

School of Molecular and Life Sciences

**Colloidal Quasi-one-dimensional Zinc-based Semiconductor
Nanocrystals**

Dechao Chen

This thesis is presented for the Degree of

Doctor of Philosophy

of

Curtin University

January 2020

Declaration

To the best of my knowledge and belief this thesis contains no material previously published by any other person except where due acknowledgment has been made.

This thesis contains no material which has been accepted for the award of any other degree or diploma in any university

Signature:

Date: 20/01/2020

To every genius chemist and their magic chemistry world!

Acknowledgements

Science needs the courage to take every brave step and I am lucky enough to have many peoples' supports. Sincerely, I want to acknowledge my parents who give me a healthy body, intelligent mental and robust character to peruse my dream.

Firstly, I want to express my deeply grateful to two of my supervisors. Foremost, I need to express my gratitude to Dr Guohua Jia, who gave me the chance to reach the dream. In Chinese idiom, Dr Jia is the master as Bo Le who finds and recognises the ambitious horse like me. Time flies, the moment was still like yesterday when I first met Dr Jia in the beautiful Curtin chemistry building. After that, Dr Jia guided me from the basic colloidal synthesis skill to the fine organization of high-quality manuscripts. Every step in my PhD, there is the care and effort from you. Any miracle would not happen without your supervisorship. When we finally achieved the first publication of our group, in the journal of *Advanced Materials*, all those hardwork and difficulties have become my best recollections in my PhD study. Inside the academic blood, it is natural that I do learn and earn the serious research attitudes and majestic demeanour of Prof. Uri Banin from Dr Guohua Jia, and Prof. Paul Alivisatos from Prof. Uri Banin. At the same time, I would also like to thank my supervisor Prof. Mark Buntine for the supervision and kind support for the Curtin HDR Mobility award which provided me an excellent opportunity to carry out my research in the USA.

Moreover, I feel thankful to Prof. Martin Saunders for boosting my characterization skill by hand in hand teaching. You are just like an encyclopedia, and your splendid microscopy skill teaches me a lot not only in materials characterization but also in

being inventiveness. Every sunny day and midnight in CMCA is one of my best memories in my PhD.

After then, I want to express my sincerely appreciation to all of my friends, team members and collaborators across the world from China, Israel, USA, France, Germany, UK, Japan. All of your supports and contributions take me closer to my dream.

Last but not least, I want to thank again all my lovely family members and my beautiful hometown Hefei. A thousand miles begins with a single step, and it's my honour to born in heart of science.

This thesis and works are supported by the Australian Research Council scholarship and the Curtin HDR mobility award.

18th Jan 2020

Brisbane

Abstract

In the recent decades, colloidal nanocrystals, which also termed as quantum dots, have witnessed an extraordinary boom on the new synthesised structures and improved performances in relation to their applications. This thesis focuses on the synthesis, properties and applications of the emerging colloidal quasi-one-dimensional zinc-based semiconductor nanocrystals.

Chapter 1 gives the general motivations of thesis.

Chapter 2 demonstrates the background of fundamental knowledge of zinc-based colloidal nanocrystals, the summary of current synthesis development in terms of zinc-based nanocrystals and the overview of their emerging applications.

Chapter 3 introduces a facile thiol-etching method to synthesise colloidal alloyed $\text{ZnS}_x\text{Se}_{1-x}$ quantum rods from polydisperse ZnSe nanowires. The alloyed $\text{ZnS}_x\text{Se}_{1-x}$ quantum rods were directly used in photocatalysis for water oxidation, showing a striking oxygen evolution capability of $3000 \mu\text{mol g}^{-1} \text{h}^{-1}$.

Chapter 4 presents a novel hetero-ZnS (short arms)–ZnSe (long arms)/ZnS shell nanorod couples structure. By further overgrowing an alloyed ZnCdS layer on the nanorods couples, the core shell heterostructure can generate blue fluorescence.

Chapter 5 reports a direct method to synthesis green fluorescence type-II ZnSe(Rod)/CdS(Rod) core shell quantum rods with staggered band gap alignments.

Chapter 6 summarizes the work conducted in the thesis and overlooks the future perspectives.

Contents

Declaration	I
Acknowledgements	III
Abstract	V
Contents.....	VI
Chapter 1. Motivation	10
Chapter 2. Background.....	10
2.1 Introduction	11
2.2 Tailoring Band Gap through Quantum Confinement Effects.....	13
2.3 Synthetic Methodology.....	14
2.4 Types of Zn-containing semiconductor NCs.....	20
2.4.1 ZnSe	20
2.4.2 ZnS	22
2.4.3 ZnTe	24
2.4.4 Zn ₃ P ₂ and Zn ₃ As ₂	25
2.4.5 Alloy.....	27
2.4.6 Core Shell.....	32
2.4.7 Doping.....	38
2.4.8 Hybrid.....	41
2.5 Photoelectronic Energy Conversion Applications.....	45

2.5.5	Lighting and Displays.....	45
2.5.6	Photocurrent Response.....	47
2.5.7	Photocatalysis	51
2.6	Summary	54
2.7	References.....	54
3	Spontaneous Formation of Noble- and Heavy-Metal Free Alloyed Semiconductor Quantum Rods for Efficient Photocatalysis	65
3.1	Abstract.....	65
3.2	Introduction.....	66
3.2	Experimental Section and Methods	67
3.4	Results and discussion	74
3.5	Conclusion	107
3.6	References.....	107
4.	Colloidal Quasi-One-Dimensional Dual Semiconductor Core/Shell Nanorod Couple Heterostructures with Blue Fluorescence.....	113
4.1	Abstract.....	113
4.2	Introduction.....	114
4.2	Experimental Section	115
4.3	Results and Discussion	121
4.3.1	Controlled Synthesis and growth mechanism of hetero- ZnS (short arm)- ZnSe/ZnS core/shell (long arm) nanorod couples	121

4.3.2 Electronic structure of hetero-ZnS (short arm)-ZnSe/ZnS core/shell (long arm) nanorod couples.....	139
4.3.3 Optical properties of hetero- ZnS-ZnSe/ZnCdS core/shell nanorod couples	144
4.4 Conclusion.....	155
4.5 References	156
Chapter 5. Type-II ZnSe (Rod)/CdS (Rod) Core/Shell Quantum Rods with Green Fluorescence.....	162
5.1 Abstract	162
5.2 Introduction.....	162
5.3 Experimental Section	164
5.4 Results and discussion.....	166
5.5 Conclusion.....	179
5.6 References	179
Chapter 6. Summary and Perspectives.....	182
Contribution Claim.....	184
Copyright Claim.....	189

Chapter 1. Motivation

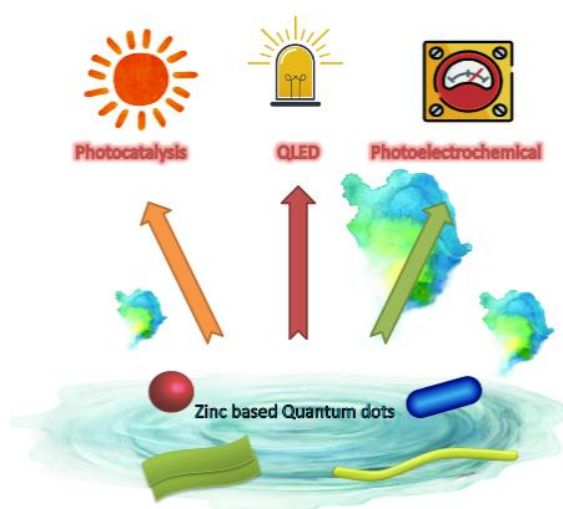
The research is dedicated to explore alternatives to the traditional cadmium colloidal semiconductor nanocrystals by using zinc based colloidal semiconductor nanocrystals, and specifically focuses on the quasi-one-dimensional nanocrystals. Their properties and applications have been investigated.

Chapter 2. Background

(Chapter 2 and 6 were adapted with permission from D. Chen, A. Wang, M. Buntine, G. Jia, Recent Advances in Zinc-Containing Colloidal Semiconductor Nanocrystals for Optoelectronic and Energy Conversion Applications, *ChemElectroChem*, 2019, 6, 4709-4724. Copyright 2019 Wiley-VCH Verlag GmbH & Co. KGaA, Weinheim.)

Colloidal semiconductor nanocrystals (NCs), especially cadmium (Cd)- and lead (Pb)-based ones, have been proved to be the promising materials for photoelectronic energy conversion applications. However, the high toxicity and cost of these materials restrict their widespread use. Zinc (Zn)-based colloidal semiconductor NCs are non/less toxic and environmental friendly materials, manifesting stimulating optical and electronic properties with relevance to a broad scope of applications from light emitting diodes (LEDs), sensors, photocatalysis and more. In this chapter, we elaborate the shape control of Zn-based colloidal semiconductor NCs achieved by a variety of colloidal synthetic approaches. Moreover, the formation of core-shell,

doping and hybrid structures based on Zn-based colloidal semiconductor NCs allow for the optimization of their functionalities, which underpin stimulating photoelectronic energy conversion applications in quantum dots LEDs (QLEDs), photodetectors and photocatalysis. Zn-based colloidal semiconductor NCs that combine the green chemistry with sustainable developments possess a bright future.



Scheme 1. Cartoon of the function of zinc based colloidal nanocrystals

2.1 Introduction

Colloidal semiconductor NCs, also termed quantum dots (QDs), are tiny crystals made of semiconductor materials with dimensions being comparable to their exciton Bohr radius.¹ Presently, Cd- and Pb-based semiconductor NCs are well developed in terms of both fundamental science and practical applications due to their facile synthetic accessibility and intriguing properties.² However, Cd and Pb are heavy metals. The high toxicity of Cd- and Pb based QDs and legistroy regulations are the

major obstacles for their widespread use. As a result, zinc-based QDs have been considered as the potential alternatives to the traditional heavy metal-based QDs.³

The compounds of zinc-based colloidal semiconductor NCs typically contain II–VI group (e.g. ZnSe, ZnS and ZnTe) and II–V group QDs (e.g. Zn₃P₂ and Zn₃As₂).⁴ Being analogous to the heavy metal-based QDs, the band gap of zinc-based colloidal semiconductor NCs covers a wide spectral range spanning from ultraviolet to visible. Meanwhile, many intriguing optical and electrochemical properties of Zn-based QDs are emerging. Furthermore, according to the band structure alignment, tailoring the dimensions of NC themselves in the combination of semiconductor NCs with other materials such as metals, can manipulate the quantum confinement of excitons and induce efficient charge separation to meet the specific requirements in diverse applications. In consideration of energy application based on Zn-based QDs, they offer an environmental benign and low cost platform by using non/less toxic and earth abundant materials, to exploit many stimulating technological applications in optoelectronics, catalysis, sensors, detector, biomedicine and more.^{3,5,6,7,8}

In this review, firstly we overview the development of zinc-based colloidal binary semiconductor NCs (ZnSe, ZnS, ZnTe, Zn₃P₂ and Zn₃As₂). Then we elaborate structural engineering of Zn-based QDs in terms of core-shell, doping and hybrid, followed by a discussion on their stimulating properties. Thirdly, the recent advances in energy conversion applications of Zn-based QDs in light-emitting diode (LED), photoelectrochemical reactions and photocatalysis are summarized and highlighted. Finally, future perspectives in this stimulating research field from fundamental studies to the emerging applications have been proposed.

2.2 Tailoring Band Gap through Quantum Confinement Effects

The band gap of bulk zinc chalcogenides ranging from 2.39 eV to 3.61 eV falls in blue and green spectral ranges. In particular, the size control of single content zinc chalcogenide NCs provides an approach to tune their band gap. As shown in Fig. 1, the band gap energies of zinc chalcogenide NCs can cover almost the entire violet-blue and blue spectral ranges. Their band gaps can be further expanded through the size tuning of zinc chalcogenide NCs, as depicted by gaps between the conduction band and predicted energies (red bars in Figure 1). Beyond the size control, the control in morphology shows the potential in tailoring their unique physical properties. Furthermore, other strategies such as compositing core/shell, alloying and doping structures are often used to improve the fluorescence quantum yields, conductivity and stability. As the lighting in the violet-blue and blue spectral ranges is highly demand, zinc-based chalcogenides are potential candidates for next-generation environmental friendly lighting industries.

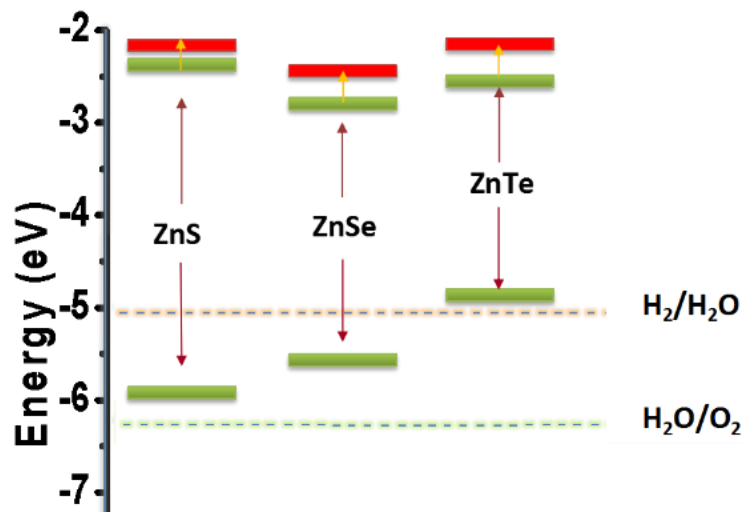


Figure 1. Electronic energy levels of bulk zinc chalcogenides (green bar) and their adjustable band gaps (red bar).^{9,10}

2.3 Synthetic Methodology

The synthetic strategies of Zn-containing QDs include almost all of the general colloidal synthetic approaches for colloidal NCs such as heating-up (HU) method, hot-injection (HI) method and cation exchange (CE) reaction. Those basic synthetic methods are based on various growth mechanisms. The heating-up and hot-injection method are kinetic controlled with high concentrations of monomers while cation exchange method is post-synthesis method.

A heating-up method is also called the “non-injection” method, in which all reagents are mixed in a reaction medium and heated up to a temperature to induce nucleation and growth of nanoparticles. For example, in a typical synthesis of this method for zinc sulfide NCs, zinc diethyldithiocarbamate ($\text{Zn}(\text{ddtc})_2$) and zinc dibutyldithiocarbamate ($\text{Zn}(\text{dbdc})_2$) act as the single source precursors in the presence of surfactant/reaction medium of amine ligands, leading to the formation of nearly monodisperse ZnS.^{11,12} By the modification of the passivating surface ligands, the growth of zinc-containing NCs can be controlled via a variety of growth mechanisms including epitaxial growth, ripening, overcome the energy barrier that required for the nucleation. The nucleation of zero-dimensional (0D) NCs can be used as the seeds for further growth of the NCs. Zinc precursors such as zinc stearate (ZnSt_2) and diethylzinc (ZnEt_2) are widely used in the reactions with sulfur or selenium precursors (Table1).^{18,19} Until now, most Zn-containing nanostructures can

be synthesized through the HI method by the control of activity of both precursors and solvents.

Cd-containing CdSe/CdS core/shell nanorods can be readily prepared by a seeded growth method.²⁰ However, this synthetic approach does not work for Zn-containing NCs because Zn-containing NCs may not be compatible with anisotropic growth under similar synthetic conditions. The CE method provides an accessible approach in compositing desirable nanostructures which is hard to be directly synthesized using conventional synthetic methods. A representative example is the formation of blue-emitting ZnSe/ZnS core/shell nanorods through sequential cation exchange, in which CdSe/CdS nanorods firstly convert into Cu₂Se/Cu₂S nanorods, followed by the substitution of Cu⁺ ions in the crystal lattices by Zn²⁺ ions that produces the final products of ZnSe/ZnS nanorods.²¹

In addition, aqueous synthetic approach can be used in the preparation of colloidal zinc-containing NCs. In a typical synthesis, the reaction between zinc and chalcogen precursors in the presence of an appropriate surfactant such as thioglycolic acid, 3-mercaptopropionic acid and 1-thioglycerol leads to water soluble zinc chalcogenide NCs.^{22,22,23,24} Furthermore, the reaction can be conducted at a relative low temperature, i.e. < 100 °C, and does not require inert atmosphere. These merits are beneficial in the functionalization of the NCs for biological applications.²⁵ By optimizing the synthetic conditions, the control of size, shape and structure of Zn-containing NCs can be achieved and further used in diverse energy conversion applications.

Table 1. Typical synthetic approaches of Zn-containing NCs. (N/A: nor reported or not existing)

Item	Metal Precursor	Anion Precursor	Method	Morphology	Emission Range	Quantum Yield
0 D Structures						
ZnSe NCs ¹⁸	ZnEt ₂	Se-TOP	Injection	Dots	365-410nm	20-50%
ZnSe NCs ¹⁹	Zn(St) ₂	Se	Injection	Dots	365-430nm	50%
ZnSe NCs ²⁶	ZnCl ₂	N/A	Cation exchange	Spherical NCs	N/A	N/A
ZnS NCs ¹³	ZnEt ₂	S	Injection	Dots	335 nm, 350 nm	N/A
ZnS QDs ²⁷	Zn(NO ₃) ₂	Na ₂ S	Injection	Dots	440 nm	31%
ZnTe quasi-Spheres ²⁸	ZnAc ₂	Te-TOP	Injection	Quasi-spheres	N/A	N/A
Zn ₃ P ₂ nanoparticles ²⁹	Zn(OMe) ₂ Or Zn(CHMeC H ₂ NMe ₂) ₂	P(SiMe ₃) ₃	Heat up	1.5-2.5 nm/ 4.5-6.5 nm dots	N/A	N/A
Zn ₃ P ₂ QDs ³⁰	Me ₂ Zn	HP ^t Bu ₂	Injection	3.59-4.32 nm dots	N/A	N/A
Zn ₃ P ₂ QDs ³¹	ZnEt ₂ and Zn(O ₂ CR) ₂	P(SiMe ₃) ₃	Injection	2.6-2.9 nm dots	620 nm	1%
Zn ₃ P ₂ QDs ³²	ZnEt ₂	(TMSi) ₃ P	Injection	3.2-8.8 nm dots	481-545 nm	0.35- 1.6%
Zn ₃ As ₂ QDs ³³	Zn(OA) ₂ and ZnEt ₂	As(SiMe) ₃	Injection	2.8 nm dots	642 nm, 939 nm	1%

1D**Structures**

ZnSe nanorods and wires ³⁴	[Zn ₄ (SPh) ₁₀] (Me ₄ N) ₂	Se-DPP	Heat up	Rods and wires	390-425 nm	1-5%
ZnSe nanorods and wires ¹⁴	Zn(St) ₂	N/A	Attachment	Rods and wires	N/A	N/A
ZnSe nanorods and wires ¹⁵	ZnAc ₂	Selenourea	Heat up	Rods and wires	436 nm, 500 nm, 546 nm	N/A
ZnSe NCs ²⁶	ZnCl ₂	N/A	Cation exchange	Rods	N/A	N/A
ZnSe quantum rods and branched NCs ³⁵	ZnEt ₂	Se	Injection	Rods and Branched NCs	420-450 nm	1%
ZnSe nanorod couples ³⁶	Zn(NO ₃) ₂	Se	Heat up	Nanorod couples	N/A	N/A
ZnSe, ZnS, ZnTe quantum rods ¹⁶	N/A	N/A	Ripening	Rods	N/A	N/A
ZnS nanorods ³⁷	Zn(ddtc) ₂	DDT	ing	Rods	N/A	N/A

ZnS nanorods ¹³	ZnEt ₂	S	Attachment	Rods	345 nm	N/A
ZnS nanowires ¹¹	Zn(ddtc) ₂	Zn(ddtc) ₂	Heat up	Wires	358 nm	N/A
ZnS nanowires ¹²	Zn(dbdc) ₂	Zn(dbdc) ₂	Heat up	Wires	337 nm	N/A
ZnS nanowires ³⁸	Zn(NO ₃) ₂	DDT	Injection	Wires	402 nm	N/A
ZnTe Nanorods ²⁸	ZnCl ₂	Te-TOP	Injection	Rods	N/A	N/A
ZnTe Nanorods ³⁹	ZnAc ₂	Te-TOP	Injection	Rods	N/A	N/A
ZnTe Nanorods ⁴⁰	Zn(AA) ₂	NaHTe	Injection	Rods	423 nm	60%
ZnTe nanobelts ⁴¹	Zn(OAc) ₂	Te-TOP	Heat up	Belts	454 nm	N/A

2D

Structures

ZnSe nanosheets ⁴²	Zn(NO ₃) ₂	Se	Heat up	Sheets	N/A	N/A
ZnS nanoplatelets ⁴³	Zn-dedtc	Zn-dedtc	Heat up	Platelets	N/A	N/A

ZnSe and ZnS quantum platelets ⁴⁴	Zn(OAc) ₂	Selenourea or thioacetami de	Injection	Platelets	N/A	N/A
--	----------------------	---------------------------------------	-----------	-----------	-----	-----

3D

Structures

ZnSe nanoflowers ⁴⁵	Zn(St) ₂	Se-TBP	Injection	Nanoflowers	N/A	N/A
--------------------------------------	---------------------	--------	-----------	-------------	-----	-----

ZnTe nanoclusters ⁴⁶	ZnCl ₂	Te-TOP	Injection	Platelets	N/A	N/A
---------------------------------------	-------------------	--------	-----------	-----------	-----	-----

ZnTe nanoflowers ⁴⁷	Zn(St) ₂	Te-TOP or Te-TBP	Injection	Nanoflowers	552 nm	N/A
--------------------------------------	---------------------	---------------------	-----------	-------------	--------	-----

ZnTe Tetrahedrons ²⁸	ZnCl ₂	Te-TOP	Injection	Tetrahedrons	N/A	N/A
---------------------------------------	-------------------	--------	-----------	--------------	-----	-----

2.4 Types of Zn-containing semiconductor NCs

Zn-containing colloidal semiconductor NCs can be divided into two main categories. The most extensively studied ones in terms of materials synthesis and energy conversion-related applications are zinc chalcogenide semiconductor NCs, including zinc selenide (ZnSe), zinc sulfide (ZnS) and zinc telluride (ZnTe). Another type of Zn-containing colloidal semiconductor NCs, which are rarely reported, is zinc pnictide such as zinc phosphide (Zn_3P_2) and zinc arsenide (Zn_3As_2). In this section, we review the fundamental aspects of Zn-containing colloidal semiconductor NCs and elaborate their stimulating optical and electronic properties.

2.4.1 ZnSe

ZnSe is the most basic and well-developed zinc chalcogenide semiconductor NCs with a wide direct band gap manifesting emission from ultraviolet to visible spectral ranges (325 nm-460 nm). By the control and modification of colloidal chemical synthetic methods, the particles size tuning ranging from 1.7 to 12 nm can be achieved, and the band gap energies can be tuned from the bulk band gap of 2.7 eV (460 nm) to 3.8 eV (326 nm), covering a large proportion of the near ultraviolet and blue spectral ranges (Fig. 1).⁴⁸ ZnSe QDs exhibits a rich phase diagram with both hexagonal and cubic crystal structures. The optical properties can be tailored by precisely tune the band gap and phase.

Colloidal ZnSe NCs have been readily synthesized through a variety of methods including the HI method and HU method. The HI method was firstly introduced to prepare nearly monodisperse ZnSe spherical nanoparticles with narrow emission line

widths.^{19,35} In contrast, 1D ZnSe nanowires and nanorods can be obtained through an oriented attachment mechanism^{14,49}, HU method¹⁵, Ostwald ripening¹⁶ and self-assembly from magic-sized clusters³⁴ (Fig. 2a-c). ZnSe nanoparticles may crystallize into other morphology such as polypods (Fig. 2f). Beyond the traditional 1D structure, Jia et al. reported a unique structure of ZnSe nanorod couples which can confine the band edge states to small short edges of the ZnSe structure (Fig. 2d).³⁶ ZnSe nanosheets was introduced by HU method in which the 2D ZnSe structures were formed via the oriented attachment process (Fig. 2e).^{42,50} Another report by Buhro et al. demonstrated that ZnSe nanoplates can be prepared from (ZnSe)₁₃(n-butylamine)₁₃ nanoclusters.⁴⁴ Other than the direct synthetic methods, cubic ZnSe and wurtzite ZnSe spherical nanoparticles as well as wurtzite ZnSe nanorods were synthesized via a sequential cation exchange method starting from cadmium-containing nanoparticles.²⁶

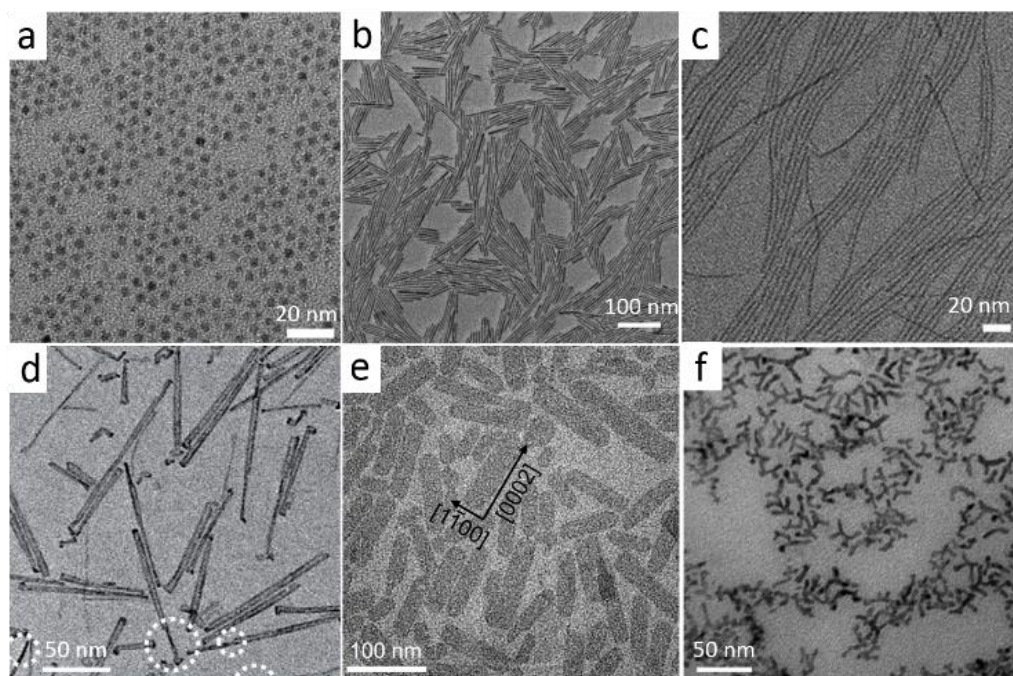


Figure 2. TEM images of colloidal ZnSe nanocrystal with diverse morphologies (a) Spherical dots, (b) Nanorods, (c) Nanowires, (d) Nanorod couples (e) Nanoplatelets, (f) Polypods. The panels were reproduced with permission from ref.³⁴ (Panel a,c; Copyright 2018 American Chemical Society),¹⁶ (Panel b; Copyright 2014 American Chemical Society),³⁶ (Panel d; Copyright 2014 Nature Publishing Group),⁴² (Panel e; Copyright 2013 Elsevier),³⁵ (Panel f; Copyright 2005 American Chemical Society).

2.4.2 ZnS

ZnS has a direct wide bulk band gap of 3.54 eV for the cubic phase and 3.91 eV for the hexagonal phase with a high transmittance in the visible range. The large exciton binding energy of 40 meV and the small Bohr radius of 2.4 nm make ZnS a significant semiconductor material in photonic and optoelectronic applications.^{51,52}

Generally, due to the large band gap of ZnS, it's hard to find a suitable semiconductor as the shell material to constitute the core/shell structure in order to achieve strong luminescence with high quantum efficiency by confining the electrons and holes into the core of ZnS. In 2007, there is a report about the highly blue-emissive 3-mercaptopropionic acid (MPA) capped ZnS QDs with a quantum yield of 31%.²⁷ The blue photoluminescence (PL) in the range from 415 nm to 440 nm is far from the band gap energy of the bulk ZnS (3.54 eV) and thus it can be attributed to the trap state emission. Later on, 1D ZnS nanorods and nanowires had been prepared in the presence of octadecylamine.⁵³ Another parallel work reports the synthesis of nanowires and nanodots with high crystallinity by the use of single source precursor of Zn(dbdc)₂.¹¹ Compare to bulk ZnS, ZnS nanodots and nanowires show a blue shift of 17-25 nm in the absorption spectra, and the emission falls in 354-358 nm.

Furthermore, the wurtzite ZnS nanowires prepared using a similar synthetic method exhibited a strong ultraviolet emission band centered at 337 nm without any trap state emission.¹² Dodecanethiol (DDT) plays an important role in controlling the morphology of ZnS nanoparticles. For example, the morphology of ZnS nanoparticles can be effectively tuned from nanorod, to nanowires and spherical dots by changing the amount of DDT.³⁸ Moreover, Chen et al. recently presented a facile approach to prepare uniform ZnS nanorods from the ZnS nanowires by the etching of DDT (Fig. 3b).³⁷ In the aspect of ZnS nanoparticles with a 2D shape, Buhro et al. assembled magic-sized nanoclusters into stacked ZnS nanoplatelets (Fig. 3c).⁴⁴ Pradhan et al. observed a phase transformation of ZnS nanodisks between wurtzite and zinc blende structures (Fig. 3d).⁴³

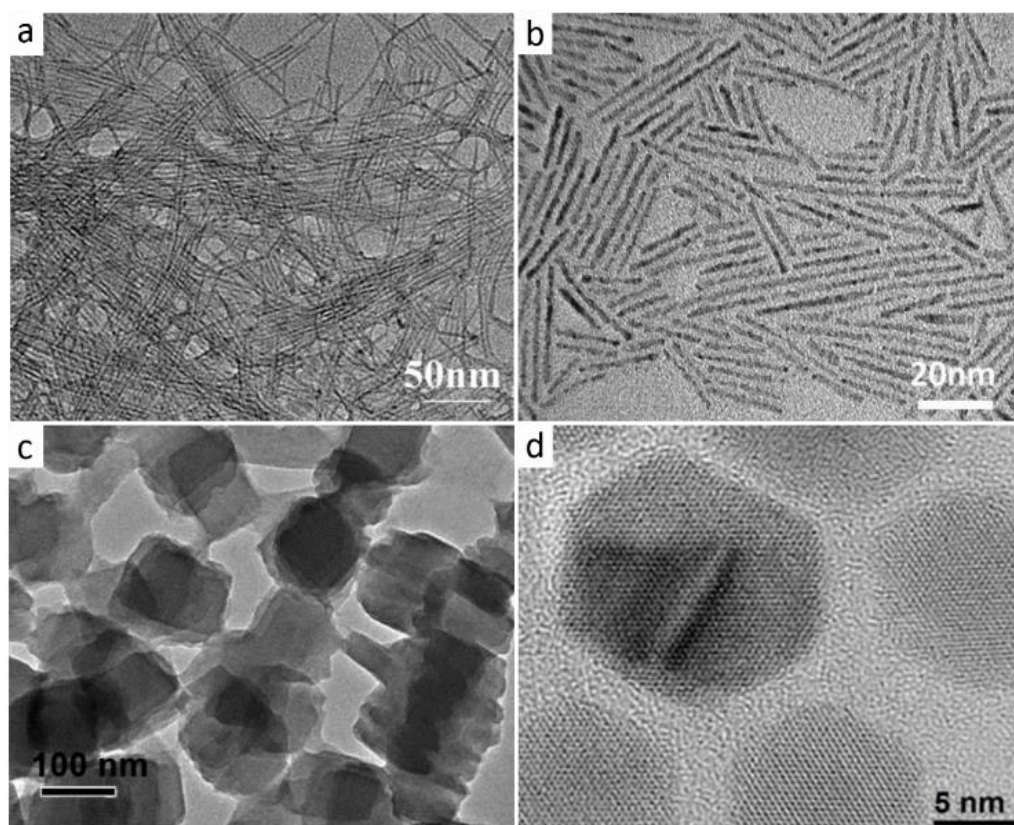


Figure 3. TEM images of colloidal ZnS nanoparticles with diverse morphologies (a) Nanowires, (b) Nanorods, (c) nanoplatelets, (d) Nanodisks. The panels were adapted with permission from Ref.¹² (Panel a; Copyright 2011 American Chemical Society),³⁷ (Panel b; Copyright 2018 Wiley-VCH Verlag GmbH & Co. KGaA, Weinheim),⁴⁴ (Panel c; Copyright 2015 American Chemical Society),⁴³ (Panel d; Copyright 2011 American Chemical Society)

2.4.3 ZnTe

ZnTe nanoparticles are less reported in comparison with other zinc chalcogenide NCs such as ZnS and ZnSe because of their difficulty in the synthesis. Zhang et al. first adapted Te-TOP as the tellurium precursor in the synthesis of ZnTe and achieved their shape control of ZnTe nanoparticles as sphere dots, tetrahedrons and nanorods by controlling of the zinc precursors and reaction temperature.²⁸ Ligand effect in combination with the reaction temperature had also been investigated to optimize the synthetic conditions that are appropriate for the synthesis of ZnTe nanoparticles with diverse shapes including spherical dots, nanorods and nanoflowers (Fig. 4a).⁴⁷ To address the issue of instability of ZnTe, aqueous ZnTe spherical dots had been synthesized by thioglycolic acid (TGA) ligand capping.⁵⁴ High single-crystalline and uniform ZnTe nanorods with a high quantum yields of 60% and good stability have been obtained through either an oriented attachment mechanism or Ostwald ripening (Fig. 4b).⁴⁰ Further potential applications of oleylamine coated ZnTe nanorods in LEDs had also been demonstrated in this work.⁴⁰ Moreover, the ZnTe nanoclusters play a vital role in the formation of the new emerging structures such as wires, triangle nanoplates and rectangular nanoplates

(Fig. 4c-f).⁴⁶ The spontaneous assembly of 2D ZnTe structures is based on a typical oriented attachment mechanism. Recently, ZnTe nanoclusters have also been used to prepare ZnTe nanoflowers (Fig. 4e).⁴¹

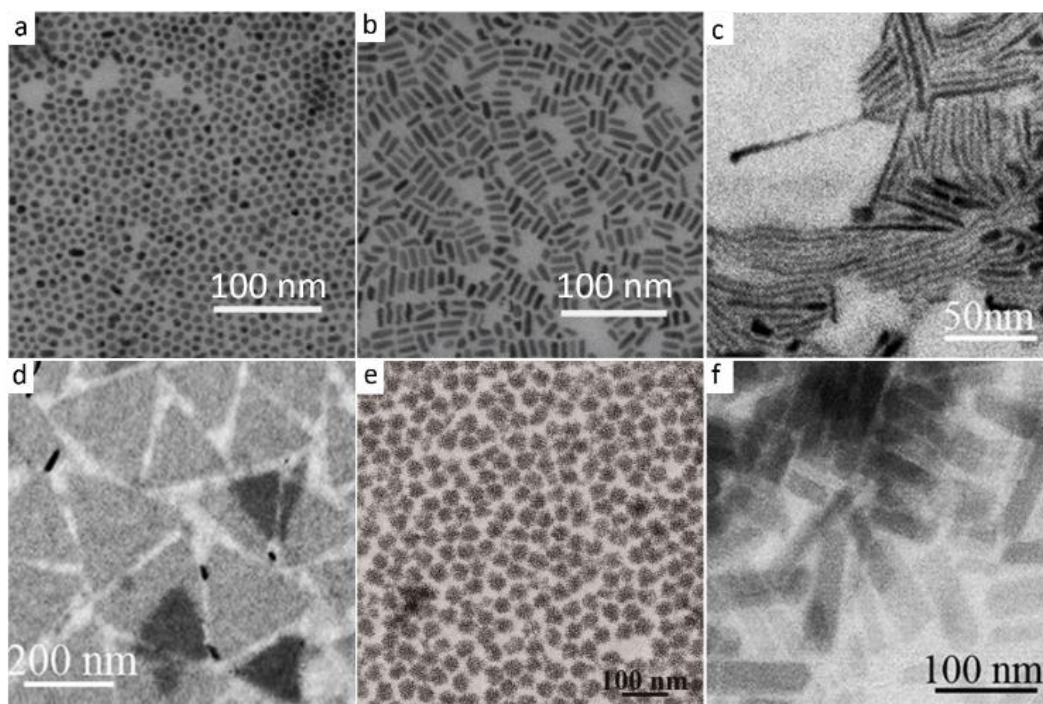


Figure 4. TEM images of colloidal ZnTe nanoparticles with diverse morphologies (a) Spherical dots, (b) nanorods, (c) Nanowires, (d) Triangle plates. (e) Nanoflowers, (f) Rectangular plates. The panels were reorganized with permission from ref.³⁹ (Panel a,b; Copyright 2011 American Chemical Society),⁴⁶ (Panel c,d,f; Copyright 2014 American Chemical Society).⁴¹ (Panel e; Copyright 2018 Wiley-VCH Verlag GmbH & Co. KGaA, Weinheim).

2.4.4 Zn_3P_2 and Zn_3As_2

Colloidal zinc pnictide semiconductor NCs including Zn_3P_2 and Zn_3As_2 QDs have rarely been studied due to the difficulties in synthesis and unavailability of precursors.

There are only a few reports on the synthesis of colloidal Zn_3P_2 and Zn_3As_2 nanoparticles. The developments of synthesis of colloidal zinc pnictide nanoparticles with various morphologies and their applications in field of energy conversion are still challenging.

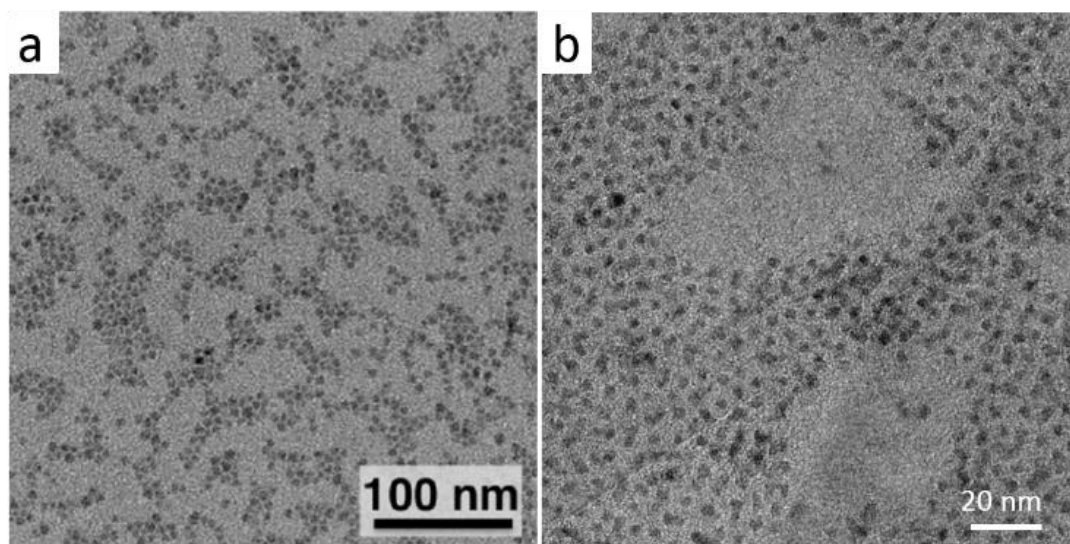


Figure 5. TEM images of (a) colloidal Zn_3P_2 nanoparticles, (b) Zn_3As_2 colloidal quantum dots. The panels were reorganized with permission from ref.³³ (Panel a, Copyright 2017 American Chemical Society),⁵⁵ (Panel b, Copyright 2014 American Chemical Society).

Bulk Zn_3P_2 has a direct band gap around 1.55-1.60 eV and a 1500 cm^{-1} absorption coefficient with a carrier diffusion length of 5-10 μm .^{56,57} The first report of the colloidal synthesis of zinc phosphide nanoparticles can be traced back to 1985 wherein a synthetic approach similar to that of CdS QDs has been reported.⁵⁸ O'Brien et al. adapted the metalorganic synthesis of Zn_3P_2 nanoparticles in the trioctylphosphine-trioctylphosphine oxide (TOP-TOPO) system and obtained the

luminescence of Zn_3P_2 nanoparticles in the blue and green spectral ranges with a Stokes shift of about 44-180 nm depending on the synthetic temperature.³⁰ The quantum yield of Zn_3P_2 nanoparticles is only around 1%.³¹ More recently, the Zn_3P_2 QDs are studied more thoroughly through the investigation of the reaction of two typical precursors of ZnEt_2 and $\text{P}(\text{SiMe}_3)_3$ associated with the intermediate state as $[\text{EtZnP}(\text{SiMe}_3)_2]_3$ and other metal organic compounds which well-explain the intermediate stages of Zn_3P_2 particle formation.^{32,59,55} Other resource such as PH_3 were also reported in the preparation of $\text{ZnO}@\text{Zn}_3\text{P}_2$ nanoparticles with an enhanced quantum yield of up to 3%.^{60,61}

There is only one report in the literature on the synthesis of colloidal Zn_3As_2 nanoparticles (Fig.5a) which takes advantage of the elevated reactivity of mixed zinc alkyl carboxylate oligomeric precursors such as ZnEt_2 and $\text{Zn}(\text{OA})_2$.³³ The 3 nm diameter of Zn_3As_2 QDs shows an optical band gap of 2.2 eV.

2.4.5 Alloy

Alloy QDs are ideal structures in overcoming materials issues such as the tendency to form defects, surface trap states and blinking effect of the nanoparticles which are closely relevant to fabricating high-quality nanoparticles. In addition to the band gap tuning of nanoparticles through the size control, alloying of QDs is an alternative approach that could retain the emission with good quantum efficiency and sharp line width. In the following section, we will elaborate two types of alloyed Zn-containing nanoparticles with and without Cd ions.

In the Cd-containing system, $\text{Cd}_x\text{Zn}_{1-x}\text{S}$ alloyed QDs show a PL emission from 474 to 391 nm with the quantum efficiency of 25-50%.⁶² The luminescence quantum efficiency of alloyed $\text{Cd}_x\text{Zn}_{1-x}\text{Se}$ QDs can be further improved to 70-85% by optimizing the synthetic condition.⁶³ $\text{Cd}_x\text{Zn}_{1-x}\text{Se}$ alloyed QDs can be also prepared in aqueous solution with a quantum yield of up to 50 % which is compared to or even better than most QDs synthesized by the conventional organometallic route (Fig. 6).⁶⁴ As shown in Fig. 6a,b, by increasing the ratio of Cd, the emission wavelength trend to red range from blue with fluctuant quantum yield. It's corresponding to the $\text{Cd}_x\text{Zn}_{1-x}\text{Se}$ alloy QDs structure formed from ZnSe QDs after injection of Cd precursor (Fig. 6c,d). Besides the alloying of the cations in the host of QDs, a broader and tunable emission crossing the entire visible spectral range of 440-650 nm was achieved in quaternary-alloyed QDs such as ZnCdSSe .⁶⁵

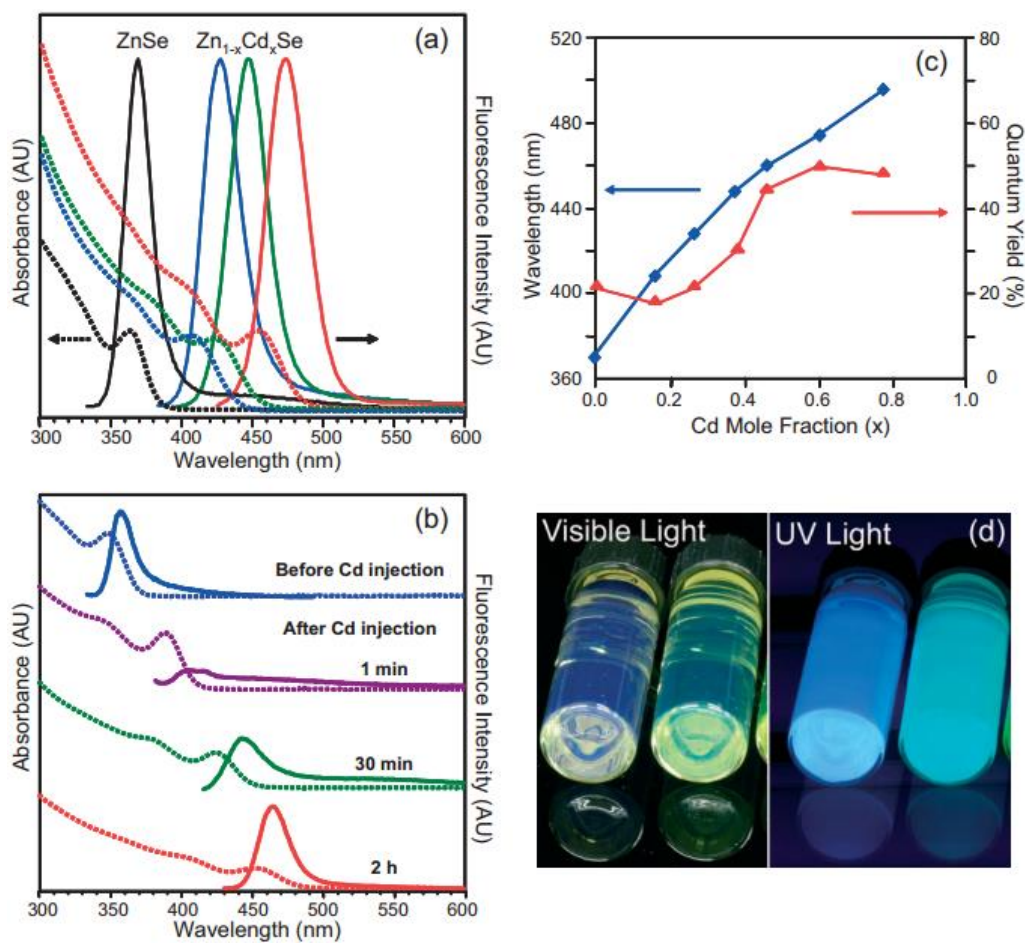


Figure 6. (a) Absorption and fluorescence spectra of ZnSe and Zn_{1-x}Cd_xSe alloyed QDs with different content ratio of Cd. (b) Absorption and fluorescence spectra of evolution of Zn_{1-x}Cd_xSe alloyed QDs with time. (c) Quantum yield and emission wavelength of Zn_{1-x}Cd_xSe alloyed QDs with different content ratio of Cd. (d) Photographs of emission of Zn_{0.4}Cd_{0.6}Se and Zn_{0.3}Cd_{0.7}Se alloyed QDs under UV-Vis light. Reprinted with permission from Ref.⁶⁴ Copyright 2007 Wiley-VCH Verlag GmbH & Co. KGaA, Weinheim.

In Cd-free systems, Zn-containing QDs show intriguing optical and electronic properties. Blue emitting ZnSeS alloyed QDs with a quantum yield of 25-30% by aqueous synthesis.⁶⁶ A one-pot synthetic approach using diphenylphosphine (DPP)

as the precursors produced $\text{ZnSe}_{1-x}\text{S}_x$ alloy QDs with a quantum yield of up to 60% (Fig. 7a).⁶⁷ Besides the spherical $\text{ZnS}_x\text{Se}_{1-x}$ alloyed nanoparticles, $\text{ZnS}_x\text{Se}_{1-x}$ alloyed nanorods have been achieved through the thiol etching at elevated temperatures.³⁷ The exposed (100) surfaces from $\text{ZnS}_x\text{Se}_{1-x}$ quantum rods possess highly active Zn sites and show enhanced photocatalytic activity in oxygen evolution reaction. Other 1D Zn-containing nanoparticles such as $\text{ZnSe}_{1-x}\text{Te}_x$ alloyed nanowires can be synthesized through the solution-liquid-solid route by using the Bi metal nanoparticle as the catalyst (Fig. 7b,c).⁶⁸ As for the 2D structures, the $\text{ZnS}_x\text{Se}_{1-x}$ nanoplates were obtained by a cation exchange reaction from $\text{Cu}_2\text{S}_x\text{Se}_{1-x}$ hexagonal nanoplates (Fig. 7d).⁶⁹ It is worth noting that multicomponent alloy colloidal nanoparticles have emerged through the partial cation exchange method as these nanoparticles are not accessible by the conventional wet-chemical routes.^{70,71}

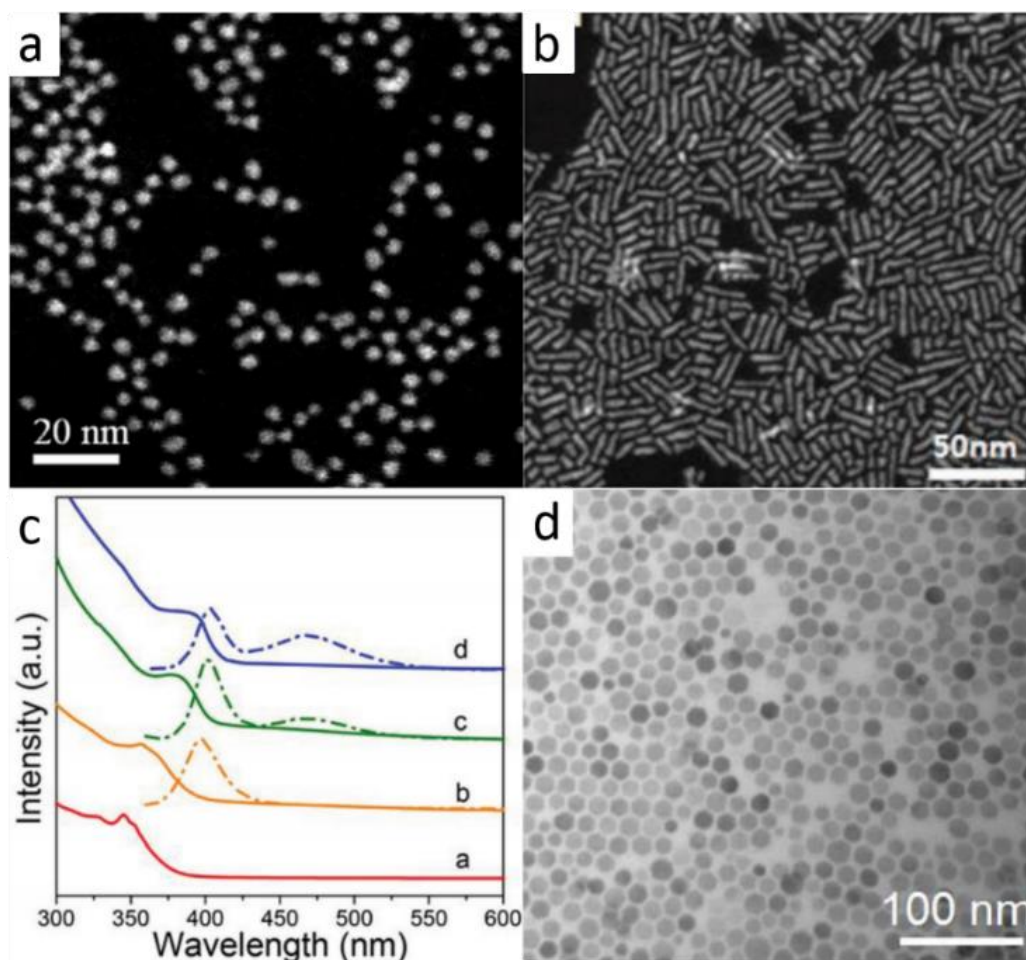


Figure 7. (a) HAADF-STEM image of $\text{ZnSe}_{1-x}\text{S}_x$ alloyed QDs. Reprinted with permission from Ref.⁶⁷, Copyright 2012 American Chemical Society. (b) HAADF-STEM image of $\text{ZnSe}_{1-x}\text{S}_x$ alloyed nanorods. (c) Absorption (solid line) and PL spectra (dashed dotted line) of the nanoparticles (from ZnSe nanowires to $\text{ZnS}_x\text{Se}_{1-x}$ alloyed quantum rods). (b,c) are reprinted with permission from Ref.³⁷, Copyright 2018 Wiley-VCH Verlag GmbH & Co. KGaA, Weinheim. (d) TEM image of wurtzite $\text{ZnS}_x\text{Se}_{1-x}$ alloyed nanoplates. Reprinted with permission from Ref.⁶⁹, Copyright 2013 Wiley-VCH Verlag GmbH & Co. KGaA, Weinheim.

2.4.6 Core Shell

Core/shell structures allow to grow one or more semiconductor layer(s) to passivate the surface of core and play a vital role in the energy conversion for quantum materials. The band gap of core and shell materials varies from their counterparts of bulk semiconductors due to the quantum confinement effect. Core/shell structures can be engineered based on the conduction and valence band alignments, which allow for the confinement of the electrons and holes partially or completely confined in the core or shell in order to meet the requirements for diverse applications in electronics and photoelectronics. The core/shell structures generally include three types namely type-I, type-II and reverse type-I. In Zn-containing core/shell QDs with type-I and type-II configurations are the most intensively investigated structures (Fig. 8). For the type-I structure, band gap of the shell material is larger than that of the core, so that both electrons and holes are confined in the core. Type-II structure shows staggered band alignments one of the charge carriers is confined in the core, while the other is in the shell, making them capable in optoelectronic applications. For reversed type-I structure, the holes and electrons are localized in the shell. In quasi-type-II structure, holes are confined in the core while electrons are delocalized throughout the whole the core and shell. In table 2, we summarized the representative core shell structures of zinc-containing QDs. Due to the large band gap of ZnS, a ZnS shell usually leads to a type-I structure whereas a type-II structure is prominent when cadmium chalcogenide are used as the shell due to the staggered band alignments.

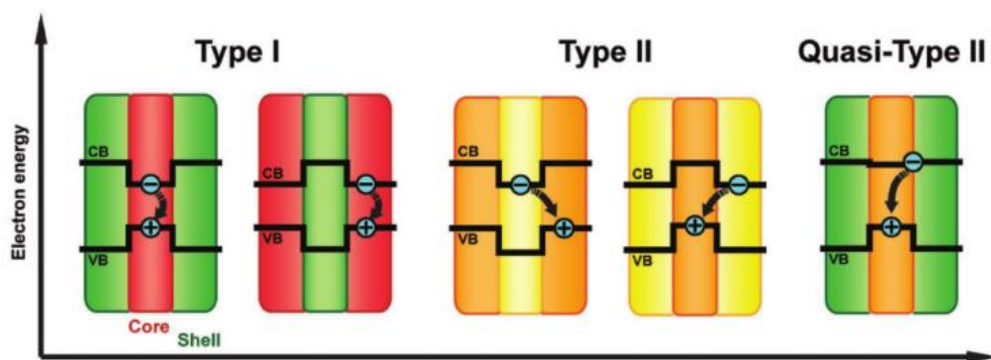


Figure 8. The schematic of band alignments of core/shell materials. Reprinted with permission from Ref.⁷², Copyright 2017 Wiley-VCH Verlag GmbH & Co. KGaA, Weinheim.

As discussed previously, ZnSe have a large band gap in the blue spectral range. This makes it an ideal material as the core to fabricate blue emitting core/shell QDs. ZnS has a larger band gap than ZnSe and therefore can acts as the shell material to effectively confine the hole and electron in the ZnSe core, as demonstrated in core/shell ZnSe/ZnS nanoparticles with 0D, 1D and 2D morphologies. However, the interfacial lattice strain make it difficult to over grow a perfect ZnS shell on the ZnSe core, being different from the shell growth of CdS on the CdSe core.⁷³ In such cases, the growth of ZnS form helix or island structures rather than a smooth shell. The ZnS shell can grow on the ZnSe core by using the precursors of thiourea and zinc acetate in water solution.^{74,75} The obtained ZnSe/ZnS QDs show a blue emission in the range of 390-460 nm with a maximum quantum yield of 65%. The ZnSe/ZnS core/shell nanorods with a maximum quantum yield of 15% can be achieved by a cation exchange method from the CdSe/CdS core/shell nanoplatelets.²¹ For nanorods, recently Ji et al. successfully tailored the ZnSe/ZnS core/shell rods by constructing

versatile surface architectures as flat-shell, islands-shell and helical-shell.⁷³ A quantum yield as high as ~50% can be achieved. The strategy by tailoring the strain at the interface of the core and shell could be expanded to other semiconductor nanoparticles to improve both the quality of shell and the quantum yield. Recently, new types of Zn(Te,Se)/ZnS QDs with green emission around 535 nm and narrow emission line width of 30 nm have been prepared. However, the quantum yield of this type of core/shell QDs is very low, which is about 1%.⁷⁶ The controllable synthesis of Zn-containing core/shell structures with a high quantum yield remains a challenge.

Compare to Zn-containing core/shell structures with the type-I configuration, those with a type-II configuration usually adopt CdSe or CdS material for the shell as the cadmium chalcogenides have a good chemical stability and smaller band gap in comparison with that of the core materials. ZnSe/CdS core/shell structures with diverse morphologies including spherical dots and rods have been reported. Zamkov et al. synthesized the ZnSe/CdS core/shell QDs with a quantum yield of 20%.⁷⁷ Furthermore, Banin et al. obtained the ZnSe seeded CdS nanorods with a quantum yield of 45%. In comparison with the type I CdSe/CdS core/shell nanorods, ZnSe/CdS core/shell nanorods with a type II configuration show a longer fluorescence lifetime of 105 ns because the electrons are more delocalized into the shell material.⁷⁸ As for other type-II core/shell ZnTe/ZnSe nanoparticles, they have a broad emission ranging from 500 nm to 575 nm and a long average fluorescence lifetime of ~77 ns.⁷⁹ However, their quantum efficiency is low, i.e. 6%, as the spatial separation reduces the electrons and holes recombination possibilities. In addition, double shell of Zn-containing core/shell QDs using the ZnSe as the core material has

also been prepared in order to improve quantum efficiency and tailoring the distribution of the charge carriers for type-II core/shell structures.^{80,81} More than double shell, Jia et al recently reported a hetero-ZnS (short arms)-ZnSe (long arms)/ZnS shell nanorod couples with alloyed ZnCdS shell with blue emission.⁸² The electron was proved to occupy only ZnSe states, while the hole occupies a ZnS-ZnS state. Over-coating ZnCdS layer of the nanorod couples eliminates the surface traps and improves the quantum efficiency.⁸² The emission of ZnSe/CdSe core/shell QDs with a type II configuration can be precisely tuned from violet to red by depositing a CdSe shell with difference thickness on the ZnSe core.⁸³ In the CdSe/ZnSe core/shell QDs, the increase of the shell thickness of ZnSe leads to a continuous transition from type-I to type-II and then back to type I structures.⁸⁴

Table 2. Summary of zinc-containing core shell structures.

Item	Type	Core	Shell	Morphology	Emission range	Quantum yield
ZnSe/ZnS QDs ^{74,75}	I	ZnSe	ZnS	Dot with shell	390-460 nm	45%, 65%
ZnSe/ZnS nanorods ²¹	I	ZnSe	ZnS	Dot in rod	380-440 nm	6-15%
ZnSe/ZnS nanorods ⁷³	I	ZnSe	ZnS	Rod in rod	421-485nm	~50%
ZnSe/ZnS nanoplatelets ⁸⁵	I	ZnSe	ZnS	Platelet with shell	N/A	N/A
Zn(Te,Se)/ZnS QDs ⁷⁶	I	Zn(Te,Se)	ZnS	Alloyed dot with shell	521-559 nm	<1%
ZnSe/CdSe NCs ⁸³	Reverse I	ZnSe	CdSe	Dot in dot	418-674 nm	40-85%
ZnTe/ZnSe QDs ⁷⁹	II	ZnTe	ZnSe	Dot in dot	500-575 nm	6%
ZnTe/CdSe NCs ⁸⁶	II	ZnTe	CdSe	Dot in dot	580-880 nm	10-30%

ZnSe/CdS NCs ⁷⁷	II	ZnSe	CdS	Dot in dot	460-630 nm	12-18%
ZnSe/CdS nanorods ⁷⁸	II	ZnSe	CdS	Dot in rod	550-600 nm	26%, 45%
ZnSe/ZnS/Cd S QDs ⁸⁰	II	ZnSe	ZnS/C dS	Dot with double shell	~565 nm	6-39%
ZnSe/CdS/Zn S QDs ⁸¹	II	ZnSe	CdS/Z nS	Dot with double shell	470-630 nm	43-61%
(Zn,Cd)Te/Cd Se nanowires ⁸⁷	II	(Zn, Cd)Te	CdSe	Wire with shell	530-760 nm	20-60%

2.4.7 Doping

Doping is another powerful strategy to tune the band gap through creating electronic energy levels. Generally, doping transition metal ions into the lattice of semiconductors allows for lower energy light emission without changing the band gap of the host semiconductor, leading to a large Stokes shift in comparison to the band gap of the host QDs. The doping of Zn-containing semiconductor NCs has been extensively investigated to tune the emission from UV to visible.

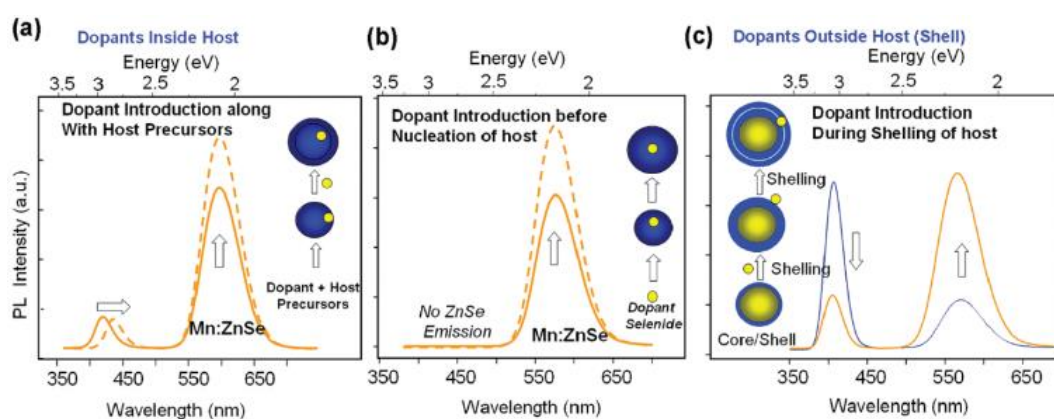


Figure 9. Illustrations and corresponding PL of different doping states. (a) Doping process along with host precursors, (b) Dopant present before the nucleation of host, (c) Doping process during the shell growth of host. Reprinted with permission from Ref.⁸⁸, Copyright 2011 American Chemical Society.

Doping of semiconductor NCs is typically involving two transition metal ions such as Mn and Cu and the doping strategy can vary, as shown in Fig. 9.⁸⁸ In Fig. 9a, Mn was doped in ZnSe QDs with Mn and Zn precursors prepared at the same time.⁸⁹ The emission peak of Mn-ZnSe QDs keeps as the same at wavelength of 580 nm but the emission intensity becomes stronger as the dopant concentration of Mn increases.

Those evidences indicate the high efficient energy transfer from the host of ZnSe QDs to the Mn dopants. For the nucleation-doping, as shown in Fig. 9b, Mn dopants were introduced before the formation of ZnSe NCs and grown with the host NCs.⁹⁰ In the same work, they also show a growth-doping strategy by using Cu as dopant, in which dopant firstly grew on the surface of ZnSe particles followed by a further ZnSe shell growth on the Cu-ZnSe particles.⁹⁰ Because the dopant also play as the seeds for nucleation, the strategy can form a well complete encapsulation for the dopant cations and the emission wavelength can be tuned by changing the size of host QDs. The QY of Mn-ZnSe QDs was increased to 50% though growth-doping method. Beyond that, the shell could be expanded to a heterogeneous shell. As shown in Fig. 9c, Mn was doped in ZnS shell to form the core/shell doping structures.⁹¹ The energy transfer between core/shell nanoparticles and Mn dopants can be switched depending on the level of the doping concentration.

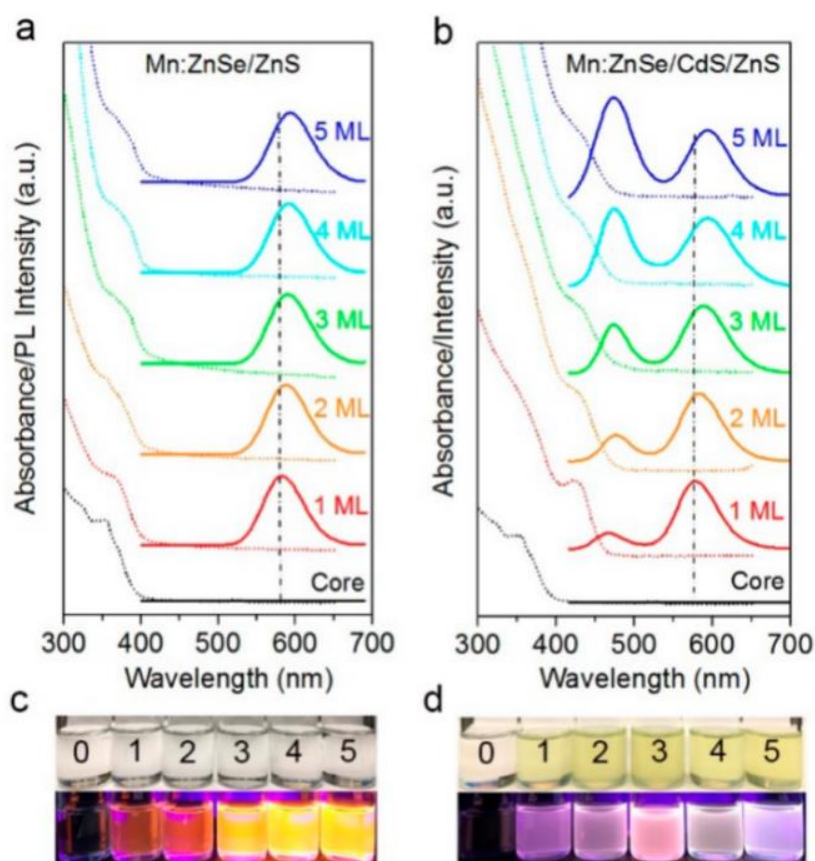


Figure 10. UV-Vis absorption and PL spectra of (a) Mn doped ZnSe/ZnS core/shell nanowires and (b) Mn doped ZnSe/CdS/ZnS core shell nanowires. The optical image of (c) Mn doped ZnSe/ZnS core shell nanowires and (d) Mn doped ZnSe/CdS/ZnS core shell nanowires. Reprinted with permission from Ref.⁹², Copyright 2017 American Chemical Society.

Mn²⁺ has also been doped into 1D Zn-containing NCs to improve their luminescence such as in Mn-ZnSe nanowires,⁹³ Mn-ZnS nanorods,⁹⁴ Mn-ZnSe nanorods⁹⁵. Those doped nanostructures exhibit enhanced fluorescence and controlled electronic and magnetic properties.^{96,97} Compared with Mn doped type-I ZnSe/ZnS core shell nanowires (Fig. 10a,c), Mn doped quasi type II/type I ZnSe/CdS/ZnS double shell

nanowires showed shell thickness-dependent emission wavelength and quantum yields (Fig. 10b,d).⁹² By increasing the shell thickness, the emission of Mn doped ZnSe/ZnS core shell nanowires shifted from 540 to 640 nm, while the emission center of Mn doped ZnSe/CdS/ZnS double shell nanowires transferred from Mn center of 590 nm to ZnSe/CdS heterostructure of 475nm.

2.4.8 Hybrid

The hybrid structures combine the Zn-containing semiconductor NCs with other materials such as noble metal particles or other semiconductor materials to form hetero-nanostructures manifesting synergistic properties. The growth methods for such hetero- nanostructures usually contain surface growth, surface growth and diffusion, simultaneous nucleation and growth of both components and replacement of a sacrificial domain.⁹⁸

Noble metal particles can be specifically deposited on a certain location on 1D zinc chalcogenide nanorods. Yu et al. presented a novel hybrid structure which uses ZnS as main rods, and integrates the rods with Au and other semiconductor materials of small band gaps such CdS or CuS to expand their responses to the solar spectrum (Fig. 11a,b).^{99,100} Moreover, except for the composition control, noble metal nanoparticles can also selective grow on the tips of 1-D zinc chalcogenide NCs, as shown in Au-ZnS^{101,102}(Fig. 11c) and Pt-ZnSe¹⁰³(Fig. 11d). On the other hand, zinc component can be modified onto other host as tips, Banin et al. reported the heavy-metal free type-II ZnTe/ZnSe nanodumbbells with fluorescence tunable from 480 nm to 585 nm by changing the size of the ZnSe tips(Fig. 11g).¹⁰⁴ As illustrated in Fig. 11e,f, ZnSe particles can grow on one of the end facets of CdS nanorods and the Au

particles grow on the other end, whereas in another study ZnSe particles have been deposited on both end facets of CdS nanorods.^{105,106,107} All of those semiconductor nano-dumbbells showed efficient charge separation due to the type-II configuration of the hybrid structures. Similarly, ZnSe tips could also be grown on the edges of CdSe nanoplates to form 2D hybrid structures (Fig. 11i).¹⁰⁸ Except for the growth of other materials on the existing semiconductors, ion exchange can also be employed to form hybrid structures such as the CdSe@CdS/ZnS nanorods with ZnS ends in the CdS nanorods with quasi-type-II band alignment as shown in Fig. 11h.¹⁰⁹ Noble metal-semiconductor structures are functional materials for photocatalysis as the charges can be efficiently separated at the interface of semiconductor and noble metal domains.

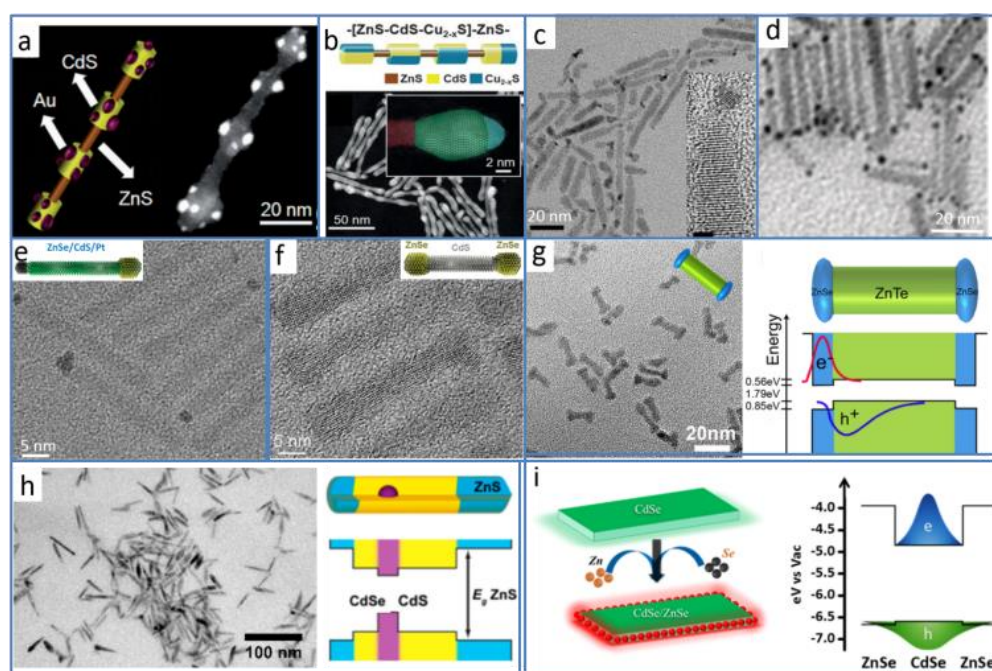


Figure 11. (a) Geometric model and HAADF-STEM image of ZnS-(CdS/Au) hybrid. Reprinted with permission from Ref.⁹⁹, Copyright 2015 Wiley-VCH Verlag GmbH & Co. KGaA, Weinheim. (b) Geometric model and HAADF-STEM image of ZnS-CdS-Cu_{2-x}S hybrid. Reprinted with permission from Ref.¹⁰⁰, Copyright 2016 Wiley-

VCH Verlag GmbH & Co. KGaA, Weinheim. (c) TEM image of Pt-tipped ZnSe nanorods. Reprinted with permission from Ref.¹⁰³, Copyright 2018 Royal Society of Chemistry. (d) TEM image of Au-tipped ZnS nanorods. Reprinted with permission from Ref.¹⁰², Copyright 2015 Royal Society of Chemistry. (e) TEM image of ZnSe/CdS/Pt hybrid. Reprinted with permission from Ref.¹⁰⁵, Copyright 2011 American Chemical Society. (f) TEM image of ZnSe/CdS/ZnSe Nanobarbells. Reprinted with permission from Ref.¹⁰⁶, Copyright 2010 American Chemical Society. (g) ZnTe/ZnSe nanodumbbells TEM image and its band alignments. Reprinted with permission from Ref.¹⁰⁴, Copyright 2017 American Chemical Society. (h) CdSe/ZnSe Dots-on-Plates illustration and its band alignments. Reprinted with permission from Ref.¹⁰⁹, Copyright 2014 American Chemical Society. (i) CdSe/ZnSe Dots-on-Plates and its band alignments. Reprinted with permission from Ref.¹⁰⁸, Copyright 2017 American Chemical Society.

In addition, the spherical zinc chalcogenide nanoparticles can be used as the seeds not only for growth of core/shell rods but also for the growth of tetrapods. Cadmium chalcogenide arms can grow on the zinc chalcogenide spherical dots as such a particle with a cubic structure has four dominant (111) facets, such as ZnTe seeded tetrapod-shaped CdSe NCs (Fig. 12a) and ZnTe seeded tetrapod-shaped CdS NCs (Fig. 12b).¹¹⁰ Typically, the cadmium chalcogenide arms grow on the core of zinc chalcogenide in four directions which are perpendicular to the (111) facet of the core particles.¹¹¹ It's worth noting the nail-shaped rods in Fig. 12f which differ from the core/shell rod using ZnS as seeds are completely under exposure.¹¹² The seed subsequent growth approach provide a powerful general method for zinc-containing

semiconductor-semiconductor synthesis. Because of the unique band gap alignment, a type-II spatial separation of charge carriers will occur in heterostructures like ZnTe/CdSe and ZnTe/CdS tetrapods. Other hybrid structures that containing zinc chalcogenide such as ZnSe-CdS nanodots,¹¹³ Zn-Ag-In-S nanorods¹¹⁴, Cu₂ZnSnS₄-Au nanorods¹¹⁵, ZnS-CuInS₂-Pt nanorods¹¹⁶ have also been reported.

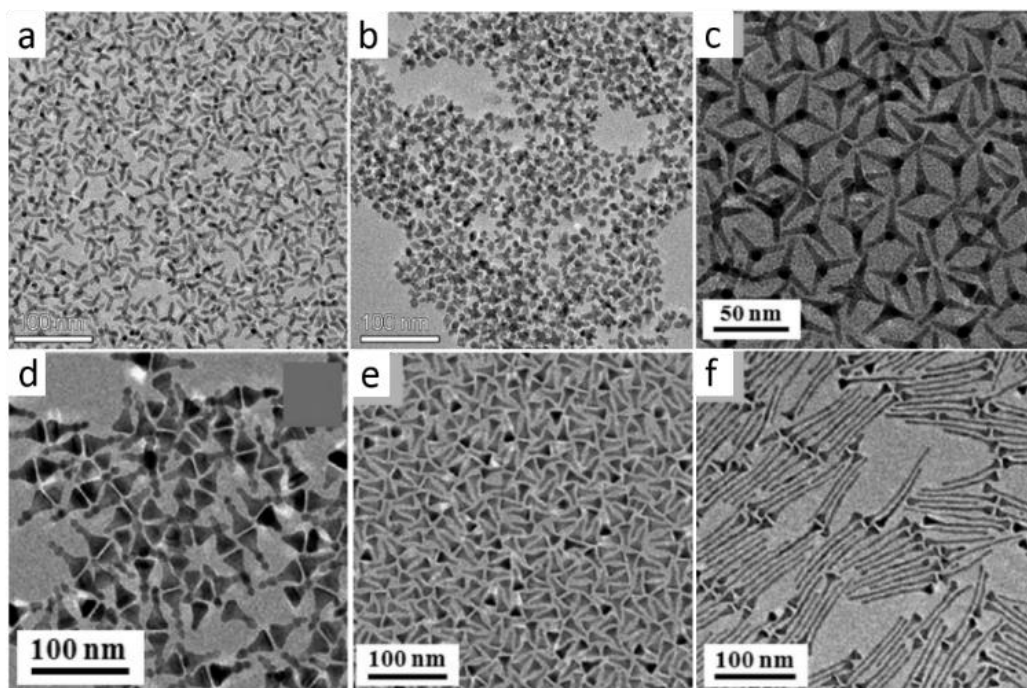


Figure 12. TEM images of (a) ZnTe seeded tetrapod-shaped CdSe NCs (b) ZnTe seeded tetrapod-shaped CdS NCs, (c) ZnSe seeded tetrapod-shaped CdSe NCs, (d) Chess-piece shaped ZnSe/CdSe NCs, (e) and (f) Nail-shaped ZnS seeded CdSe NCs. Images of a, b were reprinted with permission from Ref.¹¹⁰, Copyright 2006 Wiley-VCH Verlag GmbH & Co. KGaA, Weinheim. Images of c, d, e, f were reprinted with permission from Ref.¹¹², Copyright 2015 American Chemical Society.

2.5 Photoelectronic Energy Conversion Applications

The cadmium- or lead-containing compounds are toxic and they pose hazards to the environment which restricts their widespread uses. In this sense, environmental friendly photoelectric materials are highly demanded. Zn-containing compounds have the merits of reduced or non-toxicity, environmental benignity and excellent optical and electronic properties, and have great potential in energy conversion applications such as lighting and displays, photodetectors and photocatalysis.

2.5.5 Lighting and Displays

Core/shell QDs with high fluorescent quantum efficiency and good stability are ideal materials for lighting and displays applications. The cores passivated by the shell materials can be optically or electrically excited to generate electron and hole pairs which then re-emit photons by the electron and hole recombination, making them useful for QLED devices. Due to its large band gap and high stability, ZnS usually uses as the shell material in the core/shell structures with a type-I configuration, such as CdSe/ZnS. However, an option for heavy-metal free all Zn-containing QLEDs may be ZnSe/ZnS core/shell structures.

Typically, the emission of QLEDs using ZnSe/ZnS core/shell materials falls in the violet-blue range which is not good for lighting application. Early reports showed the fabrication of ZnSe/ZnS core/shell structures on QLEDs and achieve a 0.65% quantum efficiency (EQE) and a low current density of 500 mA/cm² with the emission peak at 420 nm.¹¹⁷ Li et al. improved the ZnSe/ZnS core shell QLEDs with a maximum EQE of 7.83% which is much higher than the best record (1.7%) of their

Cd-containing counterparts emitting in a similar spectral range (Fig. 13a-e).¹¹⁸ The current density for ZnSe/ZnS core/shell QLEDs have been promoted to 2856 cd/m² of maximum brightness with a narrow full width at half maximum (FWHM) less than 21 nm.¹¹⁹

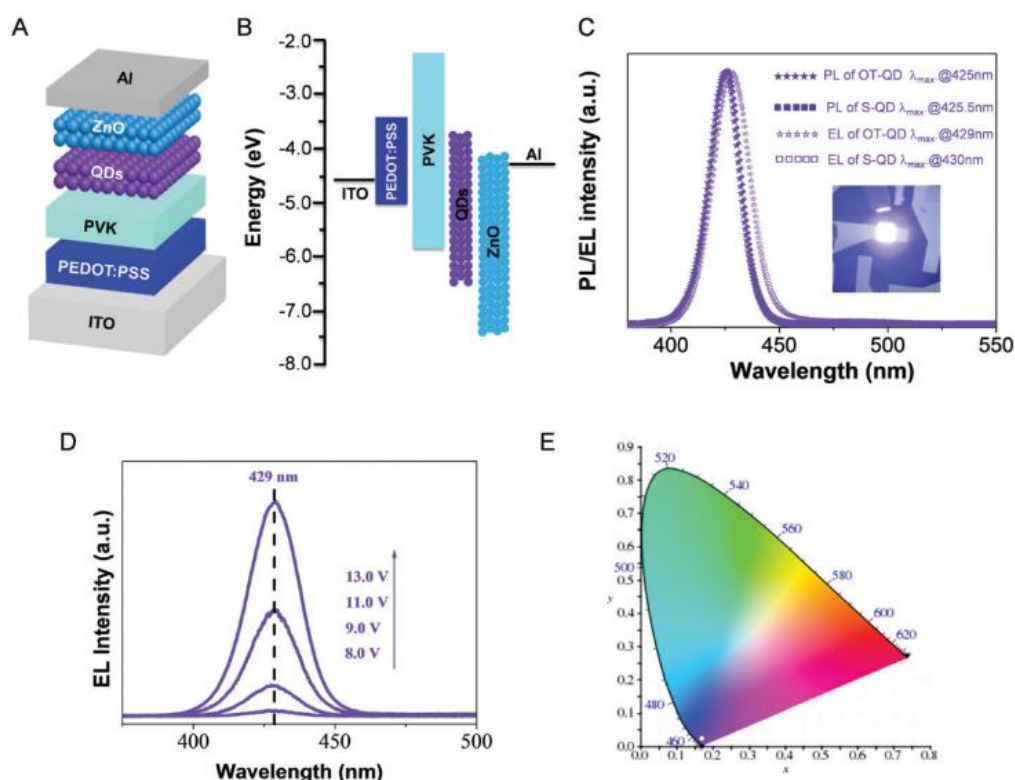


Figure 13. (a) Schematic of QLEDs device. (b) Energy level of layers. (c) PL spectra of ZnSe/ZnS core shell QDs with octanethiol and S-ODE as S sources, and corresponding EL spectra of QLEDs. (d) EL spectra of QLEDs with different bias voltage. (e) CIE color coordinates of (0.169, 0.023) corresponding to the violet emission spectra in c. Reprinted with permission from Ref.¹¹⁸, Copyright 2015 Royal Society of Chemistry.

Except for the all zinc-containing QLEDs, other nanoparticles such as Cu doped ZnInS/ZnS core/shell QDs with tunable emission from deep red to green have been used in white LEDs.¹²⁰ The produced white LEDs show high performances with the colour rendering index up to 96, luminous efficacy of 70-78 lm W⁻¹ and colour temperature of 3800-5760 K.

2.5.6 Photocurrent Response

Zn-containing colloidal QDs are potential candidates for photoelectrochemical application, due to their wide absorption in the UV and visible ranges. Generally, the UV light resource falls in an electromagnetic radiation of the wavelengths ranging from 10 to 400 nm. Meanwhile, zinc chalcogenide QDs can mainly absorb the UV light of sunlight spectrum, making zinc chalcogenide QDs promising candidate for the UV photodetectors. Bulk ZnO and ZnS (in combination with TiO₂) are widely used zinc composites, while the scale of materials is generally beyond the scope of the quantum confinement size. Therefore, more effort is desirable in focusing on the Zn-containing colloidal semiconductor NCs to investigate their photoelectrochemical application. To achieve high performance in photoresponsibility, complex structure engineering is an effective approach to gain the absorption and increase the rate for charge recombination (Fig.14), which has also been adopted in recent research.

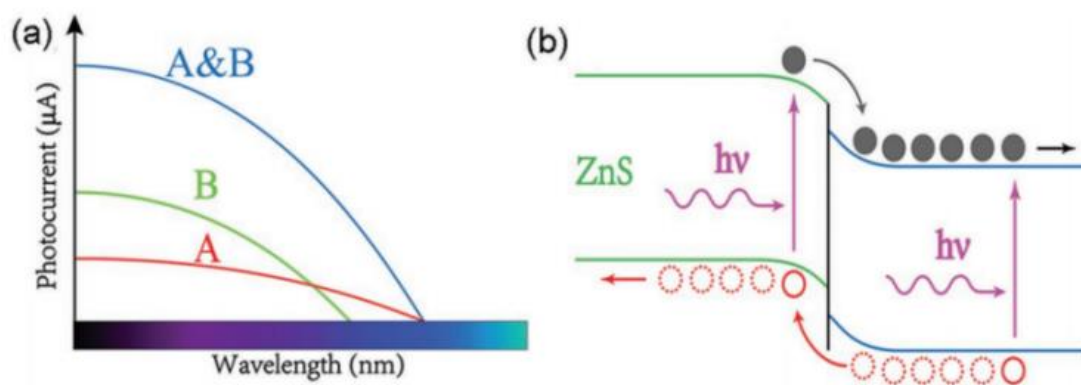


Figure 14. (a) Two composites semiconductors (A&B) with combined light absorption of single component A and B. (b) Band gap alignment of two composites semiconductors and its charge separation and transportation. Reprinted with permission from Ref.¹²¹, Copyright 2018 Wiley-VCH Verlag GmbH & Co. KGaA, Weinheim.

1D colloidal zinc chalcogenide nanocrystal-containing photodetectors had been reported which have decent photoresponse performance. ZnSe nanowires, ZnSe nanorods and ZnS nanorods show good stability in photoresponse activities. The ZnSe nanowires exhibited a size-dependent photoresponse in UVA and near-visible radiation.¹²² As shown in Fig. 15a,b, the ZnSe nanowires with a diameter of 2.1 nm show more than three times of power density than that of ZnSe nanowires with a diameter of 4.5 nm under 365 nm illuminations. When the light is switched to 405 nm, the power density of 4.5 nm diameter ZnSe nanowires surpasses that of ZnSe nanowires with a diameter of 2.1 nm. The results reveal that colloidal zinc chalcogenide nanocrystal-containing photodetectors are advantageous in tuning of the band gap to ensure efficient charge carrier transfer and match the window of detection. Similarly, ZnS nanowires exhibit a solar-blind UV photoresponse.¹²³

Recently, the $\text{ZnS}_{2/3}\text{Se}_{1/3}$ quantum rods have been proved to possess an enhanced photoresponse compared with pure ZnSe nanorods and ZnS nanorods (Fig. 15c).³⁷ The $\text{ZnS}_{2/3}\text{Se}_{1/3}$ quantum rods sensitized photoanode achieves a 90% Faradic efficiency (FE) of the theoretically calculated value as shown in Fig. 15e. The enhancement of the photocurrent density was ascribed to the dominant (100) surface of wurtzite nanorods which was further confirmed by the density functional theory simulations. As for the multicomponent Zn-containing colloidal semiconductors NCs, $\text{Cu}_2\text{ZnSnS}_4/\text{ZnSe}$ (CZTS/ZnSe) core/shell structures show an enhanced charge separation which lead to a fair photoelectrochemical performance as shown in Fig. 15d.¹²⁴ ZnS-CdS- Cu_{2-x}S heteronanorods with the absorption that covers the full spectrum of solar energy from UV to near-infrared were employed to improve the photocurrent response under chopped full spectrum irradiation.¹⁰⁰ All of those reports on colloidal Zn-containing hetero-semiconductors show the consistency in the enhanced photo(electro)catalytic capability. The emerging photoelectrochemical applications of colloidal Zn-containing NCs not only show their advantages over the heavy metal-containing systems but also challenge the traditional bulk materials.

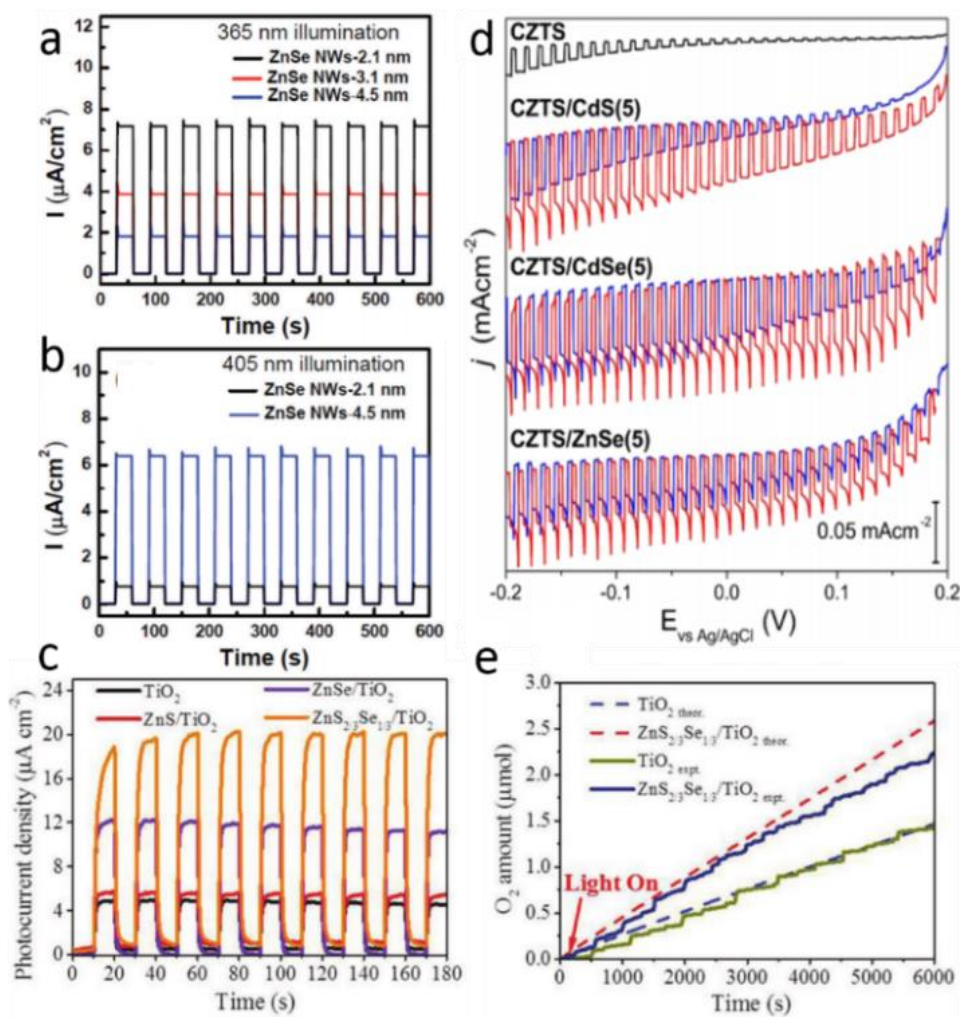


Figure 15. (a) Time response of i-t curves of ZnSe NWs with 2.1 nm, 3.1 nm and 4.5 nm diameter under 365 nm light illumination with a power density of 3.0 mW cm^{-2} . (b) ZnSe NWs with 2.1 nm and 4.5 nm diameter under 405 nm light illumination with a power density of 4.0 mW cm^{-2} . Images of a, b were reprinted with permission from Ref.¹²², Copyright 2017 Royal Society of Chemistry. (c) Time response of i-t curves of ZnSe quantum rods, ZnS quantum rods and $\text{ZnS}_{2/3}\text{Se}_{1/3}$ quantum rods under light ON-OFF cycling. (d) Linear sweep voltammograms under chopped 1 sun light illumination for CZTS before and after deposition of different buffer layers and adsorption of MV. (e) Comparison of the evolved oxygen gases of TiO_2 and $\text{ZnS}_x\text{Se}_{1-x}/\text{TiO}_2$. Images of c, e were reprinted with permission from Ref.³⁷,

Copyright 2018 Wiley-VCH Verlag GmbH & Co. KGaA, Weinheim. Images of d was reprinted with permission from Ref.¹²⁴, Copyright 2014 American Chemical Society.

2.5.7 Photocatalysis

Colloidal semiconductor NCs have advantages over their counterparts such as bulk materials as their band gap can be feasibly tuned by changing the size and composition to match the solar spectrum and oxidation/reduction potentials. The enlarged electrochemical potential can enhance the performance in both photocatalysis and photo(electro)catalytic (Fig. 16). On the other hand, Zn-containing colloidal NCs can absorb light in the UV range which makes them capable in photocatalysis. Recently, Chen et al. demonstrated that ZnSSe alloyed nanorods showed increased oxygen evolution reaction (OER) activity compared with pure ZnSe and ZnS nanorods (Fig. 17a) because the alloyed nanorods have reduced energy barrier for oxygen evolution.³⁷ Following from this work, ZnSe nanorods was applied as the visible light range absorbers for H₂ evolution with performances exceeding those of Cd-containing QDs.¹²⁵

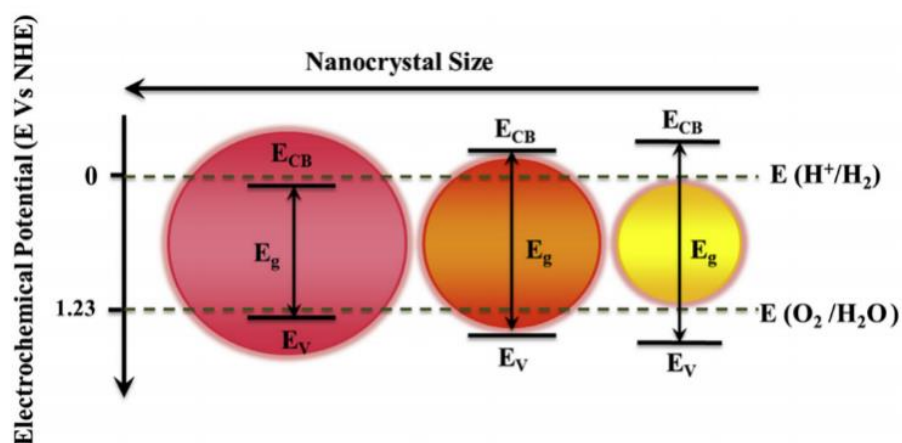


Figure 16. Quantum size effect of nanocrystal comparing to the electrochemical potential.¹²⁶

Heterostructures contain zinc colloidal NCs and other colloidal semiconductors (e.g. CdS and CuInS₂) and noble metals manifesting synergistic properties are beneficial to their photocatalytic performances. As Zn-containing semiconductor NCs may have large band gaps, other materials such as CdS and CuS with small band gaps in visible and near-infrared can be used to expand the capability of heterostructures for harvesting more solar spectrum. Yu et al. reported the remarkable improved hydrogen evolution performance of the type-II ZnS-(CdS/Au) hetero-nanorods for hydrogen evolution (Fig. 17d).⁹⁹ Similarly, Cu_{1.94}S-Zn_xCd_{1-x}S hetero-nanorods were proved to have the highest photocatalytic activity for hydrogen production among all the heterostructures with different stoichiometric ratios (Fig. 17c).¹²⁷ Besides, hybrid ZnS-CuInS₂ nanorods also show good performances in the hydrogen evolution reaction (HER) using the visible light.¹¹⁶

The materials engineering of heterostructures for photocatalysis can be further expanded to other materials. Pt-tipped Zn_{0.25}Cd_{0.75}Se alloyed nanorods show the

higher hydrogen evolution efficiency compared with Pt-ZnSe nanorods or single ZnSe nanorods as presented in Fig. 17b.¹⁰³ Cu₂ZnSnS₄-Au nanorods present enhanced catalytic activity than Cu₂ZnSnS₄ nanorods alone.^[115] These results demonstrate the synergistic effect heterostructures that integrate Zn-containing semiconductors with metal particles.¹⁰⁵

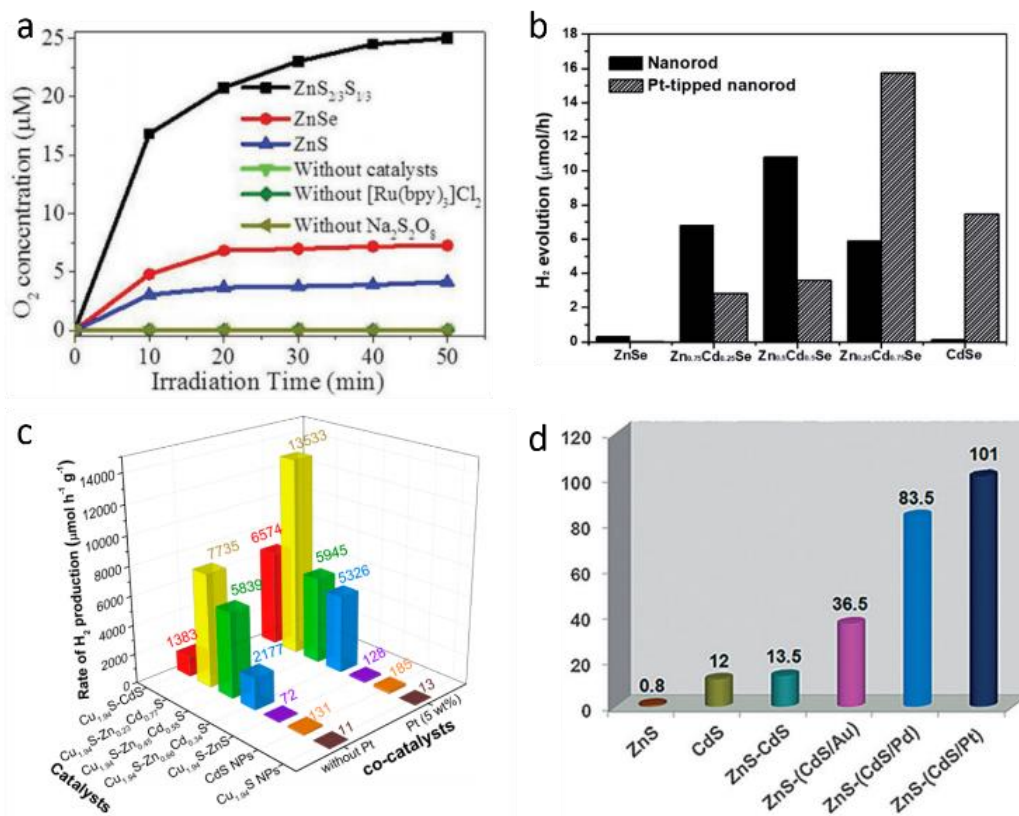


Figure 17. (a) Water oxidation catalytic activities of ZnS, ZnSe, and alloyed ZnS_{2/3}Se_{1/3} quantum rods. Reprinted with permission from Ref.³⁷, Copyright 2018 Wiley-VCH Verlag GmbH & Co. KGaA, Weinheim. (b) Photocatalytic hydrogen evolution rates of the Zn_{1-x}Cd_xSe and Pt-tipped Zn_{1-x}Cd_xSe nanorods (x=0, 0.25, 0.5, 0.75, and 1). Reprinted with permission from Ref.¹⁰³, Copyright 2018 Royal Society of Chemistry. (c) Photocatalytic hydrogen production activities of different ratio of Cu_{1.94}S-Zn_xCd_{1-x}S heteronanorods. Reprinted with permission from Ref.¹²⁷,

Copyright 2016 American Chemical Society. (d) Photocatalytic hydrogen evolution rates using different content of hetero-nanorods. Images of (d) were reprinted with permission from Ref.⁹⁹, Copyright 2015 Wiley-VCH Verlag GmbH & Co. KGaA, Weinheim.

2.6 Summary

In summary, we reviewed the recent advances of zinc-containing semiconductor nanocrystals in synthesis, properties and optoelectronic and energy conversion applications. Engineering of this type of intriguing materials in terms of alloy, core shell structure, doping and hybrid have provided powerful strategies to enhance their properties and leverage their potentials in a wide scope of applications in lighting and displays, photocurrent response and photocatalysis. However, there are still several aspects which need to be addressed in the future to maximize the potentials of zinc-containing semiconductor nanocrystals in aforementioned stimulating applications.

2.7 References

- [1] A. P. Alivisatos, *Science* **1996**, 271, 933.
- [2] P. Reiss, M. Carrière, C. Lincheneau, L. Vaure, S. Tamang, *Chem. Rev.* **2016**, 116, 10731.
- [3] G. Jia, Y. Pang, J. Ning, U. Banin, B. Ji, *Adv. Mater.* **2019**, 31, 1900781.

- [4] P. Li, Z. Wei, T. Wu, Q. Peng, Y. Li, *J. Am. Chem. Soc.* **2011**, *133*, 5660.
- [5] G. Xu, S. Zeng, B. Zhang, M. T. Swihart, K. T. Yong, P. N. Prasad, *Chem. Rev.* **2016**, *116*, 12234.
- [6] D. V. Talapin, J.-S. Lee, M. V. Kovalenko, E. V. Shevchenko, *Chem. Rev.* **2010**, *110*, 389.
- [7] J. Q. Grim, L. Manna, I. Moreels, *Chem. Soc. Rev.* **2015**, *44*, 5897.
- [8] R. Cai, Y. Du, D. Yang, G. Jia, B. Zhu, B. Chen, Y. Lyu, K. Chen, D. Chen, W. Chen, L. Yang, Y. Zhao, Z. Chen, W. Tan, *Nanoscale* **2019**, *11*, 12169.
- [9] S. H. Wei, A. Zunger, *Appl. Phys. Lett.* **1998**, *72*, 2011.
- [10] M. T. Harrison, S. V. Kershaw, M. G. Burt, A. L. Rogach, A. Kornowski, A. Eychmüller, H. Weller, *Pure Appl. Chem.* **2000**, *72*, 295.
- [11] Y. Zhang, H. Xu, Q. Wang, *Chem. Commun.* **2010**, *46*, 8941.
- [12] G. Zhu, S. Zhang, Z. Xu, J. Ma, X. Shen, *J. Am. Chem. Soc.* **2011**, *133*, 15605.
- [13] H. Y. Jung, J. Joo, M. P. Hyun, S. Il Baik, W. K. Young, C. K. Sung, T. Hyeon, *J. Am. Chem. Soc.* **2005**, *127*, 5662.
- [14] S. Sarkar, S. Acharya, A. Chakraborty, N. Pradhan, *J. Phys. Chem. Lett.* **2013**, *4*, 3292.
- [15] A. B. Panda, S. Acharya, S. Efrima, *Adv. Mater.* **2005**, *17*, 2471.
- [16] G. Jia, U. Banin, *J. Am. Chem. Soc.* **2014**, *136*, 11121.
- [17] G. Jia, S. Xu, A. Wang, *J. Mater. Chem. C* **2015**, *3*, 8284.

- [18] M. A. Hines, P. Guyot-Sionnest, *J. Phys. Chem. B.* **1998**, *102*, 3655.
- [19] L. S. Li, N. Pradhan, Y. Wang, X. Peng, *Nano Lett.* **2004**, *4*, 2261.
- [20] L. Carbone, C. Nobile, M. D. Giorgi, F. D. Sala, G. Morello, P. Pompa, M. Hytch, E. Snoeck, A. Fiore, I. R. Franchini, M. Nadasan, A. F. Silvestre, L. Chiodo, S. Kudera, R. Cingolani, R. Krahne, L. Manna, *Nano Lett.* **2007**, *7*, 2942.
- [21] H. Li, R. Brescia, R. Krahne, G. Bertoni, M. J. P. Alcocer, C. D' Andrea, F. Scotognella, F. Tassone, M. Zanella, M. D. Giorgi, L. Manna, *ACS Nano.* **2012**, *6*, 1637.
- [22] V. Lesnyak, A. Plotnikov, N. Gaponik, A. Eychmüller, *J. Mater. Chem.* **2008**, *18*, 5142.
- [23] A. Shavel, N. Gaponik, A. Eychmüller, *J. Phys. Chem. B.* **2004**, *108*, 5905.
- [24] V. Lesnyak, A. Dubavik, A. Plotnikov, N. Gaponik, A. Eychmüller, *Chem. Commun.* **2010**, *46*, 886.
- [25] V. Lesnyak, N. Gaponik, A. Eychmüller, *Chem. Soc. Rev.* **2013**, *42*, 2905.
- [26] H. Li, M. Zanella, A. Genovese, M. Povia, A. Falqui, C. Giannini, L. Manna, *Nano Lett.* **2011**, *11*, 4964.
- [27] H. Li, W. Y. Shih, W. H. Shih, *Nanotechnology* **2007**, *18*, 205604.
- [28] J. Zhang, K. Sun, A. Kumbhar, J. Fang, *J. Phys. Chem. C.* **2008**, *112*, 5454.
- [29] W. E. Buhro, *Polyhedron* **1994**, *13*, 1131.
- [30] M. Green, P. O'Brien, *Chem. Mater.* **2001**, *13*, 4500.
- [31] B. A. Glassy, B. M. Cossairt, *Chem. Commun.* **2015**, *51*, 5283.

- [32] M. Q. Ho, R. J. A. Esteves, G. Kedarnath, I. U. Arachchige, *J. Phys. Chem. C.* **2015**, *119*, 10576.
- [33] B. A. Glassy, N. L. Lai, B. M. Cossairt, *Chem. Mater.* **2017**, *29*, 6195.
- [34] J. Ning, J. Liu, Y. Levi-Kalishman, A. I. Frenkel, U. Banin, *J. Am. Chem. Soc.* **2018**, *140*, 14627.
- [35] P. D. Cozzoli, L. Manna, M. L. Curri, S. Kudera, C. Giannini, M. Striccoli, A. Agostiano, *Chem. Mater.* **2005**, *17*, 1296.
- [36] G. Jia, A. Sitt, G. B. Hitin, I. Hadar, Y. Bekenstein, Y. Amit, I. Popov, U. Banin, *Nat. Mater.* **2014**, *13*, 301.
- [37] D. Chen, H. Zhang, Y. Li, Y. Pang, Z. Yin, H. Sun, L. C. Zhang, S. Wang, M. Saunders, E. Barker, G. Jia, *Adv. Mater.* **2018**, *31*, 1803351.
- [38] Z. Deng, H. Yan, Y. Liu, *Angew. Chem. Int. Ed.* **2010**, *49*, 8695.
- [39] J. Zhang, S. Jin, H. C. Fry, S. Peng, E. Shevchenko, G. P. Wiederrecht, T. Rajh, *J. Am. Chem. Soc.* **2011**, *133*, 15324.
- [40] L. Hou, Q. Zhang, L. Ling, C. X. Li, L. Chen, S. Chen, *J. Am. Chem. Soc.* **2013**, *135*, 10618.
- [41] J. Zheng, M. Xu, J. Liu, X. Cheng, J. Liu, H. Rong, J. Zhang, *Chem. Eur. J.* **2018**, *24*, 2999.
- [42] H. Park, H. Chung, W. Kim, *Mater. Lett.* **2013**, *99*, 172.
- [43] N. S. Karan, S. Sarkar, D. D. Sarma, P. Kundu, N. Ravishankar, N. Pradhan, *J. Am. Chem. Soc.* **2011**, *133*, 1666.
- [44] Y. Wang, Y. Zhou, Y. Zhang, W. E. Buhro, *Inorg. Chem.* **2015**, *54*, 1165.

- [45] A. Narayanaswamy, H. Xu, N. Pradhan, X. Peng, *Angew. Chem. Int. Ed.* **2006**, *45*, 5361.
- [46] J. Zhang, C. Rowland, Y. Liu, H. Xiong, S. Kwon, E. Shevchenko, R. D. Schaller, V. B. Prakapenka, S. Tkachev, T. Rajh, *J. Am. Chem. Soc.* **2015**, *137*, 742.
- [47] S. H. Lee, Y. J. Kim, J. Park, *Chem. Mater.* **2007**, *19*, 4670.
- [48] M. A. Hines, P. Guyot-Sionnest, *J. Phys. Chem. B.* **1998**, *102*, 3655.
- [49] W. Chen, A. Karton, T. Hussian, S. Javaid, F. Wang, Y. Pang, G. Jia, *CrystEngComm* **2019**, *13*, 2955.
- [50] Y. Pang, M. Zhang, D. Chen, W. Chen, F. Wang, S. J. Anwar, M. Saunders, M. R. Rowles, L. Liu, S. Liu, A. Sitt, C. Li, G. Jia, *J. Phys. Chem. Lett.* **2019**, *10*, 3465.
- [51] T. Trindade, P. O'Brien, N. L. Pickett, *Chem. Mater.* **2001**, *13*, 3843.
- [52] R. M. B. Dimmler, R. H. Mauch, H. W. Schock, *J. Cryst. Growth.* **1988**, *86*, 906.
- [53] N. Belman, S. Acharya, O. Konovalov, A. Vorobiev, J. Israelachvili, S. Efrima, Y. Golan, *Nano Lett.* **2008**, *8*, 3858.
- [54] S. Xu, C. Wang, Q. Xu, H. Zhang, R. Li, H. Shao, W. Lei, Y. Cui, *Chem. Mater.* **2010**, *22*, 5838.
- [55] M. H. Mobarok, E. J. Lubner, G. M. Bernard, L. Peng, R. E. Wasylshen, J. M. Buriak, *Chem. Mater.* **2014**, *26*, 1925.
- [56] E. A. Fagen, *J. Appl. Phys.* **1979**, *50*, 6505.

- [57] J. P. Bosco, S. B. Demers, G. M. Kimball, N. S. Lewis, H. A. Atwater, *J. Appl. Phys.* **2012**, *112*, 93703.
- [58] H. Weller, A. Fojtik, A. Henglein, *Chem. Phys. Lett.* **1985**, *117*, 485.
- [59] B. A. Glassy, B. M. Cossairt, *Chem. Mater.* **2016**, *28*, 6374.
- [60] S. Miao, T. Yang, S. G. Hickey, V. Lesnyak, B. Rellinghaus, J. Xu, A. Eychmüller, *Small* **2013**, *9*, 3415.
- [61] S. Miao, D. Chen, A. Madani, M. R. Jorgensen, V. A. Bolaños Quiñones, L. Ma, S. G. Hickey, A. Eychmüller, O. G. Schmidt, *Adv. Opt. Mater.* **2015**, *3*, 187.
- [62] X. Zhong, Y. Feng, W. Knoll, M. Han, *J. Am. Chem. Soc.* **2003**, *125*, 13559.
- [63] X. Zhong, M. Han, Z. Dong, T. J. White, W. Knoll, *J. Am. Chem. Soc.* **2003**, *125*, 8589.
- [64] Y. Zheng, Z. Yang, J. Y. Ying, *Adv. Mater.* **2007**, *19*, 1475.
- [65] Z. Deng, H. Yan, Y. Liu, *J. Am. Chem. Soc.* **2009**, *131*, 17744.
- [66] A. Shavel, N. Gaponik, A. Eychmüller, *J. Phys. Chem. B.* **2004**, *108*, 5905.
- [67] K. Yu, A. Hrdina, J. Ouyang, D. Kingston, X. Wu, D. M. Leek, X. Liu, C. Li, *ACS Appl. Mater. Interfaces* **2012**, *4*, 4302.
- [68] F. Xu, B. Xue, F. Wang, A. Dong, *Chem. Mater.* **2015**, *27*, 1140.
- [69] S. K. Han, M. Gong, Z. M. Wang, C. Gu, S. H. Yu, *Part. Part. Syst. Charact.* **2013**, *30*, 1024.
- [70] V. Lesnyak, R. Brescia, G. C. Messina, L. Manna, *J. Am. Chem. Soc.* **2015**, *137*, 9315.

- [71] J. L. Fenton, B. C. Steimle, R. E. Schaak, *J. Am. Chem. Soc.* **2018**, *140*, 6771.
- [72] T. K. Kormilina, S. A. Cherevko, A. V. Fedorov, A. V. Baranov, *Small* **2017**, *13*, 1.
- [73] B. Ji, Y. E. Panfil, N. Waiskopf, S. Remennik, I. Popov, U. Banin, *Nat. Commun.* **2019**, *10*, 2.
- [74] B. Dong, L. Cao, W. Liu, *Chem. Commun.* **2010**, *46*, 7331.
- [75] Z. Fang, Y. Li, H. Zhang, X. Zhong, L. Zhu, *J. Phys. Chem. C* **2009**, *113*, 14145.
- [76] H. Asano, S. Tsukuda, M. Kita, S. Fujimoto, T. Omata, *ACS Omega* **2018**, *3*, 6703.
- [77] A. Nemchinov, M. Kirsanova, N. N. Hewa-kasakarage, M. Zamkov, *J. Phys. Chem. C* **2008**, *112*, 9301.
- [78] D. Dorfs, A. Salant, I. Popov, U. Banin, *Small* **2008**, *4*, 1319.
- [79] J. Bang, J. Park, J. H. Lee, N. Won, J. Nam, J. Lim, B. Y. Chang, H. J. Lee, B. Chon, J. Shin, J.B. Park, J. H. Choi, K. Cho, S. M. Park, T. J. S. Kim, *Chem. Mater.* **2010**, *22*, 233.
- [80] K. Boldt, C. Ramanan, A. Chanaewa, M. Werheid, A. Eychmüller, *J. Phys. Chem. Lett.* **2015**, *6*, 2590.
- [81] C. M. Tyrakowski, A. Shamirian, C. E. Rowland, H. Shen, A. Das, R. D. Schaller, P. T. Snee, *Chem. Mater.* **2015**, *27*, 7276.
- [82] D. Chen, A. Wang, H. Li, L. A. Galan, C. Su, Z. Yin, M. Massi, A. Suvorova, M. Saunders, J. Li, A. Sitt, G. Jia, *Nanoscale* **2019**, *11*, 10190.

- [83] X. Zhong, R. Xie, Y. Zhang, T. Basché, W. Knoll, *Chem. Mater.* **2005**, *17*, 4038.
- [84] L. P. Balet, S. A. Ivanov, A. Piryatinski, M. Achermann, V. I. Klimov, *Nano Lett.* **2004**, *4*, 1485.
- [85] C. Bouet, D. Laufer, B. Mahler, B. Nadal, H. Heuclin, S. Pedetti, G. Patriarche, B. Dubertret, *Chem. Mater.* **2014**, *26*, 3002.
- [86] R. Xie, X. Zhong, T. Basche, *Adv. Mater.* **2005**, *17*, 2741.
- [87] E. Groeneveld, S. Van Berkum, M. M. Van Schooneveld, A. Gloter, J. D. Meeldijk, D. J. Van Den Heuvel, H. C. Gerritsen, C. De Mello Donega, *Nano Lett.* **2012**, *12*, 749.
- [88] N. Pradhan, D. D. Sarma, *J. Phys. Chem. Lett.* **2011**, *2*, 2818.
- [89] D. J. Norris, N. Yao, F. T. Charnock, T. A. Kennedy, *Nano Lett.* **2001**, *1*, 3.
- [90] N. Pradhan, D. Goorskey, J. Thessing, X. Peng, *J. Am. Chem. Soc.* **2005**, *127*, 17586.
- [91] Y. Yang, O. Chen, A. Angerhofer, Y. C. Cao, *Chem. Eur. J.* **2009**, *15*, 3186.
- [92] Z. J. Li, E. Hofman, A. Blaker, A. H. Davis, B. Dzikovski, D. K. Ma, W. Zheng, *ACS Nano*. **2017**, *11*, 12591.
- [93] P. T. K. Chin, J. W. Stouwdam, R. A. J. Janssen, *Nano Lett.* **2009**, *9*, 745.
- [94] Z. Deng, L. Tong, M. Flores, S. Lin, J. X. Cheng, H. Yan, Y. Liu, *J. Am. Chem. Soc.* **2011**, *133*, 5389.
- [95] S. Acharya, S. Sarkar, N. Pradhan, *J. Phys. Chem. C*. **2013**, *117*, 6006.

- [96] A. Pandey, S. Brovelli, R. Viswanatha, L. Li, J. M. Pietryga, V. I. Klimov, S. A. Crooker, *Nat. Nanotechnol.* **2012**, 7, 792.
- [97] D. A. Bussian, S. A. Crooker, M. Yin, M. Brynda, A. L. Efros, V. I. Klimov, *Nat. Mater.* **2009**, 8, 35.
- [98] R. Costi, A. E. Saunders, U. Banin, *Angew. Chem. Int. Ed.* **2010**, 49, 4878.
- [99] T. T. Zhuang, Y. Liu, M. Sun, S. L. Jiang, M. W. Zhang, X. C. Wang, Q. Zhang, J. Jiang, S. H. Yu, *Angew. Chem. Int. Ed.* **2015**, 54, 11495.
- [100] T. T. Zhuang, Y. Liu, Y. Li, Y. Zhao, L. Wu, J. Jiang, S. H. Yu, *Angew. Chem. Int. Ed.* **2016**, 55, 6396.
- [101] Y. Tian, L. Wang, S. Yu, W. Zhou, *Nanotechnology* **2015**, 26, 325702.
- [102] Y. Tian, W. Zhou, H. Tang, H. Fu, L. Wang, *Chem. Commun.* **2015**, 51, 11818.
- [103] J. Y. Choi, K. M. Nam, H. Song, *J. Mater. Chem. A.* **2018**, 6, 16316.
- [104] B. Ji, Y. E. Panfil, U. Banin, *ACS Nano.* **2017**, 11, 7312.
- [105] K. P. Acharya, R. S. Khnayzer, T. O'Connor, G. Diederich, M. Kirsanova, A. Klinkova, D. Roth, E. Kinder, M. Imboden, M. Zamkov, *Nano Lett.* **2011**, 11, 2919.
- [106] N. N. Hewa-kasakarage, K. P. Z. El-khoury, K. A. N. Tarnovsky, M. Kirsanova, I. Nemitz, A. Nemchinov, M. Zamkov, *ACS Nano.* **2010**, 4, 1837.
- [107] M. Kirsanova, A. Nemchinov, N. N. Hewa-Kasakarage, N. Schmall, M. Zamkov, *Chem. Mater.* **2009**, 21, 4305.
- [108] S. Yadav, B. Adhikary, P. Tripathy, S. Sapra, *ACS Omega.* **2017**, 2, 2231.
- [109] P. Adel, A. Wolf, T. Kodanek, D. Dorfs, *Chem. Mater.* **2014**, 26, 3121.

- [110] R. Xie, U. Kolb, T. Basché, *Small* **2006**, 2, 1454.
- [111] A. Fiore, R. Mastria, M. G. Lupo, G. Lanzani, C. Giannini, E. Carlino, G. Morello, M. De Giorgi, Y. Li, R. Cingolani, L. Manna, *J. Am. Chem. Soc.* **2009**, 131, 4300.
- [112] R. Xie, M. Zhou, *Chem. Mater.* **2015**, 27, 3055.
- [113] A. Dalui, A. Chakraborty, U. Thupakula, A. H. Khan, S. Sengupta, B. Satpati, D. D. Sarma, I. Dasgupta, S. Acharya, *J. Phys. Chem. C* **2016**, 120, 10118.
- [114] T. Kameyama, S. Koyama, T. Yamamoto, S. Kuwabata, T. Torimoto, *J. Phys. Chem. C* **2018**, 122, 13705.
- [115] P. S. Dilsaver, M. D. Reichert, B. L. Hallmark, M. J. Thompson, J. Vela, *J. Phys. Chem. C* **2014**, 118, 21226.
- [116] C. Ye , M. D. Regulacio , S. H. Lim, S. Li, Q.-H. Xu, M.-Y. Han, *Chem. Eur. J.* **2015**, 21, 9514.
- [117] C. Xiang, W. Koo, S. Chen, F. So, X. Liu, X. Kong, Y. Wang, *Appl. Phys. Lett.* **2012**, 101, 053303.
- [118] A. Wang, H. Shen, S. Zang, Q. Lin, H. Wang, L. Qian, J. Niu, L. S. Li, *Nanoscale* **2015**, 7, 2951.
- [119] Q. Lin, H. Shen, H. Wang, A. Wang, J. Niu, L. Qian, F. Guo, L. S. Li, *Org. Electron.* **2015**, 25, 178.
- [120] X. Yuan, J. Hua, R. Zeng, D. Zhu, W. Ji, P. Jing, X. Meng, J. Zhao, H. Li, *Nanotechnology* **2014**, 25, 435202.

- [121] X. Xu, S. Li, J. Chen, S. Cai, Z. Long, X. Fang, *Adv. Funct. Mater.* **2018**, 28, 1802029.
- [122] D. Li, G. Xing, S. Tang, X. Li, L. Fan, Y. Li, *Nanoscale*. **2017**, 9, 15044.
- [123] D. Li, S. Hao, G. Xing, Y. Li, X. Li, L. Fan, S. Yang, *J. Am. Chem. Soc.* **2019**, 141, 3480.
- [124] N. Guijarro, M. S. Prévot, K. Sivula, *J. Phys. Chem. Lett.* **2014**, 5, 3902.
- [125] M. F. Kuehnel, C. E. Creissen, C. D. Sahm, D. Wielend, A. Schlosser, K. L. Orchard, E. Reisner, *Angew. Chem. Int. Ed.* **2019**, 58, 5059.
- [126] D. Kandi, S. Martha, K. M. Parida, *Int. J. Hydrog. Energy*. **2017**, 42, 9467.
- [127] Y. Chen, S. Zhao, X. Wang, Q. Peng, R. Lin, Y. Wang, R. Shen, X. Cao, L. Zhang, G. Zhou, J. Li, A. Xia, Y. Li, *J. Am. Chem. Soc.* **2016**, 138, 4286.

3 Spontaneous Formation of Noble- and Heavy-Metal Free Alloyed Semiconductor Quantum Rods for Efficient Photocatalysis

(Chapter 3 was adapted with permission from D. Chen, H. Zhang, Y. Li, Y. Pang, Z. Yin, H. Sun, L.-C. Zhang, S. Wang, M. Saunders, E. Barker and G. Jia, *Adv. Mater.*, 2018, 30, 1803351. Copyright 2018 Wiley-VCH Verlag GmbH & Co. KGaA, Weinheim.)

3.1 Abstract

Quasi-one-dimensional cadmium chalcogenide quantum rods (QRs) are benchmark semiconductor materials that have been combined with noble metals to constitute QR heterostructures for efficient photocatalysis. However, the high toxicity of cadmium and cost of noble metals are the main obstacles to their widespread use. Herein we report a facile colloidal synthetic approach that leads to the spontaneous formation of cadmium-free alloyed $\text{ZnS}_x\text{Se}_{1-x}$ QRs from polydisperse ZnSe nanowires by the etching of alkylthiol. The obtained non-noble metal $\text{ZnS}_x\text{Se}_{1-x}$ QRs can not only be directly adopted as efficient photocatalysts for water oxidation, showing a striking oxygen evolution capability of $3000 \mu\text{mol g}^{-1} \text{h}^{-1}$, but also be utilized to prepare QRs-sensitized TiO_2 photoanodes which present enhanced photoelectrochemical (PEC) activity. Density functional theory (DFT) simulations reveal that alloyed $\text{ZnS}_x\text{Se}_{1-x}$ QRs have highly active Zn sites on the (100) surface and reduced energy barrier for

oxygen evolution, which in turn, are beneficial to their outstanding photocatalytic and PEC activities.

3.2 Introduction

Oxygen evolution reaction (OER) is a key process and the bottleneck in water splitting as the production of H₂ is severely constrained by the sluggish kinetics of OER.¹⁻⁴ Consequently, a substantial overpotential is required to drive the OER even with the benchmark precious catalysts such as IrO₂ and RuO₂.⁵⁻⁷ However, these noble metals are costly and are not suitable for large scale industrial applications. Therefore, tremendous efforts have been devoted to the development of efficient, abundant and inexpensive catalysts, such as oxides,^{3,7,8} hydroxides,^{4,9-11} chalcogenides¹²⁻¹⁴ and phosphides.¹⁴⁻¹⁵

As the benchmark materials for photocatalytic hydrogen production, cadmium chalcogenide based QR heterostructures, such as CdS-Pt,¹⁶⁻²² CdS-PdX^{18,23} and CdS-Au,^{24,25} have been studied extensively over the years because they have appropriate band gap energies and efficient charge separation capabilities, which provide an adequate driving force for hydrogen evolution. However, QR heterostructures containing both cadmium and noble metal suffer from a high toxicity and a high cost. For example, cadmium based QRs are highly toxic and their synthesis typically involves the use of toxic reagents such as phosphonic acid and phosphonic oxide.²⁶⁻²⁹ The ideal alternatives to cadmium chalcogenides could be zinc chalcogenide QRs as they have an appropriate band gap energy and can be prepared by a phosphine-free protocol. Unfortunately, zinc precursors will form a lamellar structure in organic

solution before they react with chalcogen anions, i.e. S^{2-} , Se^{2-} and Te^{2-} .³⁰ In such a case, the obtained zinc chalcogenide nanowires maintain their original lamellar structure, making them very hard to facilitate the anisotropic growth.³¹⁻³⁴ Although there are some reports on the synthesis of zinc chalcogenide QRs based on the epitaxial growth and thermodynamically driven material diffusion mechanisms,^{31,35-39} it is still a challenge to prepare zinc chalcogenide QRs with monodispersity.

3.2 Experimental Section and Methods

Chemicals: $Zn(NO_3)_2 \cdot 6H_2O$ (99%), $ZnCl_2$ (99.995%), zinc diethyldithiocarbamate (97%), selenium powder (99.999%), bis(trimethylsilyl)sulfide (98%) $((TMS)_2S)$, 1-dodecanethiol (98%) (DDT), 1-hexadecanethiol (99%) (HDT), 1-octadecanethiol (98%) (ODT), oleylamine (approximate C_{18} content 80-90%), chloroform (99% anhydrous), and methanol (99.8% anhydrous) were purchased from Sigma-Aldrich. All chemicals were used as received without further purification.

Preparation of Zinc Precursor Stock Solution: A 0.067 M zinc stock solution was prepared by mixing $ZnCl_2$ (0.2 mmol, 27.3 mg) with oleylamine (10 mL) in a three-neck flask. The mixture was degassed and refilled with N_2 three times at room temperature. Then it was heated to 110 °C and kept at this temperature for 30 minutes under vacuum. Then the mixture was further heated up to 160 °C and kept at this temperature for 30 minutes.

Synthesis of Alloyed ZnS_xSe_{1-x} Quantum Rods (QRs): ZnSe nanowires were synthesized according to a reported approach.³¹ 30 mg purified ZnSe nanowires were dissolved in 15 mL oleylamine in a three-neck flask and then 4 mL 0.067 M zinc

precursor stock solution was added into the flask. The mixture was degassed and refilled with N₂ three times at room temperature and then heated to 110 °C and kept at this temperature for 30 minutes under vacuum. Then the mixture was heated to 260 °C from 110 °C in 7 minutes. At 260 °C, a certain amount of DDT was injected into the flask. After the injection, the temperature was raised to 280 °C in four minutes. After 30 minutes at 280 °C, the reaction was quenched by removing the heating mantle. Aliquots have been taken from time to time to monitor the growth of nanoparticles. The synthesis conditions of QRs using other sulfur sources such as HDT, ODT and (TMS)₂S are identical to those of the above synthesis except that DDT has been replaced to one of these sulfur sources. A same synthetic approach has been utilized to prepare nearly monodisperse ZnS QRs from polydisperse ZnS nanowires.

Sample Characterization: UV-vis absorption spectroscopy was performed on a Perkin Elmer Lambda 35 UV/VIS Spectrometer. Photoluminescence spectra were recorded using a Cary Eclipse luminescence spectrophotometer. Powder X-ray diffraction (XRD) patterns were obtained using Cu K α ($\lambda=1.5406$ Å) photons from an X'per PRO (PANalytical) X-ray diffractometer operated at 40 kV and 40 mA. Transmission electron microscopy (TEM) was performed using a JEOL 2100 transmission electron microscope. High-resolution TEM (HRTEM), high angle annular dark field-scanning transmission electron microscopy (HAADF-STEM) and STEM-energy-dispersive X-ray spectroscopy (STEM-EDX) were performed on an FEI Titan G2 80-200 high-resolution transmission electron microscope. X-ray photoelectron spectroscopy (XPS) measurements were performed on a Kratos Axis Ultra DLD spectrometer equipped with a monochromatic AlK α (1486.6 eV)

irradiation source operating at an X-ray gun power of 150 W. The vacuum pressure of the analysis chamber of the spectrometer was maintained at 8×10^{-9} Torr or lower throughout the duration of the analyses. The binding energy scale was calibrated for each sample by setting the main line of the C 1s spectrum to 284.8 eV. XPS spectra were collected with pass energy of 160 eV for the survey spectra and 40 eV for the high-resolution spectra. Background subtractions using a Shirley background were applied to all survey and high resolution spectra. Each high-resolution spectra were fitted with a Gaussian-Lorentzian (70%-30%) line shape with the full-width half maximum (FWHM) constrained to values considered reasonable for each element.

Photocatalytic Oxygen Evolution Reaction (OER) Test: In a typical catalytic test, 8 mg catalysts were dispersed in 50 mL phosphate buffer solution with a pH value of 6.8, followed by adding 0.49 g Na_2SO_4 , 0.18 g $\text{Na}_2\text{S}_2\text{O}_8$ and 0.03 g $[\text{Ru}(\text{bpy})_3]\text{Cl}_2 \cdot 6\text{H}_2\text{O}$. After this, the solution was transferred to a sealed double jacketed reactor (800 mL). The reactor has a quartz window which connected to an on-line gas chromatograph (Agilent 490 Micro GC) with a thermal conductivity detector. To completely remove air in the reactor, N_2 was pumped in for 30 min. Then, the solution was stabilized in the dark for 10 min, which was probed as the baseline. The solution was irradiated via a 300 W Xeon lamp (Newport) and aligned to 200 mW/cm^2 (2 suns) to start the reaction. The reaction temperature was maintained at 25°C by a flow of cooling water, controlled by a thermostatic water bath.

Apparent Quantum Efficiency (AQE) Measurement: AQE for photocatalytic OER was detected at the same experimental condition through a band-pass filter ($\lambda=380/420 \text{ nm}$). The photo flux of incident light was determined using a

spectroradiometer (DeltaOHM, LP471 UVA/RAD, resolution, $0.01 \mu\text{mol m}^{-2} \text{s}^{-1} / 0.1 \times 10^{-3} \text{ W m}^{-2}$). AQE was calculated by the following formula:

$$\text{AQE} = \frac{4 \times \text{evolved O}_2 \text{ molecule number}}{\text{Indicent photon number}} \times 100\%$$

Preparation of Working Electrode: 25 μL Nafion® 117 solution were added into a 500 μL of the QR suspension solution by sonication. Then 10 μL of the catalyst ink was dripped onto a glassy carbon electrode (5.0 mm in diameter) and dried in air.

Preparation of TiO₂ Coated Photoanode: Fluorine-doped SnO₂ (FTO)-coated glass substrates were cleaned by immersion in acetone, ethanol, and deionized water for 10 min each with sonication and dried under a N₂ stream. The cleaned substrates were soaked in the TiCl₄ (40 mM) under 70 °C for 30 mins, washed with ethanol for several times and further annealed under 400 °C for another 30 mins. Next, the commercial TiO₂ pastes were diluted 10-folds and spin-coated onto the above substrate for several times. The coated glasses were annealed under 450 °C for 1 hour to obtain the final photoanode.

QRs Sensitization: The above TiO₂ photoanode were sensitized with QRs using a chemical bath deposition (CBD) approach. In a typical procedure, the TiO₂ photoanode was immersed in the QRs, i.e. ZnS, ZnSe and ZnS_{2/3}Se_{1/3}, trichloromethane dispersion under 60 °C for 12 h and then dried with a N₂ stream. We carried out two CBD cycles for each photoanode.

Photoelectrochemical (PEC) Experiments: All PEC studies were operated on an electrochemical workstation on a Zennium workstation (Zahner, Germany) in a three-electrode framework, with Ag/AgCl as the reference electrode and Pt wire as the counter electrode. The above QRs sensitized TiO₂ photoanodes were adopted as

the working electrode. Measurements were performed in a 0.2 M Na₂SO₄ solution (pH 6.8) solution as supporting electrolyte medium. All potentials were converted into reversible hydrogen electrode (RHE) values based on equation:

$$E_{\text{RHE}} = E_{\text{Ag/AgCl}} + 0.059\text{pH} + 0.197 \text{ V}$$

The photocurrent of the photoanode was measured by current-voltage (J-V) curve at a scan rate of 10 mV s⁻¹ and was illuminated at 100 m W cm⁻² from a 300 W xenon lamp. Prior to the test, the internal light was filtered using a neutral density filter and an AM 1.5G filter into an optical fiber. Amperometric current-time (i-t) curves of the photoanodes were recorded under chopped light irradiation at an open circuit potential of each photoanode.

Oxygen Measurements: The setup of oxygen measurements was same as the PEC test excepted that a oxygen sensor (Ocean Optics, Neofox, FOSPOR-R 1/16) was inserted into the reactor to probe the O₂ concentration via the fluorescence quenching method. The PEC reactor was a customized airtight glass cell with a quartz window (the volume of the headspace, excluding the space occupied by the septum, oxygen sensor, and the solution, was 20 mL). The needle probe was inserted into the 1/16" threaded holes through a rubber septum and conducted uninterrupted O₂ readings at 5 seconds intervals throughout the test. Ahead of the detecting, the probe was calibrated through 2 points method (air, 20.9% O₂ and Nitrogen, 0% O₂), with a reading error of 1%. Before irradiation, the reactor was purged with nitrogen for 10 mins to exclude air and guarantee anaerobic circumstances in the reaction system. The test started with 10 mins of baseline O₂ reading followed by 100 mins of irradiation of AM 1.5G simulated solar light (light intensity: 1 sun or 100 mW cm⁻²) with the potentiostatic method (1.23 V vs. RHE). The probe measures the O₂

exponent in the headspace and records as $\mu\text{mol/L}$. This was converted to μmol after first adjusting for the O_2 dissolved in solution by Henry's Law.

Measurement of Faradic Efficiency (FE): FE describes the transfer efficiency of electric charge in an electrochemical reaction system, and it is the ratio between the utilized charge by reactants and the amount of total charge of the external circuits. The oxygen generated during the PEC process was measured in real-time by using a NeoFox Sport Oxygen Sensor (Ocean Optics). For the calculation of the FE of the water splitting (η_{faradic}) in the configuration of short-circuited electrodes, the following equation was applied:⁴⁰

$$\eta_{\text{faradic}} = \frac{4 \times n_{\text{O}_2}(\text{mol}) \times 96485 (\text{C/mol})}{Q(\text{C})} \times 100\%$$

in which Q is the total amount of charge passed through the external circuit during the same time period as the measurement of evolved O_2 gas.

Electrochemical Active Surface Area (EASA) Test: EASA of the samples were conducted in a three-electrode electrochemical system using a rotating disk electrode (RDE) configuration (Pine Instrument Company, USA), which is controlled by a Gamry electrochemical workstation.^{40,41} Ag/AgCl (KCl sat.) and Pt wire were adopted as the reference electrode and the counter electrode, respectively.

Density Functional Theory (DFT) Simulations: DFT calculations were performed using the Vienna *Ab initio* Simulations Package (VASP)^{42,43} and projected augmented wave (PAW)⁴⁴⁻⁴⁶ method (with $2s^22p^4$, $3s^23p^4$, $4s^24p^4$, $3d^{10}4s^2$ treated as valence electrons for O, S, Se and Zn, respectively). The exchange-correlation interaction was treated with generalized gradient approximation (GGA) in the Perdew, Burke and Ernzerhof (PBE)⁴⁷ parameterization. For strongly localized d

electrons, GGA has systematic and noncancelling errors.⁴⁸ Therefore, we adopted GGA+U (U=8 and J=1)^{49,50} and the hybrid functional (PBE0)^{51,52} to correct the self-interaction and overdelocalized *d* states. The cutoff energy of plane-wave basis was set to 450 eV, and integrations over the first Brillouin zone were calculated using a Gamma-centred **k**-point set of 6×6×4. With these settings, the total energy was able to converge within 1 meV/atom. The wurtzite structure (space group *P6₃mc*, No. 186) of ZnS, ZnSe, ZnS_{0.5}Se_{0.5} and ZnS_{2/3}Se_{1/3} were fully relaxed using GGA+U, and the energy was converged within 10⁻⁶ eV/cell and the force was converged to less than 10⁻⁴ eV/Å. Electronic structure and band alignment were then obtained by using PBE0 in the bulk and slab calculations, respectively, with the same cutoff energy and similar **k**-point density. A vacuum spacing no less than 15 Å was used in all slab calculations.

The study of OER was then performed on the (100) surface. Gibbs free energy changes for the four elementary steps of OER were calculated accordingly by following equations:^{48,53}

$$\begin{aligned}
\Delta G_1 &= G(*\text{OH}) - G(*) - G(\text{OH}) \\
&= E(*\text{OH}) + 0.5E(\text{H}_2) - E(*) - E(\text{H}_2\text{O}) - eU + k_B T \ln(a_{\text{H}^+}) \\
&\quad + \Delta \text{ZPE} - T\Delta S \\
\Delta G_2 &= G(*\text{O}) + G(\text{H}) - G(*\text{OH}) \\
&= E(*\text{O}) + 0.5E(\text{H}_2) - E(*\text{OH}) - eU + k_B T \ln(a_{\text{H}^+}) + \Delta \text{ZPE} \\
&\quad - T\Delta S
\end{aligned}$$

$$\begin{aligned}
\Delta G_3 &= G(*\text{OOH}) - G(\text{OH}) - G(*\text{O}) \\
&= E(*\text{OOH}) - E(*\text{O}) + 0.5E(\text{H}_2) - E(\text{H}_2\text{O}) - eU + k_B T \ln(a_{\text{H}^+}) \\
&\quad + \Delta \text{ZPE} - T\Delta S
\end{aligned}$$

$$\Delta G_4 = 4 \times [1.23 \text{ eV} - eU + k_B T \ln(a_{\text{H}^+})] - (\Delta G_1 + \Delta G_2 + \Delta G_3)$$

where $E(\text{H}_2)$, $E(\text{H}_2\text{O})$, $E(*)$, $E(*\text{OH})$, $E(*\text{O})$, and $E(*\text{OOH})$ are DFT total energies for hydrogen molecule, water molecule, and catalysis surfaces without and with OH, O and OOH, respectively. $G(*)$, $G(*\text{O})$, $G(*\text{OH})$, and $G(*\text{OOH})$ are the Gibbs free energies of the surfaces without and with O, OH and OOH species, respectively. k_B is the Boltzmann constant and T is temperature (300 K). ZPE is the abbreviation for zero-point energy. S denotes entropy. Details of the treatment of these parameters have been reported previously in the literature.⁵⁴

3.4 Results and discussion

Here, we report that nearly monodisperse alloyed $\text{ZnS}_x\text{Se}_{1-x}$ QRs can be facily obtained from their polydisperse ZnSe nanowire counterparts in the presence of alkylthiol at elevated temperatures. This simple, but generic, approach produces nearly monodisperse heavy metal-free colloidal semiconductor QRs that could not be easily obtained by the conventional colloidal synthetic approaches. Without further calcination, the obtained QRs can be directly employed as photocatalysts for OER in water splitting. The alloyed $\text{ZnS}_x\text{Se}_{1-x}$ QRs are noble- and heavy-metal-free, demonstrating both highly efficient catalytic activities of OER and enhanced PEC performance.

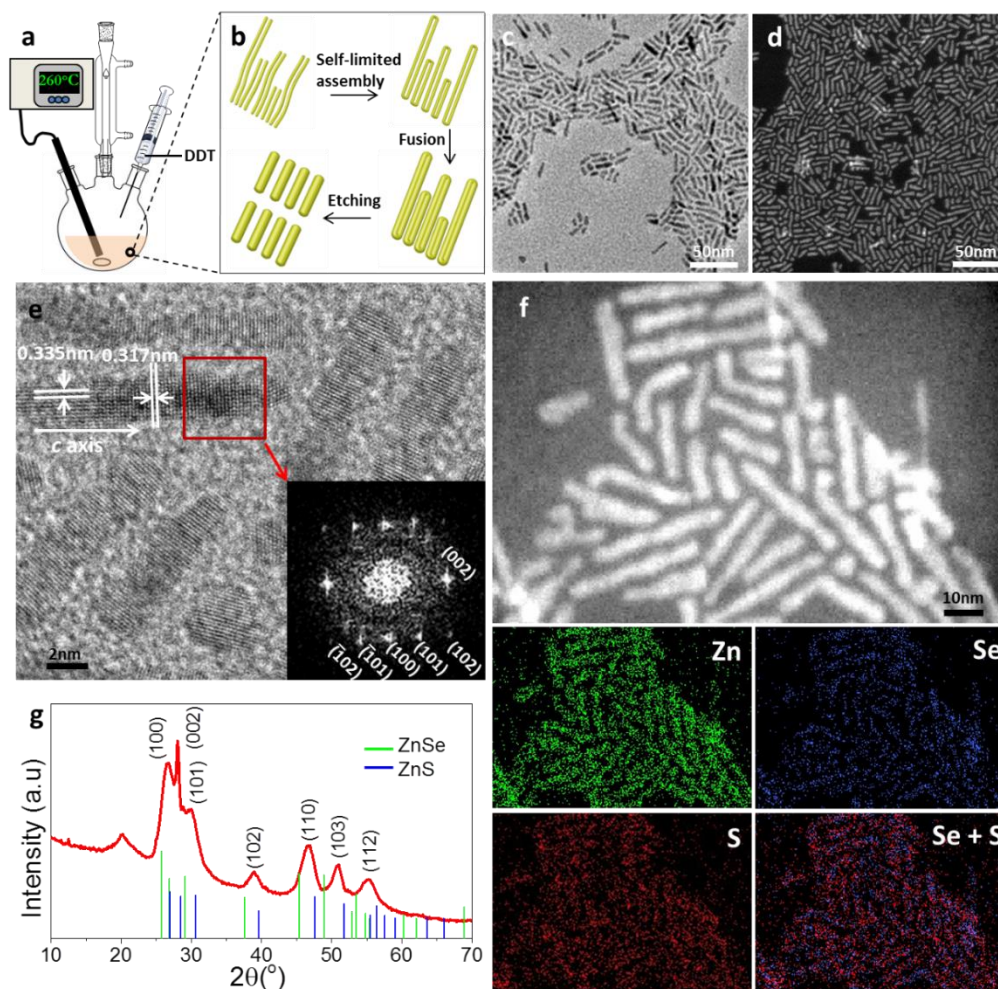


Figure 1. a) Scheme of the experimental setup. b) Schematic illustration of the formation of QRs. c) TEM image. d) STEM image. e) HRTEM image of QRs. Inset in e) is the FFT of selected areas of alloyed $\text{ZnS}_x\text{Se}_{1-x}$ QRs, revealing the crystallographic relations. White lines indicate the orientation of selected crystal planes and arrow shows the orientation of long axis of QRs. f) HAADF-STEM image and STEM-EDX element maps. g) XRD pattern of QRs. Standard XRD patterns for both wurtzite ZnSe (PDF#15-0105) and ZnS (PDF#36-1450) were given for reference.

To synthesize zinc chalcogenide QRs, we took the advantage of the ease with which zinc chalcogenide forms ultrathin nanowires while intentionally added alkylthiol as an external input during their growth at elevated temperatures. Our synthesis is based on a colloidal chemical synthetic route (see the scheme in Figure 1a). Figure 1b shows the schematic illustration of the formation of alloyed $\text{ZnS}_x\text{Se}_{1-x}$ QRs: Starting with polydisperse ultrathin ZnSe nanowires, paired rods are formed in the presence of 1-dodecanethiol (DDT) via a self-limited assembly mechanism;³⁹ then each two rod components of a paired rod form a single rod with a large diameter through intraparticle fusion, and finally the etching of DDT leads to the formation of nearly monodisperse alloyed $\text{ZnS}_x\text{Se}_{1-x}$ QRs. Transmission electron microscope (TEM) images (Figure 1c) and high angle annular dark field-scanning transmission electron microscopy (HAADF-STEM) (Figure 1d) image show the predominantly elongated features of the alloyed $\text{ZnS}_x\text{Se}_{1-x}$ QRs with an aspect ratio of ~ 5 . Statistics on the size of the alloyed QRs show the uniformity of both length ($16.3 \pm 4.3 \text{ nm}$) and diameter ($3.6 \pm 0.7 \text{ nm}$).

High-resolution TEM (HRTEM) characterization reveals high crystallinity with lattice fringes throughout the whole particles (Figure 1e). The lattice planes marked in Figure 1e are perpendicular to each other and the extracted lattice distances of 3.17 \AA and 3.35 \AA correspond to the (002) and (100) planes of the wurtzite structure. Fast Fourier transform (FFT) analysis of the selected area of a QR (red rectangle in Figure 1e and the inset) shows the crystallographic relations, corroborating the wurtzite structure. The derived lattice plane spacings of 3.17 \AA (002) and 3.35 \AA (100) of QRs show a slight shrinkage with respect to the 3.25 \AA (002) and 3.43 \AA (100) planes of the standard wurtzite ZnSe (PDF#15-0105), suggesting that the obtained

crystal lattices are constrained. We further conducted STEM-energy-dispersive X-ray spectroscopy (STEM-EDX) and X-ray diffraction (XRD) to elucidate the reason that is responsible for this shrinkage of the crystal lattices.

STEM-EDX element maps show that both Zn and Se are evenly distributed throughout the elongated QRs (Figure 1f). Since DDT has been intentionally added into the react system during the growth of the nanoparticles, we also acquired a STEM-EDX element map on S. The element map for S clearly shows that a homogeneous distribution of S element throughout the nanoparticles is seen, indicating the formation of alloyed $\text{ZnS}_x\text{Se}_{1-x}$ QRs. XRD analysis shows that the obtained QRs crystallize into wurtzite structure (Figure 1g) and the sharp peak of the (002) plane confirms the long axis direction. All diffraction peaks shift to large angles, indicating the obtained QRs have smaller crystal lattices in regard to the standard wurtzite ZnSe. The results on XRD measurement are consistent with our crystallographic interpretations based on the HRTEM characterization, in which smaller lattice plane spacings are derived, corroborating the formation of alloyed $\text{ZnS}_x\text{Se}_{1-x}$ QRs.

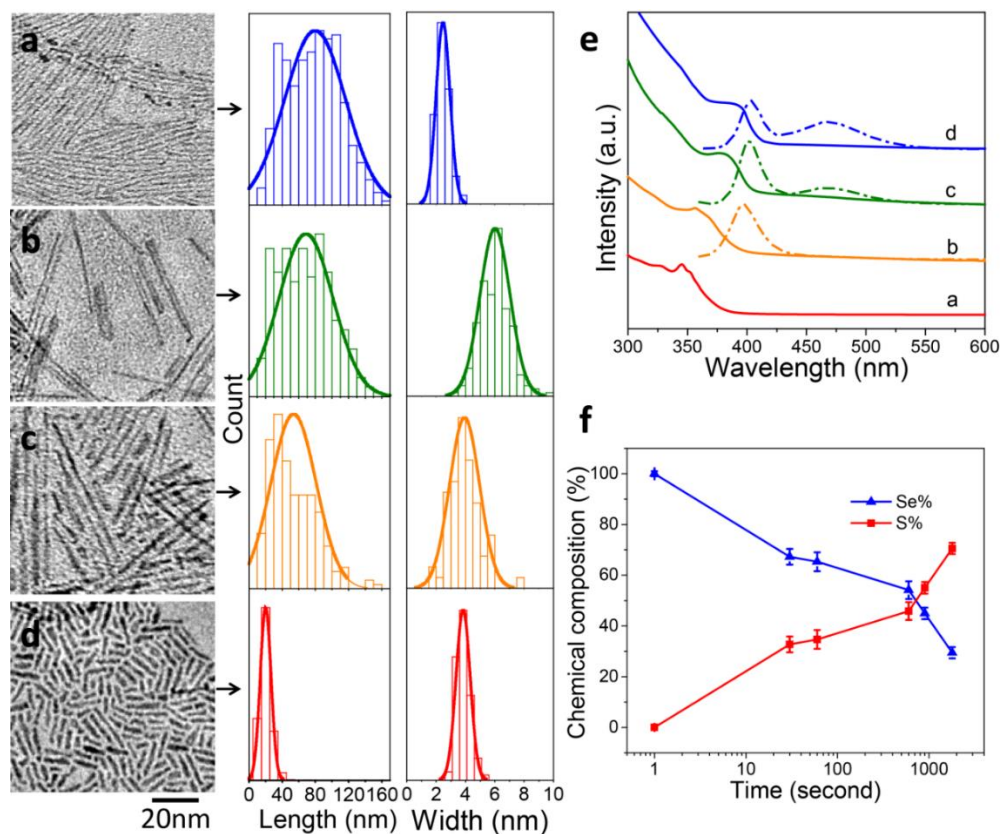


Figure 2. a-d) TEM images and sizing histograms of the aliquots and final products. a) original ZnSe nanowires, b-d) ZnSe QRs evolved from ZnSe nanowires after b) 30 seconds at 260 °C, c) 5 minutes at 280 °C, and d) 30 minutes at 280 °C. The sizing histograms on length and width were shown on the right-hand side of each TEM image. e) Absorption (solid line) and photoluminescence spectra (dash dotted line) of the nanoparticles. The original ZnSe nanowires do not show any detectable luminescence so the luminescence spectrum is not included in e). f) Chemical composition of Se (%) and S (%) of alloyed $\text{ZnS}_x\text{Se}_{1-x}$ nanoparticles as a function of reaction time. Points in f) correspond to the original ZnSe nanowires and five aliquots, which were taken after the reaction evolved for 30 seconds at 260 °C, 1 minutes at 280 °C, 10 minutes at 280 °C, 15 minutes at 280 °C, and 30 minutes at 280 °C.

In the next step, we combined TEM characterization with optical absorption spectroscopy (**Figure 2**) to reveal the growth mechanism of alloyed $\text{ZnS}_x\text{Se}_{1-x}$ QRs, as schematically shown in Figure 1b. Polydisperse ZnSe nanowires (length $80\pm 37\text{nm}$, width $2.4\pm 0.6\text{nm}$, Figure 2a) have been synthesized using a literature method.³¹ The obtained ZnSe nanowires were separated from the crude solution by dissolving into chloroform and precipitating by methanol with the aid of centrifugation. Subsequently, they were re-dissolved into the oleylamine solution, in which zinc precursor stock solution was added to prevent the ripening of the ZnSe nanowires at elevated temperatures. DDT was swiftly injected into the react mixture when the temperature of the system reached 260 °C. Within 30 minutes at 260-280 °C, TEM measurements on aliquots show that the initial pairing of nanowires leads to paired rod (Figure 2b), which subsequently undergo intraparticle fusion to form thick QRs (Figure 2c), and finally polydisperse QRs break down, producing nearly monodisperse alloyed $\text{ZnS}_x\text{Se}_{1-x}$ QRs due to DDT etching (Figure 2d).

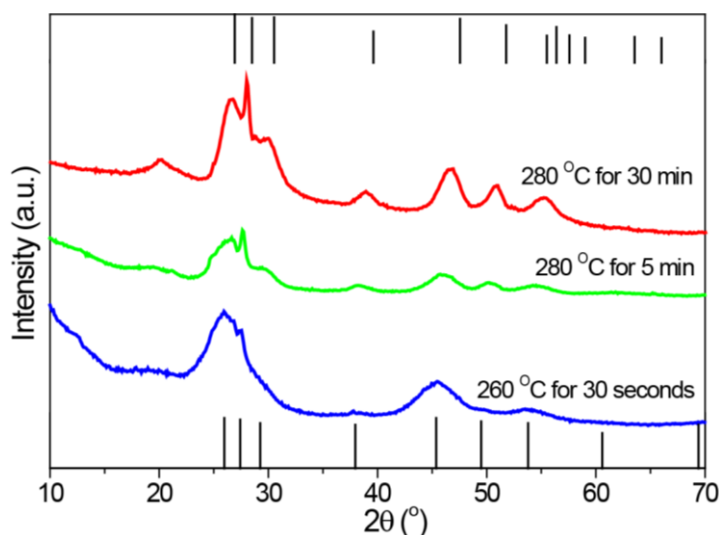


Figure 3. Comparison of XRD patterns of the intermediate and final products during the formation of alloyed $\text{ZnS}_x\text{Se}_{1-x}$ QRs from ZnSe nanowires. The standard XRD patterns for both wurtzite ZnSe (bottom) and wurtzite ZnS (top) were given for reference.

Starting with long ZnSe nanowires (length $80 \pm 37 \text{ nm}$, width $2.4 \pm 0.6 \text{ nm}$, Figure 2a), the length of the nanoparticles slightly shrunk to $69 \pm 32 \text{ nm}$ while the width increased to $6.3 \pm 0.8 \text{ nm}$ as the reaction evolved for 30 seconds at 260°C (Figure 2b) in the presence of DDT. The large increase of the width of the nanoparticles from $2.4 \pm 0.6 \text{ nm}$ to $6.3 \pm 0.8 \text{ nm}$ is associated with the pairing of the proceeding ZnSe nanowires (Figure 2b). The diffraction peaks of the sample in Figure 2b show a small shift of 0.17 degrees to high angles with respect to the standard XRD pattern of wurtzite ZnSe (Figure 3). After the reaction was evolved for 30 seconds at 260°C , it was heated to 280°C within four minutes. As the reaction evolved for 5 minutes at 280°C , the gap between two rod components of each paired rod vanishes, and therefore two rod components form a thick QR by intraparticle fusion (Figure 2c). Accordingly, the length of the obtained QRs becomes $54 \pm 27 \text{ nm}$ and their width is $3.9 \pm 0.9 \text{ nm}$, being much smaller compared with the width of the proceeding paired rods, which is $6.3 \pm 0.8 \text{ nm}$. Further reaction at this temperature for 30 minutes produced nearly monodisperse QRs (length $20 \pm 6 \text{ nm}$, width $3.9 \pm 0.4 \text{ nm}$) (Figure 2d). The absorption onset was red-shifted from 345 nm to 398 nm , 401 and then to 403 nm after 30 seconds at 260°C , 5 minutes and 30 minutes at 280°C , respectively (Figure 2e), being consistent with the increase in the width of the produced nanoparticles. The shift of diffraction peaks of the obtained products showed a shift

from 0.23 and 0.60 degrees as the reaction evolved for 5 min and 30 min at 280 °C, respectively (Figure 3). This continuous shift corresponds to the shrinking of the lattice spacings (Table 1). EDX measurement on these aliquots reveals a decreasing trend of the chemical composition of Se while that of S are gradually increasing as the reaction proceeds (Figure 2f), reaching a ratio of ~2:1 for S:Se for the final products of alloyed $\text{ZnS}_x\text{Se}_{1-x}$ QRs. This clearly shows that some of the Se^{2-} anions in ZnSe is gradually substituted by S^{2-} as the reaction proceeds in the presence of DDT at elevated temperatures, leading to the spontaneous formation of nearly monodisperse alloyed $\text{ZnS}_x\text{Se}_{1-x}$ QRs.

Table 1. Comparison of lattice parameters of intermediate and final products during the formation of alloyed $\text{ZnS}_x\text{Se}_{1-x}$ QRs from ZnSe nanowires.

Product	Diffraction angle of (002)	Shift of angle of (002) with respect to ZnSe	Spacing of (002)
ZnSe	27.42	0	0.32500
$\text{ZnS}_{0.33}\text{Se}_{0.67}$ (30 seconds 280 °C)	27.59	0.17	0.32305
$\text{ZnS}_{0.46}\text{Se}_{0.54}$ (5 min 280 °C)	27.65	0.23	0.32236
$\text{ZnS}_{2/3}\text{Se}_{1/3}$ (30 min 280 °C)	28.02	0.60	0.31819

°C)

ZnS	28.50	1.08	0.31292
-----	-------	------	---------

Except for the original ZnSe nanowires, all the aliquots and final products show detectable photoluminescence with a trap state broad emission band at longer wavelengths due to the imperfect passivation of the obtained nanoparticles (Figure 2e). Our previous studies on the synthesis of ZnSe nanoparticles demonstrate that ZnSe nanowires retain their original morphology at elevated temperatures when zinc precursor is added into the reaction mixture.³¹ Herein, to synthesize nearly monodisperse QRs from polydisperse nanowires, we took the advantage of this fact while conducted the experiments under identical synthetic conditions except that DDT was intentionally added into the react solution at elevated temperatures, i.e. 260-280 °C. ZnSe nanowires retain their original morphology because the particle ripening is significantly hindered in the presence of zinc precursor (Figure 4b).³¹ However, they converted into long and thick ZnSe QRs through Ostwald ripening in the absence of both zinc precursor and DDT (Figure 4d),³¹ as further confirmed by absorption spectra (Figure 4e) and XRD (Figure 4f) measurements. The significant difference between the products obtained in the absence of (Figure 4d) and in the presence of DDT (Figure 4c) unambiguously corroborates the essential role of DDT that leads to the initial pairing of nanowires at the early stage and the formation of short alloyed QRs at the later stage of the reaction due to the alkylthiol etching.

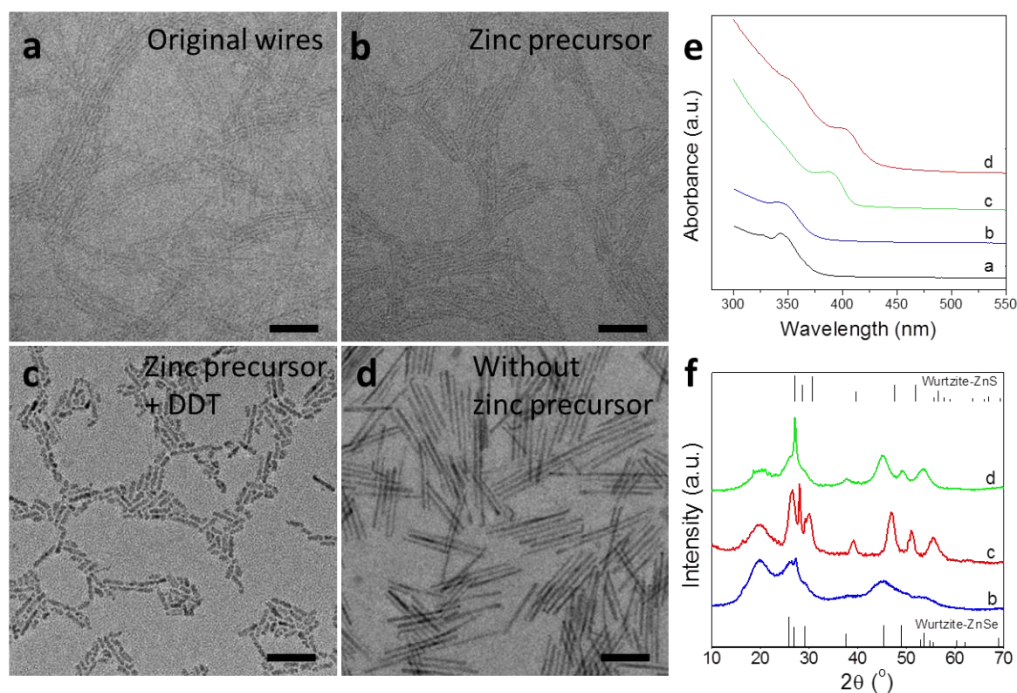


Figure 4. a) TEM image of original ZnSe nanowires. b) TEM image ZnSe nanowires evolved from a) after 30 min at 280 °C in the presence of zinc precursor ($\text{Zn}(\text{NO}_3)_2$) showing ZnSe nanowires retain their morphology. c) TEM image of alloyed $\text{ZnS}_x\text{Se}_{1-x}$ QRs evolved from a) after 30 min at 280 °C in the presence of both zinc precursor ($\text{Zn}(\text{NO}_3)_2$) and DDT showing short alloyed $\text{ZnS}_x\text{Se}_{1-x}$ QRs are obtained due to the etching of DDT. d) TEM image of ZnSe QRs evolved from a) after 30 min at 280 °C in the absence of both zinc precursor ($\text{Zn}(\text{NO}_3)_2$) and DDT showing ZnSe QRs are obtained due to the ripening of ZnSe nanowires at elevated temperatures. All scale bars are 50 nm. e) Absorption spectra of nanoparticles. f) XRD patterns of nanoparticles. The standard XRD patterns for both wurtzite ZnSe and ZnS were given for reference.

We further conducted three groups of parallel syntheses in order to elucidate how the reaction temperature (Figure 5a-c), amount (Figure 5d-f) and type of sulfur source

(Figure 5g-i) will affect the formation of alloyed QRs and how to gain better control on their size distribution. These three parallel syntheses were conducted at or slightly below the temperature of the boiling point of DDT, which is 280 °C.⁵⁵ As soon as DDT was injected into the react solution, oleylamine ligand binding on the surface of nanoparticles is likely replaced by DDT because DDT is a stronger binding ligand than oleylamine. The reaction at 250 °C for 30 minutes in the presence of DDT (Figure 5a) leads to slightly thick nanowires only (length 90 ± 24 nm, width 3.9 ± 0.7 nm, Figure 6a, b), indicating this reaction temperature is too low to ensure the high capability of etching of DDT. Another experiment conducted at 260 °C (Figure 5b) produced a mixture consisting of short QRs and long nanowires with a large size distribution (length 21 ± 13 nm, width 4.0 ± 0.7 nm, Figure 6c, d). The third experiment conducted at 280 °C (Figure 5c) produces nearly monodisperse QRs (length 17 ± 4 nm, width 4.4 ± 0.8 nm, Figure 6e, f). These results clearly demonstrate that nearly monodisperse QRs were obtained from polydisperse nanowires by alkylthiol etching. Moreover, DDT shows a high etching capability only when the temperature of the reaction system is close to its boiling point. This is easy to understand since, at such an elevated temperature, the surface binding ligand of DDT becomes more liable and is easy to be liberated from the surface of the nanoparticles, which in turn, makes the nanoparticles less stable and break down, therefore producing nearly monodisperse short QRs.

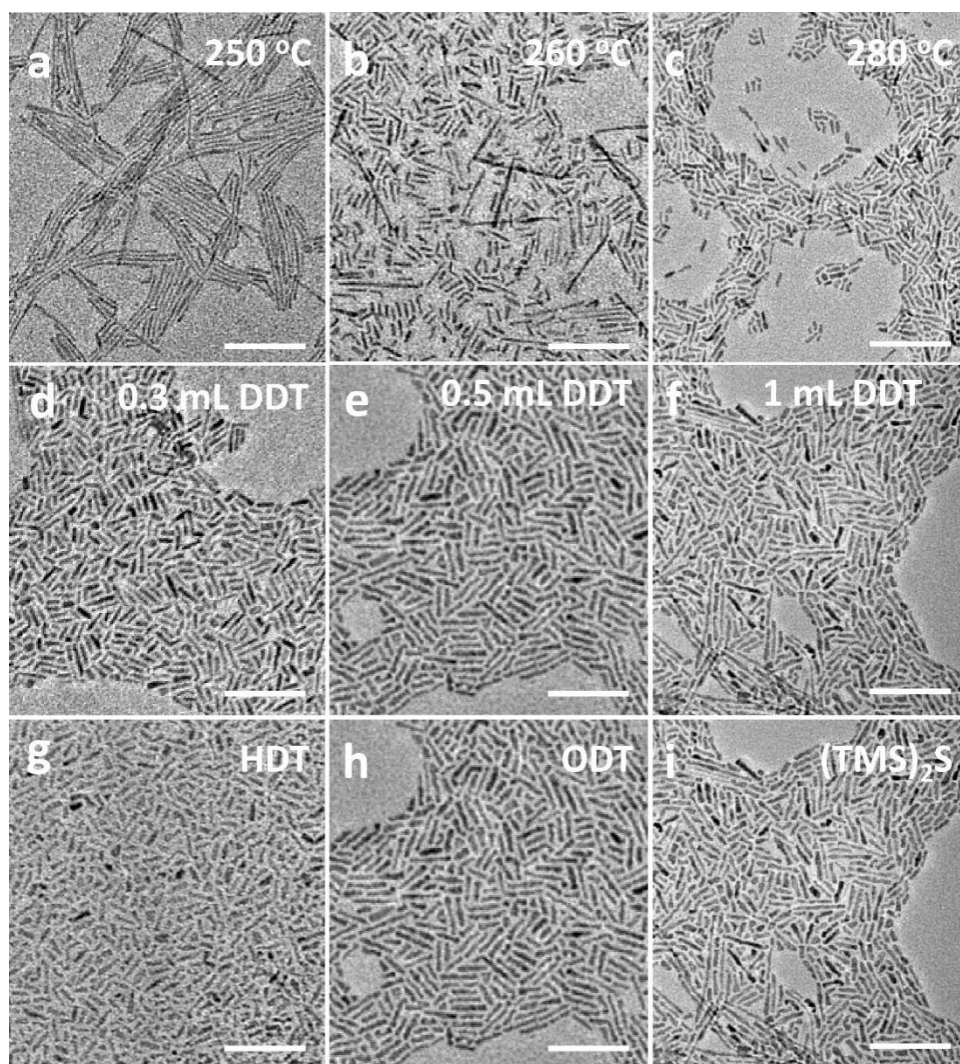


Figure 5. TEM images of ZnSe QRs synthesized under different conditions. a-c) Temperature: a) 30 minutes at 250 °C. b) 30 minutes at 260 °C. c) 30 minutes at 280 °C. d-f) Amount of DDT: d) 0.3 mL. e) 0.5 mL. f) 1 mL. g-i) Sulfur source: g) HDT. h) ODT. i) $(\text{TMS})_2\text{S}$. All scale bars are 50 nm.

We further use other sulfur sources, including 1-hexadecanethiol (HDT), 1-octadecanethiol (ODT), and bis(trimethylsilyl) sulfide $((\text{TMS})_2\text{S})$ (Figure 5g-i.), to conduct the syntheses while keeping all of the other synthetic conditions the same.

All syntheses produces nearly monodisperse QRs, demonstrating the essential role of akylthiol in the formation of monodisperse alloyed QRs from polydisperse nanowires.

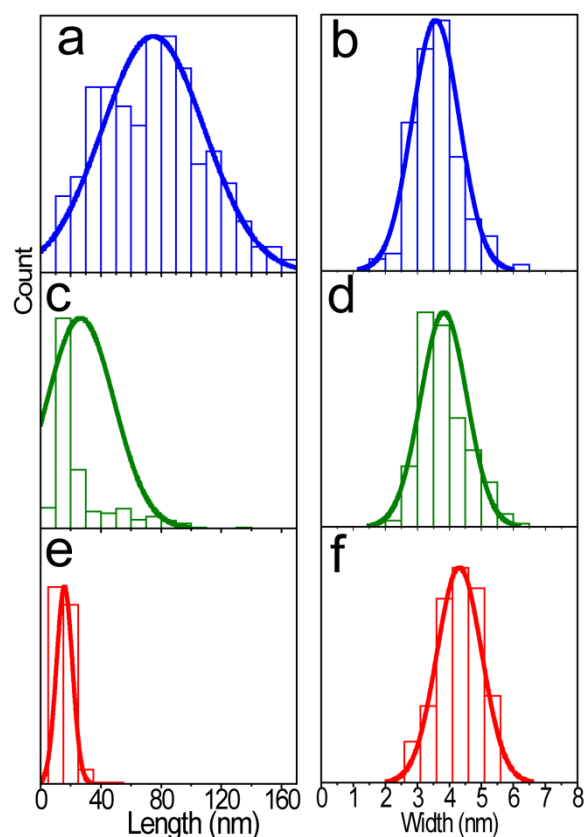


Figure 6. Sizing histograms of nanoparticles formed after 30 minutes at a,b) 250 °C, length is $90\pm24\text{nm}$, width is $3.9\pm0.7\text{ nm}$. c,d) 260 °C, length is $21\pm13\text{nm}$, width is $4.0\pm0.7\text{ nm}$. e,f) 280 °C, length is $17\pm4\text{nm}$, width is $4.4\pm0.8\text{ nm}$.

To gain better control on the size distribution of the QRs, we conducted a second group of three parallel syntheses in the presence of different amounts of DDT. In such syntheses, different amounts of DDT (0.3 mL, 0.5 mL and 1 mL, Figure 5d-f) were swiftly injected into the solution at 260 °C and then the mixture was increased to 280 °C in four minutes. Final products were obtained as the reaction proceeded for 30 minutes at 280 °C. All of the above syntheses produced nearly monodisperse QRs

with different size (See sizing histograms in Figure 7). These results demonstrate that size control of ZnSe QRs can be achieved through the optimization of the amount of DDT.

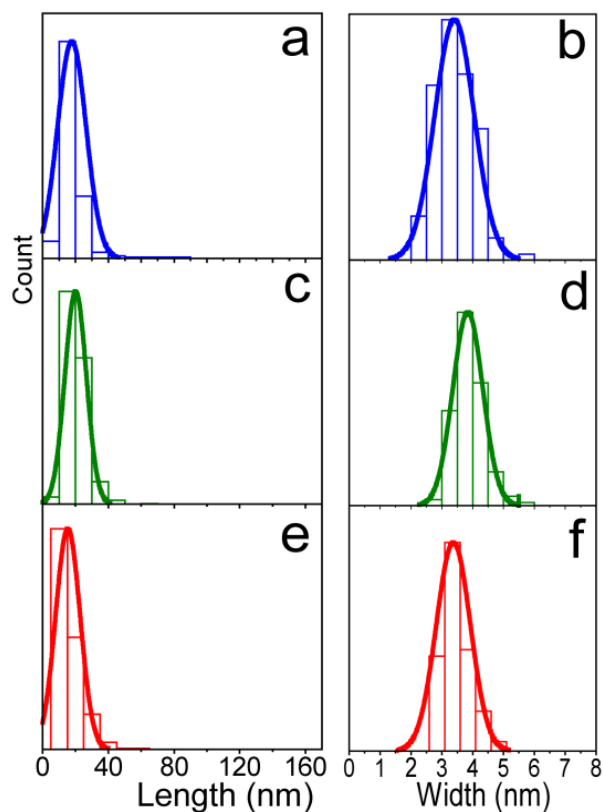


Figure 7. Sizing histograms of $\text{ZnS}_x\text{Se}_{1-x}$ alloyed QRs formed with the addition of a,b) 0.3 mL, c,d) 0.5 mL and e,f) 1 mL DDT. a) length is 18 ± 10 nm, b) width is 3.4 ± 0.6 nm, c) length is 23 ± 5 nm, d) width is 3.9 ± 0.4 nm, e) length is 17 ± 6 nm, f) width 3.5 ± 0.5 nm.

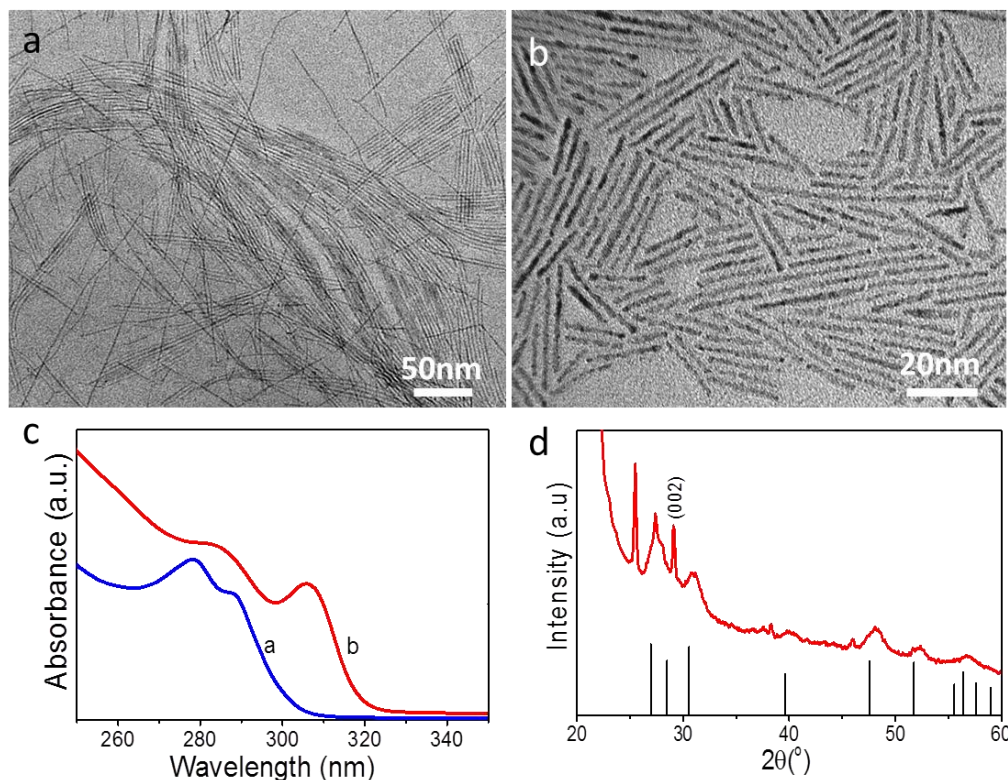


Figure 8. a) TEM images of original ZnS nanowires. b) TEM image of ZnSe nanorods after 30 minutes at 280 °C in the presence of DDT. c) Absorption spectra of ZnS nanowires and ZnS QRs. d) XRD patterns of the obtained ZnS QRs. The XRD pattern of the obtained QRs matches wurtzite ZnS (PDF#36-1450).

To demonstrate the generality of this synthetic approach, it was further expended to synthesize QRs of other zinc chalcogenides, including ZnS, from polydisperse ZnS nanowires. ZnS nanowires with a diameter of ~2 nm (Figure 8a) were synthesized using a literature method³¹ and the absorption spectrum shows the first exciton absorption peak at 288 nm (Figure 8c). After the reaction evolved for 30 minutes at 280 °C, ZnS QRs with a diameter of 3.5 nm were produced (Figure 8b). The red shift of the absorption onset from 288 nm to 304 nm is consistent with the increase of diameter of ZnS QRs (Figure 8c). XRD patterns of the obtained ZnS QRs match

wurtzite structure and the sharp peak of the (002) plane confirmed the preferential elongation of the QRs (Figure 8d).

The obtained alloyed $\text{ZnS}_{2/3}\text{Se}_{1/3}$ QRs were used as the catalysts to test their photocatalytic and PEC performances. Notably, alloyed $\text{ZnS}_{2/3}\text{Se}_{1/3}$ QRs can be directly adopted as photocatalysts for water splitting without further calcination. The photocatalytic water oxidation of the as-prepared samples was conducted under UV-Visible light irradiations using persulfate ($\text{S}_2\text{O}_8^{2-}$) as a sacrifice oxidant for the reduction reaction, whereas tris(2,2'-bipyridine) ruthenium(II) ($\text{Ru}(\text{bpy})_3^{2+}$) was used as the one-electron oxidant photosensitizer to promote multiple-electron water oxidation kinetics and avoid excessive driving potentials. To elucidate the water oxidation mechanism shown schematically in Figure 9a, experiments without one of above three components, i.e. photosensitizer, catalyst and sacrificial agent, were performed, and all experiments show almost no activity (Figure 9b). This suggests that the presence of all three components, $\text{ZnS}_{2/3}\text{Se}_{1/3}$, $[\text{Ru}(\text{bpy})_3]^{2+}$ and $\text{Na}_2\text{S}_2\text{O}_8$, are indispensable for the whole OER. As shown in the scheme of water oxidization (Figure 3a), two out of four $[\text{Ru}(\text{bpy})_3]^{2+}$ are converted into their excited state, $2[\text{Ru}(\text{bpy})_3]^{2+*}$ by illumination through the metal-to-ligand charge transfer (MLCT). Photoinduced electron transfer from $2[\text{Ru}(\text{bpy})_3]^{2+*}$ to $2\text{S}_2\text{O}_8^{2-}$ produces $2[\text{Ru}(\text{bpy})_3]^{3+}$, SO_4^{2-} , and $\text{SO}_4^{\bullet-}$.⁵⁶ The produced $\text{SO}_4^{\bullet-}$ can oxidize $[\text{Ru}(\text{bpy})_3]^{2+}$ to produce two equiv of $2[\text{Ru}(\text{bpy})_3]^{3+}$.⁵⁷ In the meanwhile, electrons and holes are generated and separated by the catalysts of alloyed $\text{ZnS}_{2/3}\text{Se}_{1/3}$ QRs with illumination, and then the photogenerated electrons are transferred to $[\text{Ru}(\text{bpy})_3]^{3+}$ that regenerates $[\text{Ru}(\text{bpy})_3]^{2+}$ while water is oxidized, leading to O_2 evolution.

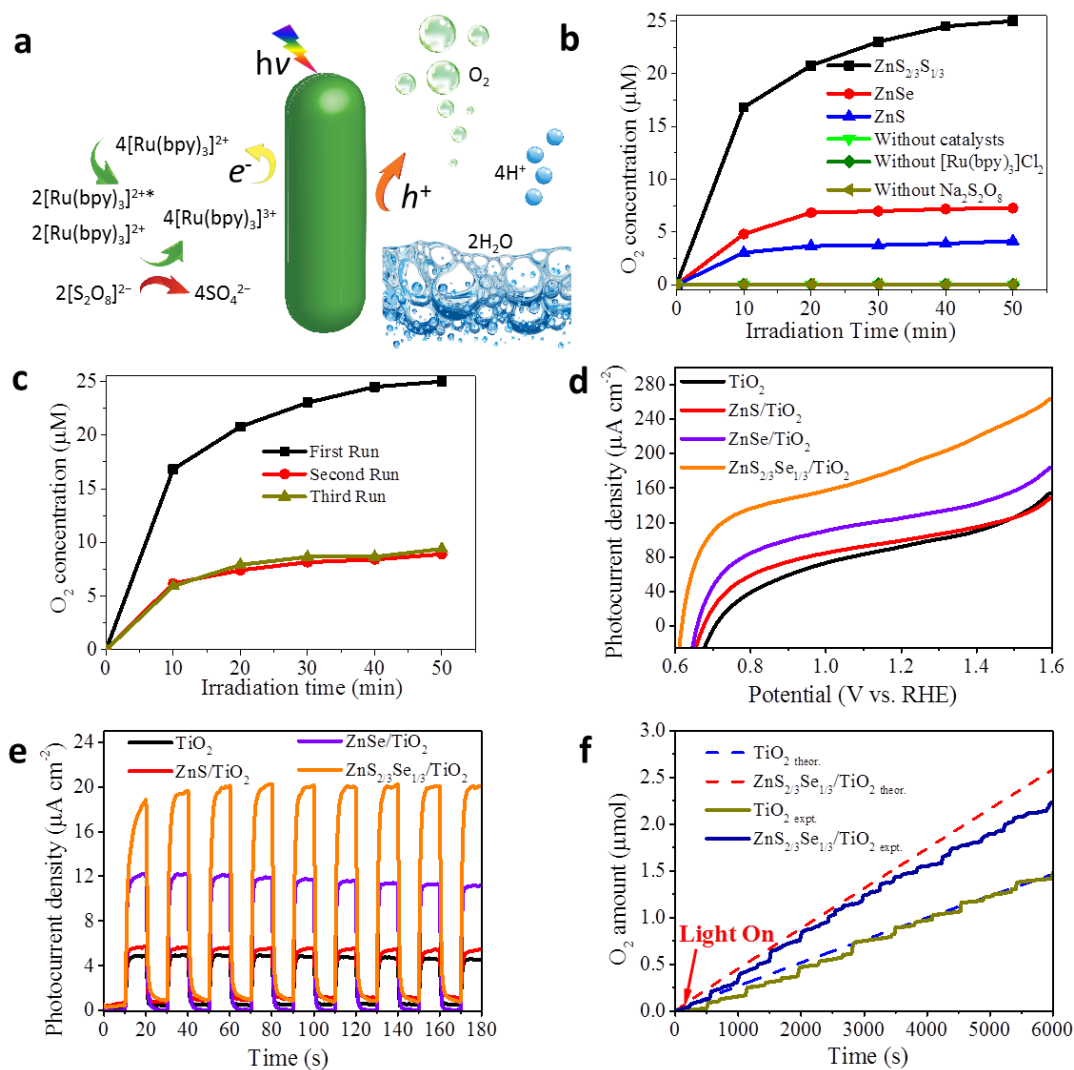


Figure 9. a) Schematic illustration of the water oxidation catalyzed by alloyed $\text{ZnS}_{2/3}\text{Se}_{1/3}$ QRs in the presence of $[\text{Ru}(\text{bpy})_3]^{2+}$ and $\text{Na}_2\text{S}_2\text{O}_8$. b) Comparison of water oxidation using ZnS , ZnSe and alloyed $\text{ZnS}_{2/3}\text{Se}_{1/3}$ QRs as the catalysts. It also shows the control experiment conducted without one of the three components, i.e. $\text{ZnS}_{2/3}\text{Se}_{1/3}$, $[\text{Ru}(\text{bpy})_3]^{2+}$, and $\text{Na}_2\text{S}_2\text{O}_8$. c) Time dependent oxygen concentration using the synthesized catalysts under three cycles running. d) Current-voltage curves of the composites under illumination. e) i-t curves at open circuit potential under light ON-OFF cycling. f) Comparison of the evolved oxygen gases of TiO_2 and

$\text{ZnS}_x\text{Se}_{1-x}/\text{TiO}_2$ (expt.=experimental results; theor.= theoretical amount of O_2 produced, assuming a FE of 100%).

A control experiment utilizing ZnS , ZnSe and alloyed $\text{ZnS}_{2/3}\text{Se}_{1/3}$ QRs as the photocatalysts show that the alloyed QRs demonstrate increased OER activity (Figure 9b). Figure 9c presents the time dependent oxygen concentration using the synthesized catalysts under three cycles running. The catalyst displays an efficient OER yield of $3000 \mu\text{mol g}^{-1} \text{h}^{-1}$ during the first 30 min irradiation and reached the flat at about 1 hour. The apparent quantum efficiency (AQE) under irradiation for $\text{ZnS}_{2/3}\text{Se}_{1/3}$ photocatalysts was measured to be approximately 13.3% ($\lambda = 380 \text{ nm}$) and 0.33% ($\lambda = 420 \text{ nm}$). It is also observed that the reaction rate shows an inevitable slowdown trend at the second running test and stabilized at the third cycle test, which will be further discussed in the following sections.

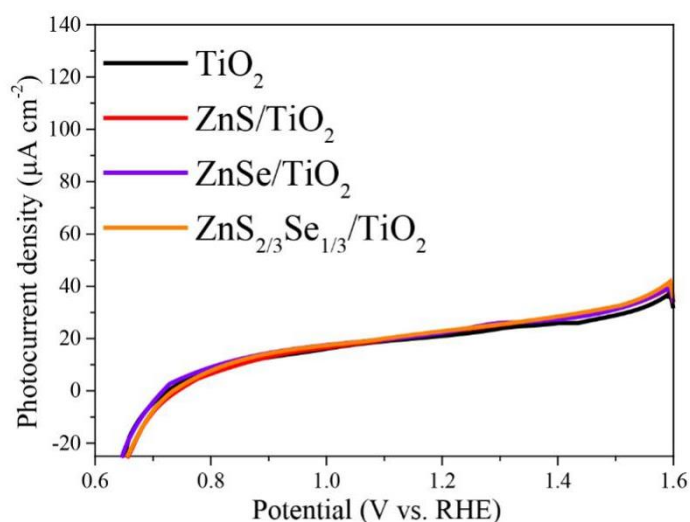


Figure 10. Current-voltage curves of the composites under dark.

QRs-sensitized TiO_2 substrates were prepared and acted as the photoanodes for PEC measurement. Figure 9d and Figure 10 compare the current–voltage curves of the composites under illumination and dark condition, respectively. The suitable band gap alignment between alloyed QRs and TiO_2 ensures the efficient electron hole transport (Figure 11).

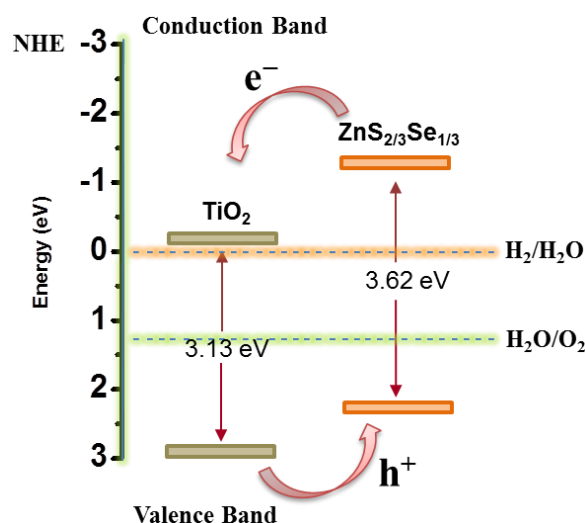


Figure 11. Schematic of alloyed $\text{ZnS}_{2/3}\text{Se}_{1/3}$ QRs sensitized TiO_2 photoanodes for PEC measurement. When TiO_2 and $\text{ZnS}_{2/3}\text{Se}_{1/3}$ (ZnSe or ZnS) are connected together, the energy difference in the conduction band leads to the photo-generated electron flow from the conduction band of $\text{ZnS}_{2/3}\text{Se}_{1/3}$ to the bottom of the conduction band of TiO_2 , and finally to the counter electrode through external circuit. In the meanwhile, the generated holes move from the valence band of TiO_2 to the top of the valence band of $\text{ZnS}_{2/3}\text{Se}_{1/3}$, and then oxidize the water to O_2 on the active sites on $\text{ZnS}_{2/3}\text{Se}_{1/3}$ QRs.

As a result, all the sensitized photoanodes present significantly enhanced anodic photocurrent densities with the order $\text{ZnS}_{2/3}\text{Se}_{1/3}/\text{TiO}_2 > \text{ZnSe}/\text{TiO}_2 > \text{ZnS}/\text{TiO}_2 >$

TiO₂ upon illumination. Furthermore, all the sensitized photoanodes show the cathodal shift onset potentials and the alloyed ZnS_{2/3}Se_{1/3} QRs sensitized photoanode displays the largest shift, demonstrating the highest potential for water oxidation among all QRs-sensitized TiO₂ photoanodes. The detailed oxidation kinetics of these QRs will be further discussed in the DFT section below. As shown in Figure 9e, the transient photo responses of the photoanodes were assessed by measuring i-t curves at an open circuit potential. Prompt and steady photocurrent responses can be captured on the photoanodes during the ON and OFF cycles of illumination. Consistently, ZnS_{2/3}Se_{1/3} QRs sensitized photoanode presents the most obvious enhancement of the photocurrent density, which is 4.5 times higher than that of the pristine TiO₂ anode (Figure 9e). The enhancement of the photocurrent density for ZnSe QRs sensitized photoanode is 2.8 times higher than that of the pristine TiO₂ anode whereas those for ZnS QDs sensitized photoanode does not show evidently enhanced photocurrent density (Figure 9e). The amount of O₂ oxidized by ZnS_{2/3}Se_{1/3}/TiO₂ and TiO₂ photoanodes under the irradiation were in-situ probed through the potentiostatic method. As shown in Figure 9f, the amount of experimentally quantified O₂ of ZnS_{2/3}Se_{1/3}/TiO₂ was nearly 90% Faradic efficiency (FE) of theoretically calculated value. The photocurrent density changes during the FE test were also obtained as a function of illumination time (Figure 12).

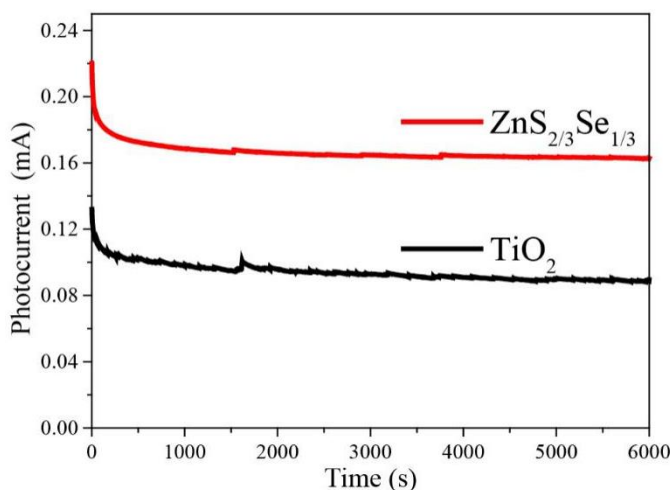


Figure 12. Comparison of photocurrent versus time measurements of alloyed ZnS_{2/3}Se_{1/3} QRs and TiO₂.

We further conducted the electrochemical active surface area (EASA) test to probe the difference of the surface active sites of ZnS, ZnSe and alloyed ZnS_{2/3}Se_{1/3} QRs, wherein double-layer capacitance (Cdl) of the samples were tested from 0.705 to 0.855 V (vs. RHE) at scan rates of 10, 20, 30, 40, and 60 mV s⁻¹ (Figure 13). The corresponding capacitive current densities at 0.75 V were plotted as a function of scan rate (Figure 13d). The slope of the fitted line equals twice the value of Cdl and represents EASA. The alloyed ZnS_{2/3}Se_{1/3} QRs show a higher electrochemically EASA, i.e. 0.288 mF cm⁻², which is about two times higher than that of ZnSe (0.139 mF cm⁻²) and thirty-two times higher than that of ZnS (0.009 mF cm⁻²) QRs. This result clearly shows that abundant surface active sites were introduced to the alloyed ZnS_{2/3}Se_{1/3} QRs by DDT etching during the formation of alloyed QRs.

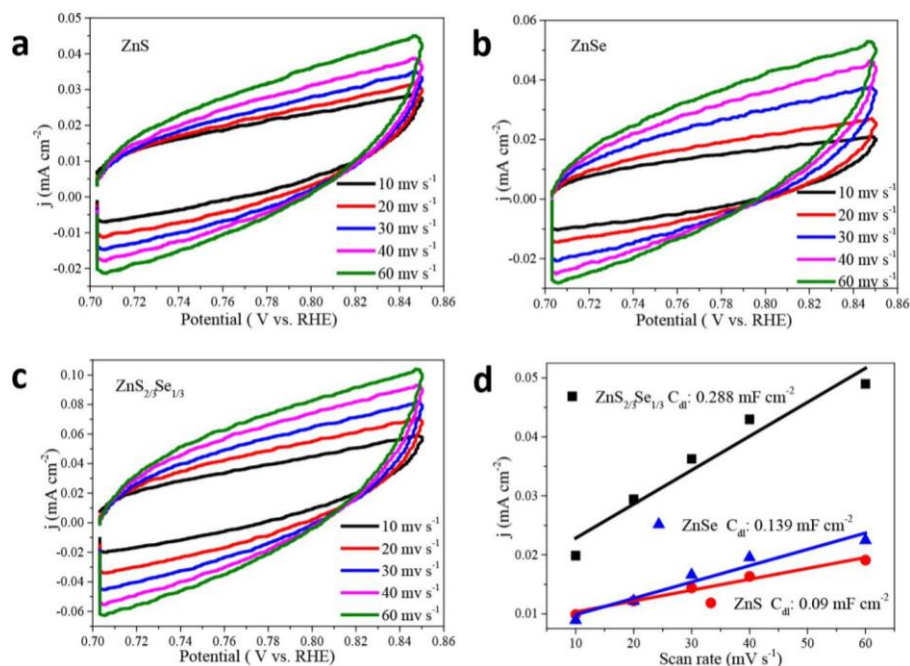


Figure 13. a-c) CV tests of ZnS, ZnSe and alloyed ZnS_{2/3}Se_{1/3} QRs at different scan rates. a) ZnS. b) ZnSe. c) ZnS_{2/3}Se_{1/3}. d) Current density as a function of the scan rate.

A variety of characterizations on the alloyed ZnS_{2/3}Se_{1/3} QRs after photocatalytic and PEC tests were conducted to gain insights on the deceased photocatalytic activity after two times of running as well as to elucidate their stability. Figure 14a-c and d-f compared the electron microscopy images of alloyed ZnS_{2/3}Se_{1/3} QRs after photocatalytic and PEC tests, respectively. The HAADF-STEM (Figure 14a, d), TEM (Figure 14b, 4e), HRTEM and associated FFT analysis of the selected area (Figure 14c, f, Figure 15), and XRD (Figure 16) measurements show that the ZnS_{2/3}Se_{1/3} QRs after the OER and PEC tests retain their original morphology and show good crystallinity, with evident lattice fringes indexed into wurtzite structure (Figure 14c, f, Figure 15). STEM-EDX analysis show that all elements including zinc, selenium and sulfur in the ZnS_{2/3}Se_{1/3} QRs after OER (Figures 17) and PEC

(Figures 18) tests are distributed evenly throughout the whole nanoparticles, further confirming their good stability.

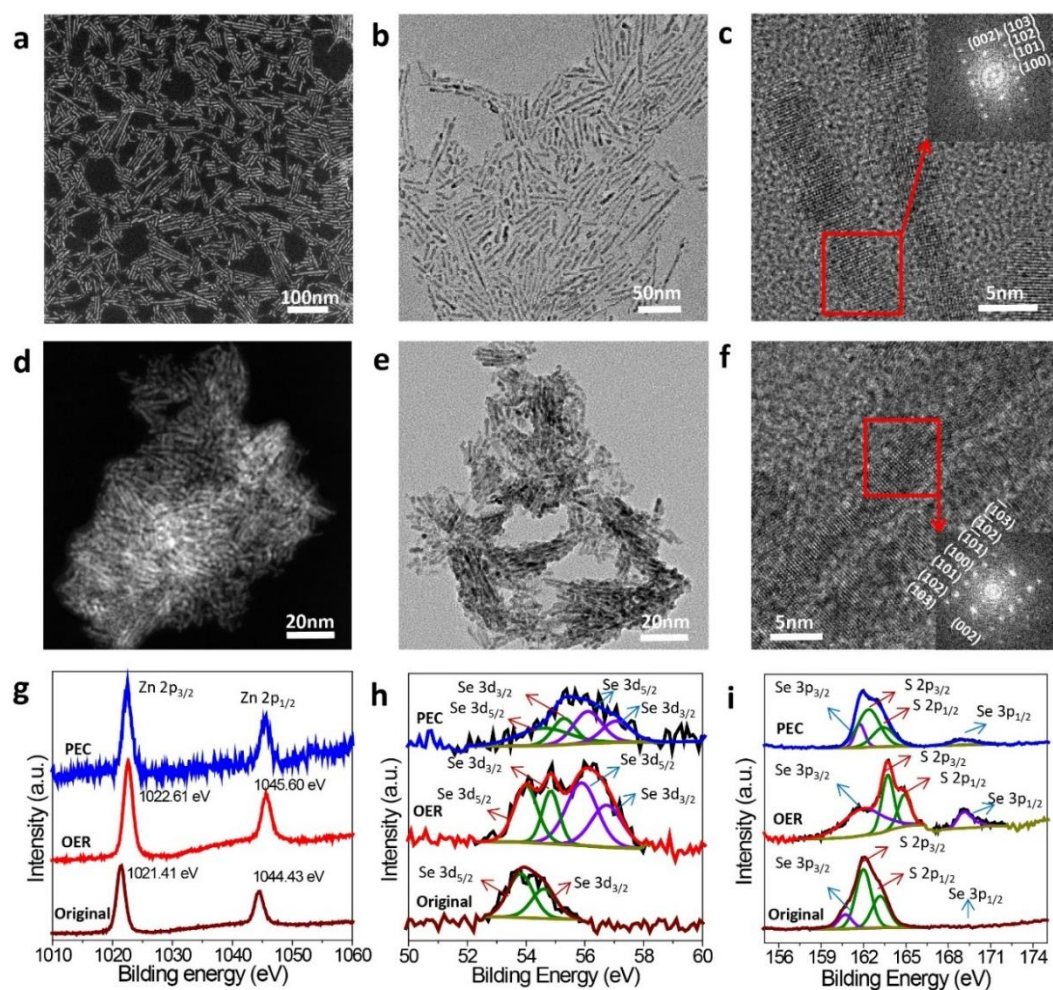


Figure 14. a-c) Electron microscopy images of the alloyed $\text{ZnS}_{2/3}\text{Se}_{1/3}$ QRs after the OER test. a) HAADF-STEM. b) TEM. c) HRTEM. d-f) Electron microscopy images of the alloyed $\text{ZnS}_{2/3}\text{Se}_{1/3}$ QRs after the PEC test. d) HAADF-STEM. e) TEM. f) HRTEM. Insets in c,f) show FFT of selected areas of alloyed $\text{ZnS}_{2/3}\text{Se}_{1/3}$ QRs, revealing the crystallographic relations. g-i) Comparison of XPS spectra of the alloyed $\text{ZnS}_{2/3}\text{Se}_{1/3}$ QRs before and after the OER and PEC tests. g) Zn 2p, h) Se 3d, i) Se 3p and S 2p.

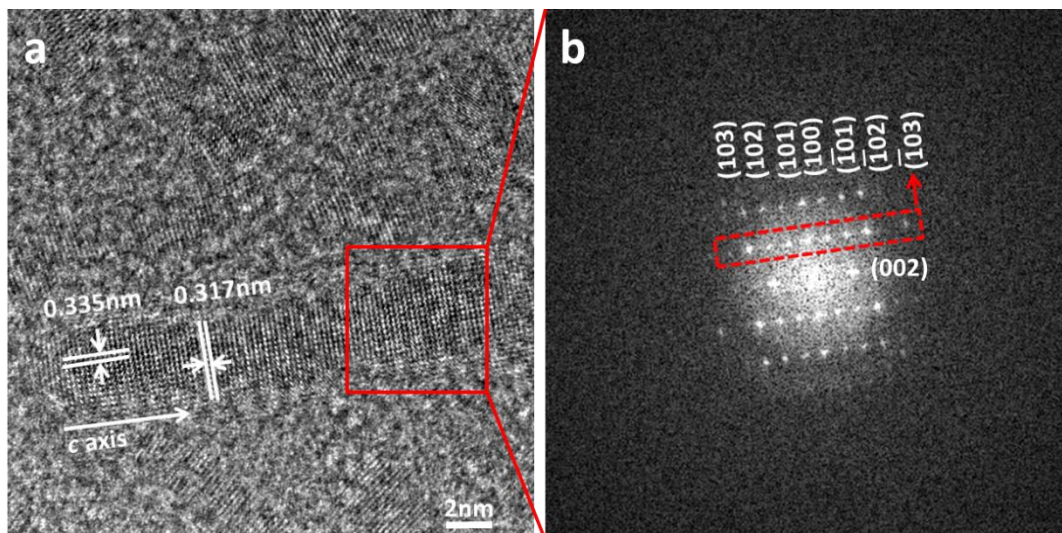


Figure 15. a) HRTEM image of the alloyed $\text{ZnS}_{2/3}\text{Se}_{1/3}$ QRs after the OER test. White lines indicate the orientation of selected crystal planes and arrow shows the orientation of the long axis of the alloyed QRs. b) FFT of selected areas in a) marked by a red rectangle, revealing the crystallographic relations.

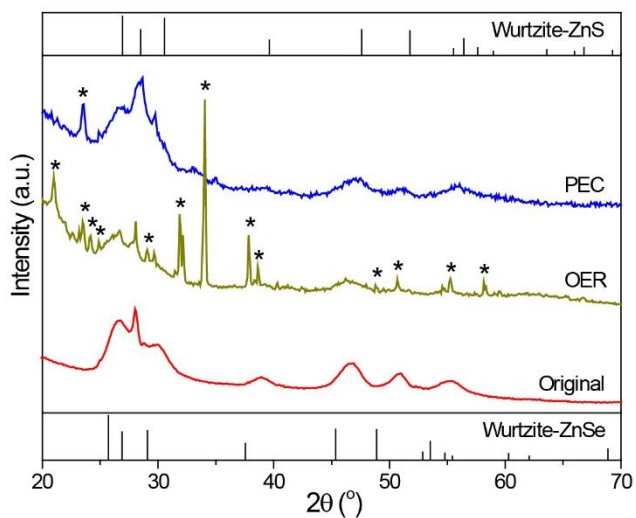


Figure 16. Comparison of XRD patterns of the alloyed $\text{ZnS}_{2/3}\text{Se}_{1/3}$ QRs before and after the OER and PEC tests. The sharp diffraction peaks marked by * are associated

with the residuals of the reagents for the photocatalytic test. The standard XRD patterns for both wurtzite ZnSe and ZnS were given for reference.

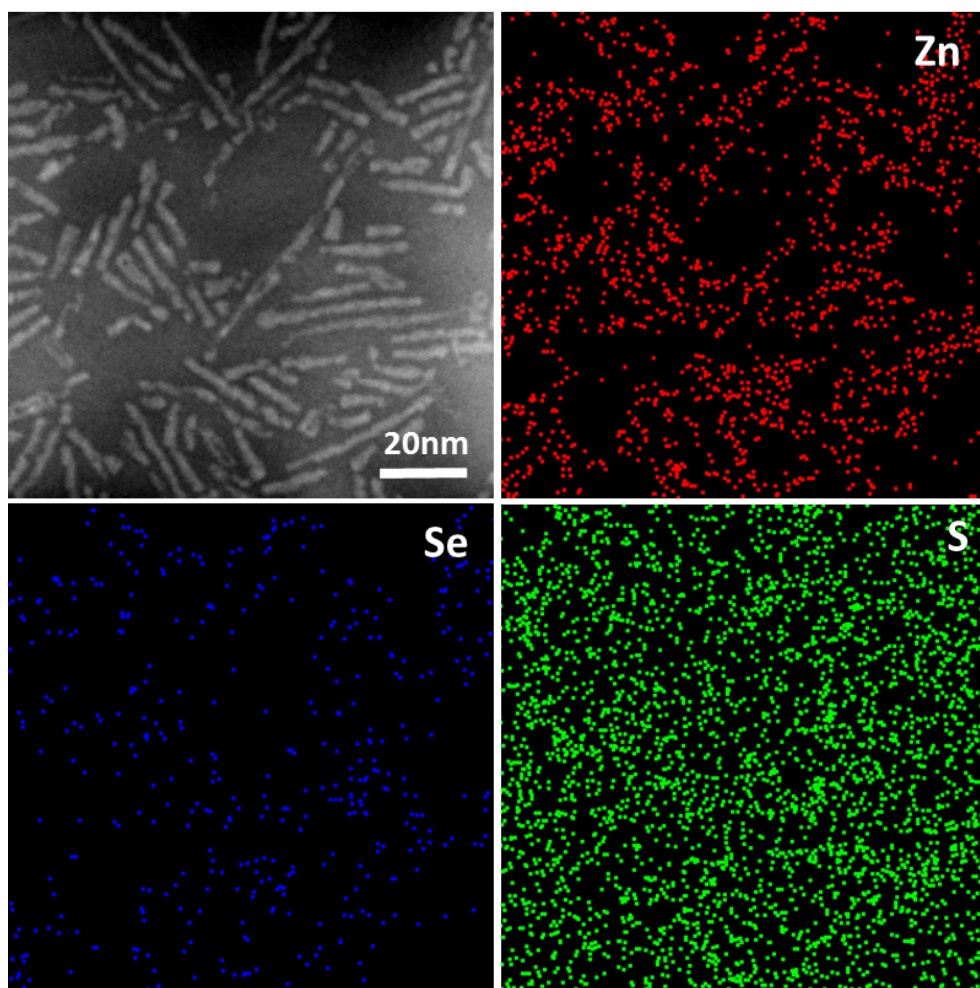


Figure 17. HAADF-STEM image and STEM-EDX element maps of the $\text{ZnS}_{2/3}\text{Se}_{1/3}$ QRs after the OER test.

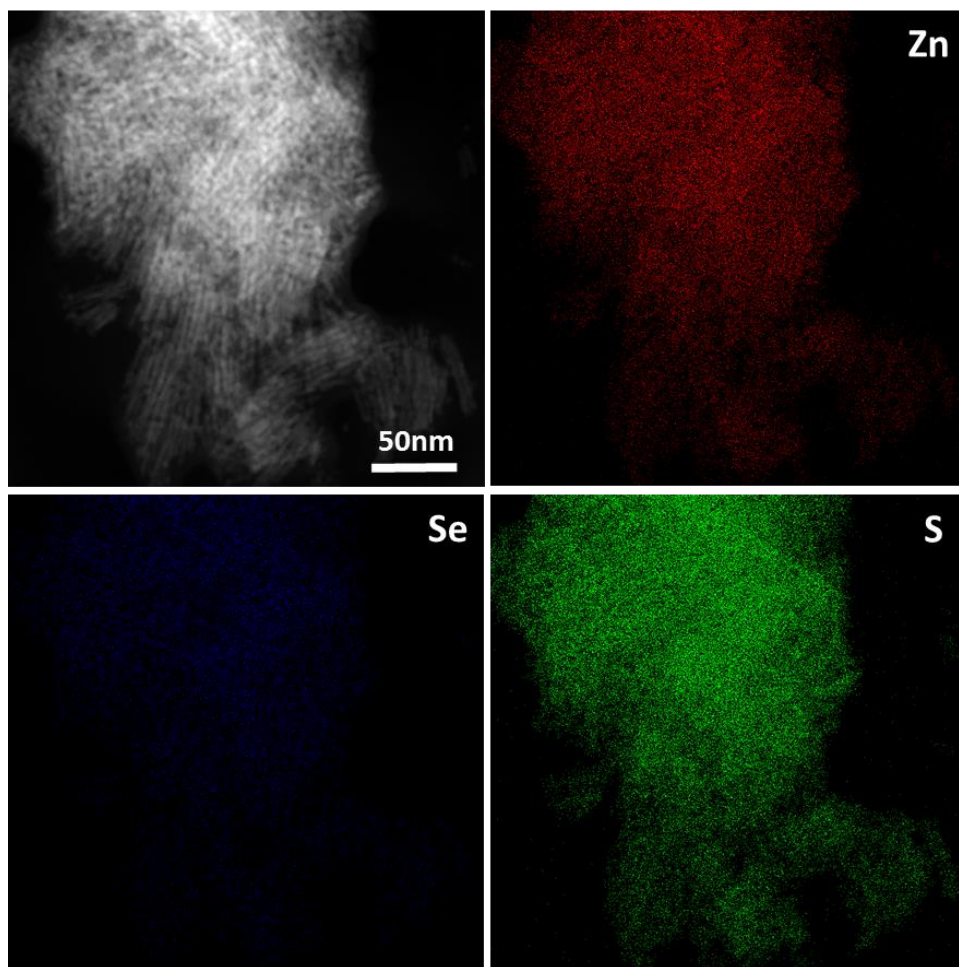


Figure 18. HAADF-STEM image and STEM-EDX element maps of the $\text{ZnS}_{2/3}\text{Se}_{1/3}$ QRs after the PEC test.

High-resolution X-ray photoelectron spectroscopy (XPS) was used to examine the binding environment in QRs. Notably, the survey spectra of the samples after OER and PEC tests reveal that the binding energies for Zn 2p (Figure 14g), Se 3d (Figure 14h), Se 3p and S2p (Figure 14i) show a slight shift to the higher energy in comparison with those of the original QRs. This tiny shift of the binding energy is likely attributed to the interaction between Se (Zn, S) and other atoms, as previously observed in Au/ZnSe.⁵⁸ Except for Se, all elements are present solely as Zn(+2) and

S(-2), since no satellites of these elements with other oxidation states were observed.⁵⁹⁻⁶⁰ However, a close inspection on the 3d region of Se of the QRs after OER and PEC tests (Figure 14h) shows that the spectra in this region can be well-fitted by two doublets of selenium species with an integrated intensity ratio and energy difference for Se 3d_{5/2} and Se 3d_{3/2} being 3:2 and 0.83 eV, respectively, which are in good agreement with the literature values.⁶¹ The Se 3d_{5/2} binding energy at 56.9 eV (blue fitted curves in Figure 14h) for the new selenium species matches well with that of Na₂Se(S₂O₃)₂,⁶² which may form on the surface of ZnS_{2/3}Se_{1/3} QRs during the OER and PEC tests. The determination of XPS spectra of selenium in the 3p region is complicated due to the overlap with S peaks in 2p region (Figure 14i). However, the positions of the main components of S 2p_{3/2} (162.03 eV) and S 2p_{1/2} (163.15 eV) confirm the presence of sulfides S²⁻.⁶³ The interpretation of the XPS spectra is consistent with our observation on the decreased activity of the catalysts after two circles running. This is because that the surface active sites of alloyed ZnS_{2/3}Se_{1/3} QRs has been stabilized after the first run, during which Na₂Se(S₂O₃)₂ may form on the surface of ZnS_{2/3}Se_{1/3} QRs and thus partially blocks the surface active sites.

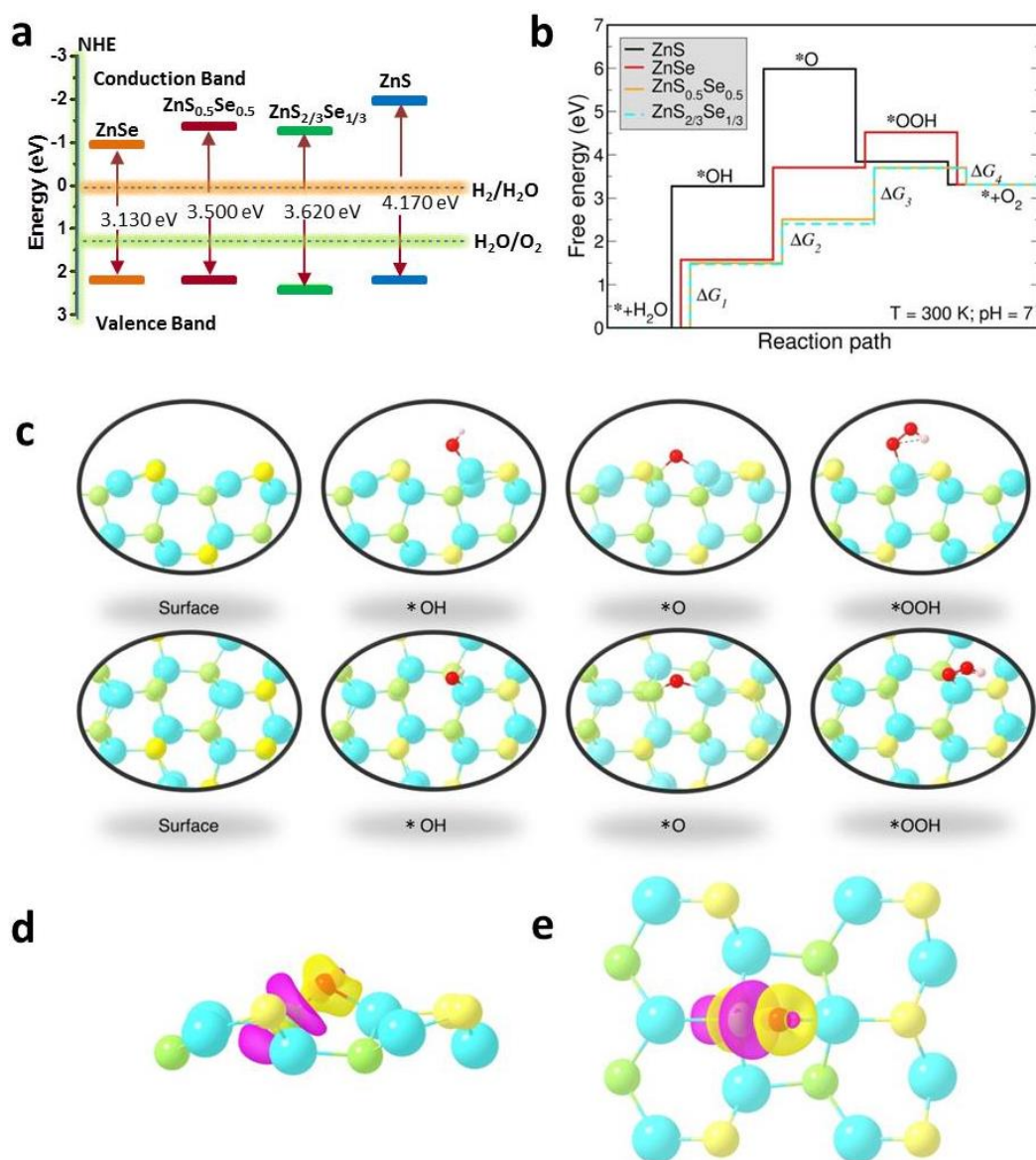


Figure 19. a) Schematic of the band gap alignment of ZnS, ZnSe and alloyed $\text{ZnS}_x\text{Se}_{1-x}$ ($x=0.5, 2/3$) and the relative band gap energies with respect to the normal hydrogen electrode level (NHE). b) Diagram of the 4-step Gibbs free energy changes calculated on (100) surface. c) Configurations of adsorbed redox species on $\text{ZnS}_{0.5}\text{Se}_{0.5}$ (100) surface associated with b). Top panel: side view; Bottom panel: top view. Colour scheme: cyan (Zn), yellow (S), green (Se), red (O), pink (H). d,e) Plot of differential charge density (magenta: charge depletion, yellow: charge accumulation)

at an isosurface value of $0.004 \text{ e}/\text{\AA}^3$ for *O species absorbed on $\text{ZnS}_{0.5}\text{Se}_{0.5}$ (100) surface. d) Side view. e) Top view.

To gain further insights on the photocatalytic and PEC activities of alloyed $\text{ZnS}_x\text{Se}_{1-x}$ QRs, in particular to elucidate the reason why alloyed QRs show increased catalytic activities over their counterparts such as both pure ZnS and ZnSe QRs, we employed the first-principles method to evaluate the catalytic activity of alloyed $\text{ZnS}_x\text{Se}_{1-x}$ QRs.⁶⁴⁻⁶⁵ We used two different stoichiometric ratios of the alloyed QRs, i.e. $\text{ZnS}_{0.5}\text{Se}_{0.5}$ as the intermediate, and $\text{ZnS}_{2/3}\text{Se}_{1/3}$ as the final product, to perform the simulations. Results shows that this ratio only changes the amount of the surface active sites of the alloyed QRs but does not alter their intrinsic properties for catalysis. As compared in Figure 19a, Figures 20, 21 and Table 2 in Supporting Information, the band gap of QRs is gradually shifting to a higher energy as the composition of sulfur increases, but clearly their valance band edges are lower than the $\text{H}_2\text{O}/\text{O}_2$ level and their conduction band edges are higher than the $\text{H}_2/\text{H}_2\text{O}$ level, suggesting their potential capability for OER. The (100) surface ($0.026 \text{ eV}/\text{\AA}^2$ for ZnS) is calculated to be more stable than the (110) ($0.044 \text{ eV}/\text{\AA}^2$ for ZnS) surface. This is consistent with the aforementioned structural characterizations, in which the (100) surface is the dominant surface for wurtzite QRs, and therefore the OER Gibbs free energy calculations were based on this surface.

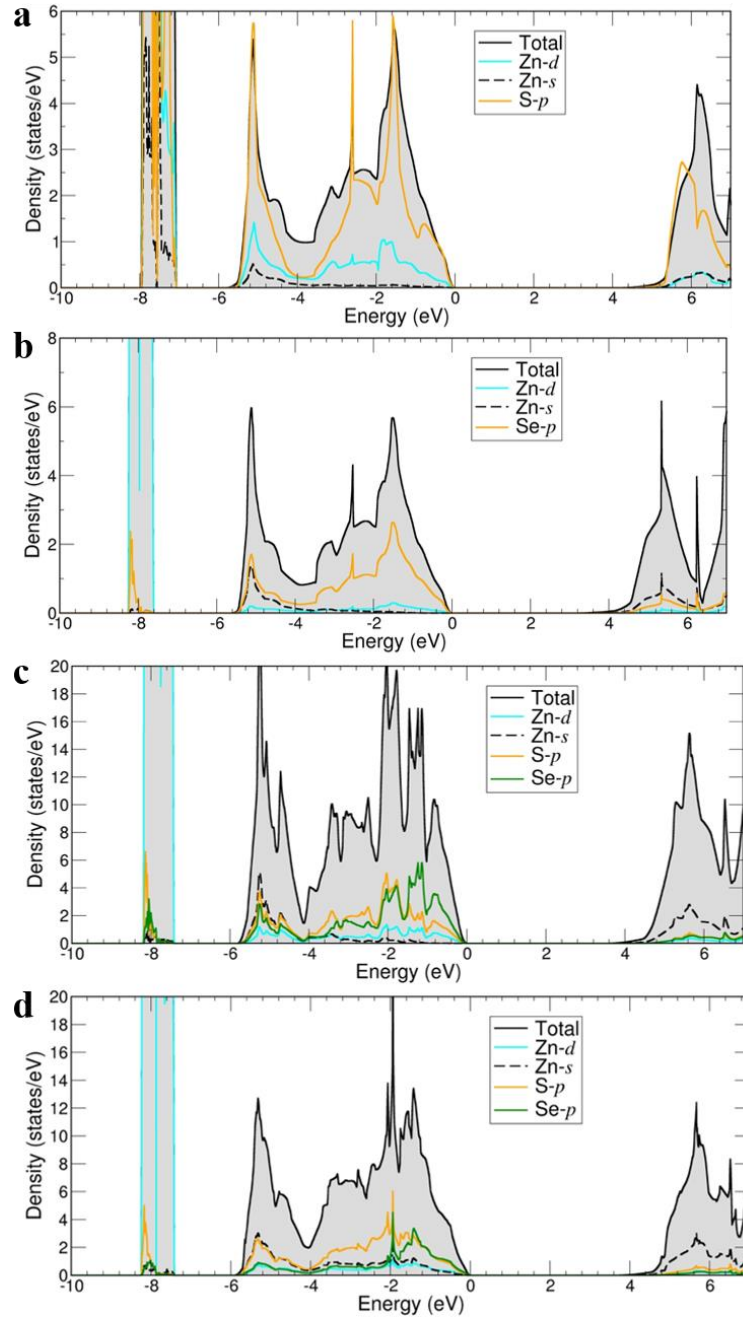


Figure 20. a-d) Calculated electronic density of states using PBE0 functional. a) ZnS. b) ZnSe. c) $\text{ZnS}_{0.5}\text{Se}_{0.5}$. d) $\text{ZnS}_{2/3}\text{Se}_{1/3}$. Energy is referenced to VBM. For ZnS, Zn-4s electrons are merged with Zn-3d electrons, indicating the significant *s-d* hybridization, which is due to the bonding with S. S-*p* strongly hybridizes with Zn-*s* and *p* states, suggesting a strong covalency and large band gap. *s-d* hybridization is very weak in ZnSe. This is due to a weak Zn-Se bonding compared to Zn-S. So,

ZnSe also has a smaller band gap. In $\text{ZnS}_{0.5}\text{Se}_{0.5}$, the occupied states close to Fermi level are dominated by Se- p , indicating that the Zn-Se bonding remains weaker than Zn-S.

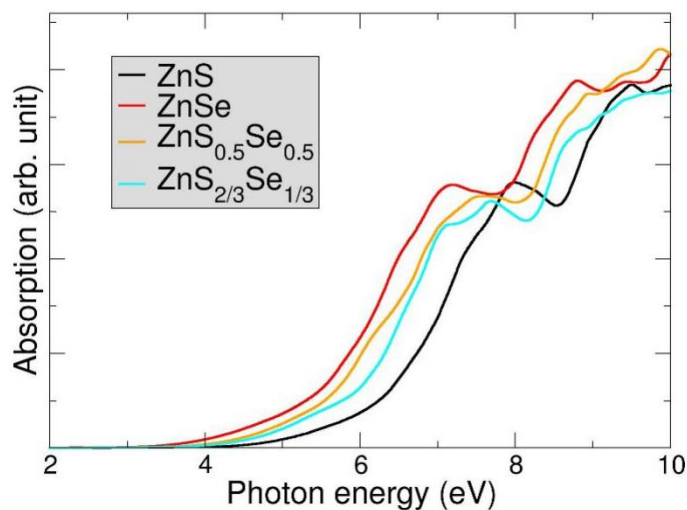


Figure 21. Light absorption spectra for ZnS, ZnSe, $\text{ZnS}_{0.5}\text{Se}_{0.5}$ and $\text{ZnS}_{2/3}\text{Se}_{1/3}$ calculated using PBE0 functional.

Table 2. Calculated lattice parameters by using GGA+U and calculated band gap and band edge positions by using PBE0.

Material	Lattice parameter		Band gap (eV)	VBM (V)	CBM (V)
	(Å)				
	<hr/>				
	a	c			
ZnS	3.799	6.224	4.170	2.163	-2.007
ZnSe	4.008	6.574	3.130	2.164	-0.966

ZnS _{0.5} Se _{0.5}	3.905	6.399	3.500	2.134	-1.366
ZnS _{2/3} Se _{1/3}	3.869	6.341	3.620	2.327	-1.293

OER involving four electron transfer can be treated by four elementary steps, during which intermediates of *OH, *O and *OOH are generated (Figure 19b, c). The OER energy barriers associated with Gibbs free energy changes during the four steps (ΔG_1 - ΔG_4) for generation of *OH, *O, *OOH and O₂ species on active Zn sites of (100) surface, as schematically illustrated in Figure 19b, were shown in Table 3, Supporting Information. The configurations of adsorbed redox species on (100) surface were depicted in Figure 19c. The high uphill/endothermic energy profiles for the deprotonation of H₂O (*+H₂O→ *OH+H⁺+e⁻, step 1) and *OH (HO*→O*+H⁺+e⁻, step 2) on ZnS (100) indicate a high overpotential and the low activity of ZnS. ΔG_1 of ZnSe is much lower than ZnS, suggesting a higher activity of ZnSe. However, ΔG_2 of ZnSe is still large. Based on the electronic structure of ZnS_xSe_{1-x} alloys, we would expect an intermediate OER activity for ZnS_xSe_{1-x} alloys. However, very highly active Zn sites were found on ZnS_{0.5}Se_{0.5} (100) and ZnS_{2/3}Se_{1/3} (100) surfaces. ΔG_1 , ΔG_2 and ΔG_3 of the alloys are much lower than those of ZnS and ZnSe, which leads to a very low overpotential. Besides, step 4 (*OOH → O₂+H⁺+e⁻) is downhill/exothermic for all materials, suggesting that it is effortless to proceed and *OOH will convert to O₂ automatically. Therefore, ZnS_xSe_{1-x} alloys have abnormally highly active surface sites compared to both ZnS and ZnSe.

Table 3. Calculated oxygen evolution reaction free energies for pH=7. The energies for pH=0 are shown in the brackets.

Material	Reaction free energy (eV)			
	ΔG_1	ΔG_2	ΔG_3	ΔG_4
ZnS	3.27 (3.68)	2.71 (3.11)	-2.14 (-1.74)	-0.53 (-0.13)
ZnSe	1.57 (1.98)	2.13 (2.54)	0.81 (1.22)	-1.21 (-0.81)
ZnS _{0.5} Se _{0.5}	1.50 (1.90)	1.01 (1.41)	1.19 (1.60)	-0.39 (0.01)
ZnS _{2/3} Se _{1/3}	1.47 (1.87)	0.93 (1.34)	1.29 (1.69)	-0.38 (0.02)

We find the high activity of ZnS_xSe_{1-x} alloys is correlated with their local surface structure. A close inspection reveals the key role of Se ions in promoting the OER activity of Zn surface site that is coordinated by two Se ions and one S ion (Figure 19c, e and f). The Se at the second nearest neighbour distance to Zn can form Se-O bonding with the adsorbed *O on Zn (and there is no barrier as can be seen from nudged elastic band calculations). The differential charge density for *O species absorbed on ZnS_xSe_{1-x} (100) surface shows that *O can gain additional charge by forming a chemical bond with the neighbouring Se, which stabilizes *O on the surface and reduces the energy barrier ΔG_2 ($\text{HO}^* \rightarrow \text{O}^* + \text{H}^+ + \text{e}^-$). The formation of Se-O bonding can be understood since Se-*p* electrons that dominate the occupied states (Figure 17) close to Fermi level is chemically active. While, this cannot occur for surface Zn site coordinated completely with three Se ions, for which the Zn ion

forms a strong Zn-O bonding. Therefore, the alloyed $\text{ZnS}_x\text{Se}_{1-x}$ QRs with more active Zn site show a higher OER activity than pure ZnS and ZnSe.

3.5 Conclusion

In conclusion, we have developed a wet-chemical approach that leads to spontaneous formation of nearly monodisperse alloyed $\text{ZnS}_x\text{Se}_{1-x}$ QRs from polydisperse ZnSe nanowires by the etching of alkylthiol. The obtained alloyed QRs can be directly used for OER and PEC tests without calcination. Compared with pure ZnS and ZnSe, alloyed $\text{ZnS}_x\text{Se}_{1-x}$ QRs show enhanced OER activity in water splitting and PEC activities because of the highly active Zn sites on the (100) surface and reduced water oxidation energy barrier, as revealed by DFT simulations. This work not only sheds light on the construction of one-dimensional nanostructures with monodispersity but also provides a basis for earth abundant and eco-friendly photocatalysts.

3.6 References

- [1] R. D. L. Smith, M. S. Prévot, R. D. Fagan, Z. P. Zhang, P. A. Sedach, M. K. J. Siu, M. Kit, J. Siu, S. Trudel, C. P. Berlinguette, *Science* **2013**, 340, 60.
- [2] J. Wang, F. Xu, H. Y. Jin, Y. Q. Chen, Y. Wang, *Adv. Mater.* **2017**, 29, 1605838.
- [3] X. F. Lu, L. F. Gu, J. W. Wang, J. X. Wu, P. Q. Liao, G. R. Li, *Adv. Mater.* **2017**, 29, 1604437.

- [4] R. Liu, Y. Wang, D. Liu, Y. Zou, S. Wang, *Adv. Mater.* **2017**, 29, 1701546.
- [5] T. R. Cook, D. K. Dogutan, S. Y. Reece, Y. Surendranath, T. S. Teets, D. G. Nocera, *Chem. Rev.* **2010**, 110, 6474.
- [6] Y. P. Liu, Q. J. Li, R. Si, G. D. Li, W. Li, D. P. Liu, D. J. Wang, L. Sun, Y. Zhang, X. X. Zou, *Adv. Mater.* **2017**, 29, 1606200.
- [7] L. H. Zhuang, L. Ge, Y. S. Yang, M. R. Li, Y. Jia, X. D. Yao, Z. H. Zhu, *Adv. Mater.* **2017**, 29, 1606793.
- [8] Y. Zheng, Y. Jiao, Y. Zhu, Q. Cai, L. H. Li, Y. Han, Y. Chen, S. Qiao, *J. Am. Chem. Soc.* **2017**, 139, 3336.
- [9] F. Song, X. Hu, *Nat. Commun.* **2014**, 5, 4477.
- [10] X. Lu, C. Zhao, *Nat. Commun.* **2015**, 6, 6616.
- [11] J. Wang, W. Cui, Q. Liu, Z. Xing, A. Asiri, X. Sun, *Adv. Mater.* **2016**, 28, 215.
- [12] C. Tang, N. Cheng, Z. Pu, W. Xing, X. Sun, *Angew. Chem., Int. Ed.* **2015**, 127, 9483.
- [13] H. Zhu, J. Zhang, R. Yanzhang, M. Du, Q. Wang, G. Gao, J. Wu, G. Wu, M. Zhang, B. Liu, *Adv. Mater.* **2015**, 27, 4752.
- [14] N. Jiang, B. You, M. Sheng, Y. Sun, *Angew. Chem., Int. Ed.* **2015**, 127, 6349.
- [15] R. Wang, X. Y. Dong, J. Du, J. Y. Zhao, S. Q. Zang, *Adv. Mater.* **2018**, 30, 1703711.
- [16] L. Amirav, A. P. Alivisatos, *J. Phys. Chem. Lett.* **2010**, 1, 1051.
- [17] G. Dukovic, M. G. Merkle, J. H. Nelson, S. M. Hughes, A. P. Alivisatos, *Adv. Mater.* **2008**, 20, 4311.

- [18] S. E. Habas, P. Yang, T. Mokari, *J. Am. Chem. Soc.* **2008**, *130*, 3294.
- [19] E. Elmalem, A. E. Suanders, R. Costi, A. Salant, U. Banin, *Adv. Mater.* **2008**, *20*, 4312.
- [20] H. Schlicke, D. Ghosh, L. Fong, H. L. Xin, H. Zheng, A. P. Alivisatos, *Angew. Chem., Int. Ed.* **2013**, *52*, 980.
- [21] L. J. Hill, M. M. Bull, Y. Sung, A. G. Simmonds, P. T. Dirlam, N. E. Richey, S. E. DeRosa, I.-B. Shim, D. Guin, P. J. Costanzo, N. Pinna, M.-G. Willinger, W. Vogel, K. Char, J. Pyun, *ACS Nano* **2012**, *6*, 8632.
- [22] M. Berr, A. Vaneski, A. S. Susha, J. Rodríguez-fernández, M. Döblinger, F. Jäckel, A. L. Rogach, J. Feldmann, *Appl. Phys. Lett.* **2010**, *97*, 093108.
- [23] Y. Shemesh, J. E. Macdonald, G. Menagen, U. Banin, *Angew. Chem., Int. Ed.* **2011**, *123*, 1217.
- [24] Y. Ben-Shahar, F. Scotognella, I. Kriegel, L. Moretti, G. Cerullo, E. Rabani, U. Banin, *Nat. Commun.* **2016**, *7*, 10413.
- [25] Y. Ben-Shahar, F. Scotognella, N. Waiskopf, I. Kriegel, S. D. Conte, G. Cerullo, U. Banin, *Small* **2015**, *11*, 462.
- [26] X. Peng, L. Manna, W. Yang, J. Wickham, E. Scher, A. Kadavanich, A. P. Alivisatos, *Nature* **2000**, *404*, 59.
- [27] D. J. Milliron, S. M. Hughes, Y. Cui, L. Manna, J. Li, L.-W. Wang, A. P. Alivisatos, *Nature* **2004**, *430*, 190.
- [28] L. Carbone, C. Nobile, M. De. Giorgi, F. D. Sala, G. Morello, P. Pompa, M. Hytch, E. Snoeck, A. Fiore, I. R. Franchini, M. Nadasan, A. F. Silvestre, L.

- Chiodo, S. Kudera, R. Cingolani, R. Krahne, L. Manna, *Nano Lett.* **2007**, *7*, 2942.
- [29] D. V. Talapin, J. H. Nelson, E. V. Shevchenko, S. Aloni, B. Sadtler, A. P. Alivisatos, *Nano Lett.* **2007**, *7*, 2951.
- [30] J. Zhang, C. Rowland, Y. Liu, H. Xiong, S. Kwon, E. Shevchenko, R. D. Schaller, V. B. Prakapenka, S. Tkachev, T. Rajh, *J. Am. Chem. Soc.* **2015**, *137*, 742.
- [31] G. Jia, U. Banin, *J. Am. Chem. Soc.* **2014**, *136*, 11121.
- [32] S. Acharya, S. Efrima, *J. Am. Chem. Soc.* **2005**, *127*, 3486.
- [33] A. B. Panda, S. Acharya, S. Efrima, *Adv. Mater.* **2005**, *17*, 2471.
- [34] Y. Wang, Y. Zhou, Y. Zhang, W. E. Buhro, *Inorg. Chem.* **2015**, *54*, 1165.
- [35] J. Zhang, S. Jin, H. C. Fry, S. Peng, E. Shevchenko, G. P. Wiederrecht, T. Rajh, *J. Am. Chem. Soc.* **2011**, *133*, 15324.
- [36] S. Acharya, S. Sarkar, N. Pradhan, *J. Phys. Chem. C* **2013**, *117*, 6006.
- [37] T. Yao, Q. Zhao, Z. Qiao, F. Peng, H. Wang, H. Yu, C. Chi, J. Yang, *Chem. Eur. J.* **2011**, *17*, 8663.
- [38] B. Ji, Y. E. Pan, U. Banin, *ACS Nano* **2017**, *11*, 7312.
- [39] G. Jia, A. Sitt, G. B. Hitin, I. Hadar, Y. Bekenstein, Y. Amit, I. Popov, U. Banin, *Nat. Mater.* **2014**, *13*, 301.
- [40] H. B. Yang, J. Miao, S. F. Hung, F. Huo, H. M. Chen, B. Liu, *ACS Nano*, **2014**, *8*, 10403.
- [41] L. Yang, C. McCue, Q. Zhang, E. Uchaker, Y. Mai, G. Cao, *Nanoscale*, **2015**,

7, 3173.

- [42] G. Kresse, D. Joubert, *Phys. Rev. B* **1999**, 59, 1758.
- [43] P. E. Blöchl, *Phys. Rev. B* **1994**, 50, 17953.
- [44] G. Kresse, J. Furthmüller, *Comput. Mater. Sci.* **1996**, 6, 15.
- [45] G. Kresse, J. Furthmüller, *Phys. Rev. B* **1996**, 54, 11169.
- [46] G. Kresse, J. Hafner, *Phys. Rev. B* **1993**, 48, 13115.
- [47] J. P. Perdew, K. Burke, M. Ernzerhof, *Phys. Rev. Lett.* **1996**, 77, 3865.
- [48] Y. Li, Y.L. Li, B. Sa, R. Ahuja, *Catal. Sci. Tech.* **2017**, 7, 545.
- [49] S. L. Dudarev, G. A. Botton, S. Y. Savrasov, C. J. Humphreys, A. P. Sutton, *Phys. Rev. B* **1998**, 57, 1505.
- [50] T. Miyake, P. Zhang, M. L. Cohen, S. G. Louie, *Phys. Rev. B* **2006**, 74, 245213.
- [51] M. Ernzerhof, G. E. Scuseria, *J. Chem. Phys.* **1999**, 110, 5029.
- [52] C. Adamo, V. Barone, *J. Chem. Phys.* **1999**, 110, 6158.
- [53] I. C. Man, H. Su, F. Calle-Vallejo, H. A. Hansen, J. I. Martínez, N. G. Inoglu, J. Jitchin, T. F. Jaramillo, J. K. Nørskov, J. Rossmeisl, *ChemCatChem* **2011**, 3, 1159.
- [54] H. Zhang, W. Tian, Y. Li, H. Sun, M. O. Tadé, S. Wang, *J. Mater. Chem. A* **2018**, 6, 6265.
- [55] B. A. Korgel, N. Zaccheroni, D. Fitzmaurice, *J. Am. Chem. Soc.* **1999**, 121, 3533.
- [56] D. Hong, Y. Yamada, T. Nagatomi, Y. Takai, S. Fukuzumi, *J. Am. Chem. Soc.*

2012, *134*, 19572.

- [57] A. L. Kaledin, Z. Huang, Y. V. Geletii, T. Lian, C. L. Hill, D. G. Musaev, *J. Phys. Chem. A* **2010**, *114*, 73.
- [58] W.J. Bao, J. Li, J. Li, Q.W. Zhang, Y. Liu, C.F. Shi, X.H. Xia, *Anal. Chem.* **2018**, *90*, 3842.
- [59] J. E. B. Katari, V. L. Colvin, A. P. Alivisatos, *J. Phys. Chem.* **1994**, *98*, 4109-4117.
- [60] V. Lesnyak, C. George, A. Genovese, M. Prato, A. Casu, S. Ayyappan, A. Scarpellini, L. Manna, *ACS Nano* **2014**, *8*, 8407-8418.
- [61] W. Chen, A. Kahn, P. Soukiassian, P. S. Mangat, J. Gaines, C. Ponzoni, D. Olego, *Phys. Rev. B* **1994**, *49*, 10790.
- [62] U. Weser, G. Sokolowski, W. Pilz, *J. Electron Spectrosc. Relat. Phenom.* **1977**, *10*, 429.
- [63] C. J. Vesely, D. W. Langer, *Phys. Rev. B* **1971**, *4*, 451.
- [64] W. Kohn, L. J. Sham, *Phys. Rev.* **1965**, *140*, A1133.
- [65] P. Hohenberg, W. Kohn, *Phys. Rev.* **1964**, *136*, B864.

4. Colloidal Quasi-One-Dimensional Dual Semiconductor Core/Shell Nanorod Couple Heterostructures with Blue Fluorescence

(Chapter 4 was adapted with permission from D. Chen, A. Wang, H. Li, C. Su, Z. Yin, M. Massi, A. Suvorova, M. Saunders, J. Li, A. Sitt, G. Jia, Colloidal quasi-one-dimensional dual semiconductor core/shell nanorod couple heterostructures with blue fluorescence, *Nanoscale*, 2019, 11, 10190-10197. Copyright 2019 Royal Society of Chemistry.)

4.1 Abstract

Herein we report a nanorod couple heterostructure made of dual semiconductors, in which two parallel aligned ZnSe nanorods are connected by the growth of ZnS on both end and side facets, producing hetero-ZnS (short arms)-ZnSe (long arms)/ZnS shell nanorod couples. As evidenced by electronic structure studies, both experimental and theoretical, such core/shell nanorod couple heterostructures can act as a platform to precisely tailor the quantum confinement of charge carriers between the constituting components within a single nano-object, generating blue fluorescence after the overgrowth of an alloyed ZnCdS layer on the heterostructures. We foresee the mechanistic insights gained and electronic structures revealed in this work would shed light on the rational design of more complex heterostructures with novel functionalities.

4.2 Introduction

Nano-heterostructures that integrate different components together to provide a system with unique dimensionality-dependent integrative and synergic effects¹⁻⁶ are of significant importance due to their diverse applications in solar energy harvesting,^{7,8} catalysis,^{9,10} electronics,^{11,12} biological imaging,^{13,14} and medical diagnostics and treatment.^{15,16} The recent advancements in the protocols of the colloidal synthesis enable the construction of multi-component structures with increasing chemical complexity that can be achieved in a predictable manner via a series of sequential synthetic procedures.^{1,2,12,17,18} In most cases, the preparation of heterostructures involves the sequential growth of one material onto another.^{1,2,18} However, heterostructures that are formed by the joining of two nano-components of the same composition together using a second material are less common in the literature.

As a benchmark heterostructure, CdSe seeded CdS core/shell quantum rods with green to red fluorescence have received significant attention because it provides a platform for the stimulating studies of the elongated nanocrystals in a variety of applications in assemblies, photocatalysis, optoelectronic devices, and bio-labeling.¹⁹⁻²³ However, due to the small band gap of the core material of CdSe and the band offsets of the CdSe/CdS core/shell structure, it is difficult to tune the fluorescence of the CdSe/CdS core/shell quantum rod heterostructures into the blue spectral range. Manna and co-workers have developed a sequential cation exchange approach, in which the Cd^{2+} ion is replaced by Cu^+ and then by Zn^{2+} , to prepare blue-emitting ZnSe/ZnS core/shell quantum rods,²⁴ but this exchange is formed post-

synthesis and involves multi-steps. Hence, to date, the straightforward synthesis of semiconductor quantum rods with blue fluorescence remains highly challenging.

Herein, we report a wet-chemical method for fabricating hetero- ZnS (short arm)-ZnSe/ZnS core/shell (long arm) nanorod couples that are formed by bridging precisely two parallelly aligned ZnSe nanorods with ZnS at their edges. Mechanistic studies reveal that the formation of this heterostructure is attributed to the growth of ZnS between the end facets of each two parallelly aligned ZnSe nanorods, constituting ZnS (short arms)-ZnSe/ZnS core/shell (long arms) nanorod couples. Effective mass approximation (EMA) simulations reveal that the electron occupies only ZnSe states, while the hole occupies a ZnS-ZnS state. Over-coating the nanorod couples with a layer of CdS produces ZnS-ZnSe/ZnCdS core/shell nanorod couples with blue fluorescent, in which the alloyed ZnCdS layer eliminates the surface traps and improves the quantum efficiency. The heterostructures were further converted into hetero-PbS (short arms)-PbSe (long arms)/PbS nanorod couples through a cation exchange reaction.

4.2 Experimental Section

Chemicals: $\text{Zn}(\text{NO}_3)_2 \cdot 6\text{H}_2\text{O}$ (99%), zinc diethyldithiocarbamate (97%), selenium powder (99.999%), CdO (99%), sulfur (99%), bis(trimethylsilyl)sulfide (98%), dodecanethiol (98%), oleylamine (approximate C_{18} content 80–90%), oleic acid (90%, technical grade), 1-octadecene (90%, technical grade), trioctylphosphine (TOP, 97%), trioctylphosphine oxide (TOPO, 90%), toluene (99.8%, anhydrous), chloroform (99%, anhydrous), and methanol (99.8% anhydrous) were purchased

from Sigma-Aldrich. Octadecylphosphonic acid (ODPA) and hexylphosphonic acid (HPA) were purchased from PCI Synthesis. All chemicals were used as received without further purification.

Preparation of Zinc Precursor Stock Solution: A 0.067 M zinc stock solution was prepared by dissolved $\text{Zn}(\text{NO}_3)_2 \cdot 6\text{H}_2\text{O}$ (0.2 mmol) in oleylamine (10 mL) in a three-neck flask. The mixture was degassed and refilled with N_2 three times at room temperature and then heated to 110 °C and kept at this temperature under vacuum for 30 minutes. Then the mixture was further heated up to 160 °C and kept at this temperature for 30 minutes.

Synthesis of thin ZnSe nanorods: Thin ZnSe nanorods synthesis was conducted according to a previously reported approach with some modifications.²⁶ In a typical synthesis, 0.2 mmol (59.5 mg) $\text{Zn}(\text{NO}_3)_2 \cdot 6\text{H}_2\text{O}$ and 10 mL oleylamine were mixed in a three-neck flask. The mixture was degassed and refilled with N_2 three times at room temperature and then heated to 110 °C and kept at this temperature for 0.5 hour. At 160 °C, 2 mL 0.1 M Se oleylamine solution was injected into the flask. After the injection, the temperature was set at 120 °C and the mixture was degassed for 10 minutes. After the flask was refilled with N_2 , the temperature was raised up to 230 °C in 6 minutes. After 20 minutes at 230 °C, the reaction was quenched by removing the heating mantle.

Purification of thin ZnSe nanorods: Purification of nanoparticles was conducted by dissolving 2 mL of the crude solution into 2 mL chloroform solution. Then methanol was continuously added into the solution until a turbid solution was obtained. The precipitation was separated from the solution by the aid of centrifugation and this procedure may repeat two or three times.

Synthesis of hetero- ZnS-ZnSe/ZnS core/shell Nanorod Couples: 30 mg purified thin ZnSe nanorods were dissolved in 15 mL oleylamine in a three-neck flask and then 4 mL 0.067 M zinc precursor stock solution was added into the flask. The mixture was degassed and refilled with N₂ three times at room temperature and then heated to 110 °C and kept at this temperature for 30 minutes under vacuum. Then the mixture was heated to 260 °C in 7 minutes. At 260 °C, 1 mL (4.17 mmol) of 1-dodecanethiol was injected into the flask. After the injection, the temperature was raised to 280 °C in four minutes. After 30 minutes at 280 °C, the reaction was quenched by removing the heating mantle. Aliquots have been taken from time to time to monitor the growth of nanoparticles. Other sulfur source, such as (4.0 mmol) bis(trimethylsilyl)sulfide, has been used to substitute 1-dodecanethiol for synthesis of branched nanorod couples. The synthetic conditions for the synthesis of hetero- ZnS-ZnSe/ZnS core/shell nanorod couples using bis(trimethylsilyl)sulfide as the sulfur source are exactly same as above except 1-dodecanethiol has been replaced by bis(trimethylsilyl)sulfide.

Synthesis of homo- ZnSe Nanorod Couples: The synthesis of homo- ZnSe nanorod couples was conducted according to a previously reported approach with some modifications.²⁶ In a typical synthesis, 30 mg purified thin ZnSe nanorods was dissolved into 15 mL oleylamine solution into a three-neck flask. 1 mL 0.067 M zinc oleylamine and 1 mL 0.067 M selenium oleylamine stock solutions were added the flask at room temperature. Then the reaction solution was gradually heated up to 280 °C in 15 minutes and kept at this temperature for 30 minutes. The reaction was quenched by removing the heating mantle. Aliquots have been taken from time to time to monitor the growth of nanoparticles.

Etching of ZnSe Nanorods: 30 mg purified thin ZnSe nanorods were synthesized by a reported approach^{26,44} and were dissolved in 15 mL oleylamine in a three-neck flask and then 4 mL 0.067 M zinc precursor stock solution was added into the flask. The mixture was degassed and refilled with N₂ three times at room temperature for three times and then heated to 110 °C and kept at this temperature for 30 minutes under vacuum. Then the mixture was heated to 260 °C in 7 minutes. At 260 °C, a certain amount of 1-dodecanethiol was injected into the flask. After the injection, the temperature was raised to 280 °C in four minutes. After 30 minutes at 280 °C, the reaction was quenched by removing the heating mantle. Aliquots have been taken from time to time to evolution of the nanoparticles.

Synthesis of ZnSe/ZnCdS Core/Shell Nanorod Couples: For the CdS shell growth, CdO (15 mg), trioctylphosphine oxide (2.0 g), octadecylphosphonic acid (75 mg) and hexylphosphonic acid (10 mg) were added to a three-neck flask (50 ml). The mixture was heated to 150 °C for 0.5 h under vacuum and then rise to 320 °C at N₂ to obtain a colourless solution. After that, the mixture was heated and stabilized at 365 °C and 3 ml TOP solution dissolved with 1×10^{-9} mol branched hetero- ZnS-ZnSe nanorod couples and 30mg sulfur was swiftly injected into the flask. After 30 seconds, the reaction was quenched by ice bathing. The crude reaction solution was diluted with toluene, methanol was added to precipitate the nanocrystals and remove excess surfactants.

Synthesis of Branched Hetero- PbS-PbSe Nanorod Couples: The cation exchange method was used to obtain branched hetero- PbS-PbSe nanorod couples from branched hetero- ZnS-ZnSe nanorod couples. A 0.05 M lead oleate stock solution was prepared by dissolving lead acetate (1 mmol) in a mixture of oleic acid (0.88 ml)

and octadecene (19.12 ml) at 180 °C. The purified branched hetero- ZnS-ZnSe nanorod couples was dissolved in 1 mL anhydrous chloroform and then injected into 5 ml oleylamine in a 15 ml three-neck flask. After place in vacuum for 10 min, lead oleate stock (0.05 M) solution was injected into the flask and the temperature was raised to 100°C. After 5min at this temperature, the colorless solution transformed to dark brown, which indicates the Zn^{2+} ions have been substituted by Pb^{2+} . The solution was quenched by ice bathing and the obtained solution was washed by toluene and precipitated by methanol with the aid of centrifugation.

Synthesis of CdS rods: CdS nanorods were prepared using a literature method.²⁵ In a typical synthesis, CdO (60 mg), trioctylphosphine oxide (3.0 g), octadecylphosphonic acid (290 mg) and hexylphosphonic acid (45 mg) were added to a three-neck flask (50 ml). The mixture was heated to 150 °C for 0.5 h under vacuum and then rise to 320 °C at N_2 to obtain a colourless solution. After that, the mixture was heated and stabilized at 365 °C and 1.8 ml TOP solution dissolved with 4×10^{-8} mol CdS spherical dots and 60 mg sulfur was swiftly injected into the flask. After 9 minutes, the reaction was quenched by ice bathing. The crude reaction solution was diluted with toluene, methanol was added to precipitate the nanocrystals and remove excess surfactants with the aid of centrifugation.

Sample Characterization.

UV-vis Absorption Spectroscopy: UV-vis absorption spectroscopy was performed on a Perkin Elmer Lambda 35 UV/VIS Spectrometer using quartz cuvettes.

Photophysical measurements: Uncorrected steady-state emission spectra were recorded using an Edinburgh FLSP980-stm spectrometer equipped with a 450 W xenon arc lamp, double excitation and emission monochromators, a Peltier-cooled

Hamamatsu R928P photomultiplier (185-850 nm). Emission spectra were corrected for source intensity (lamp and grating) and emission spectral response (detector and grating) by a calibration curve supplied with the instrument. Overall quantum yields were measured with the use of an integrating sphere coated with BenFlect. Fluorescence emission lifetimes (τ) were determined with the time-correlated single photon counting technique (TCSPC) with the same Edinburgh FLSP920 spectrometer using pulsed picosecond LEDs (EPLED 280 or EPLED 320, FWHM <800 ps) as the excitation source, with repetition rates between 10 kHz and 1 MHz, and the above-mentioned R928P PMT as detector. To record the fluorescence spectra at 77 K, the samples were placed in quartz tubes (2 mm diameter) and inserted in a special quartz Dewar filled with liquid nitrogen. To measure the fluorescence spectra at different temperatures from 77 K to 287 K, the samples were placed in quartz cuvettes in a liquid nitrogen cryostat (Oxford Instrument). All the solvents used in the preparation of the solutions for the photophysical investigations were of spectrometric grade. Experimental uncertainties are estimated to be $\pm 10\%$ for lifetimes and $\pm 20\%$ for quantum yields.

XRD Measurement: XRD patterns were obtained using Cu K α ($\lambda=1.5406$ Å) photons from an X'per PRO (PANalytical) X-ray diffractometer operated at 40 kV and 40 mA. Samples were deposited as a thin layer on a low-background scattering quartz substrate.

TEM Measurement: TEM grids were prepared by depositing one drop of a solution of purified nanoparticles onto a standard carbon coated grid. TEM was performed using a JEOL 2100 transmission electron microscope with a tungsten filament running at an accelerating voltage of 120 keV. HRTEM, HAADF-STEM, High-

resolution Z-contrast STEM and STEM-energy-dispersive X-ray spectroscopy (EDX) were performed on an FEI Titan G2 80-200 high-resolution transmission electron microscope running at an accelerating voltage of 200 keV with a field emission gun as an electron source.

4.3 Results and Discussion

4.3.1 Controlled Synthesis and growth mechanism of hetero- ZnS (short arm)-ZnSe/ZnS core/shell (long arm) nanorod couples

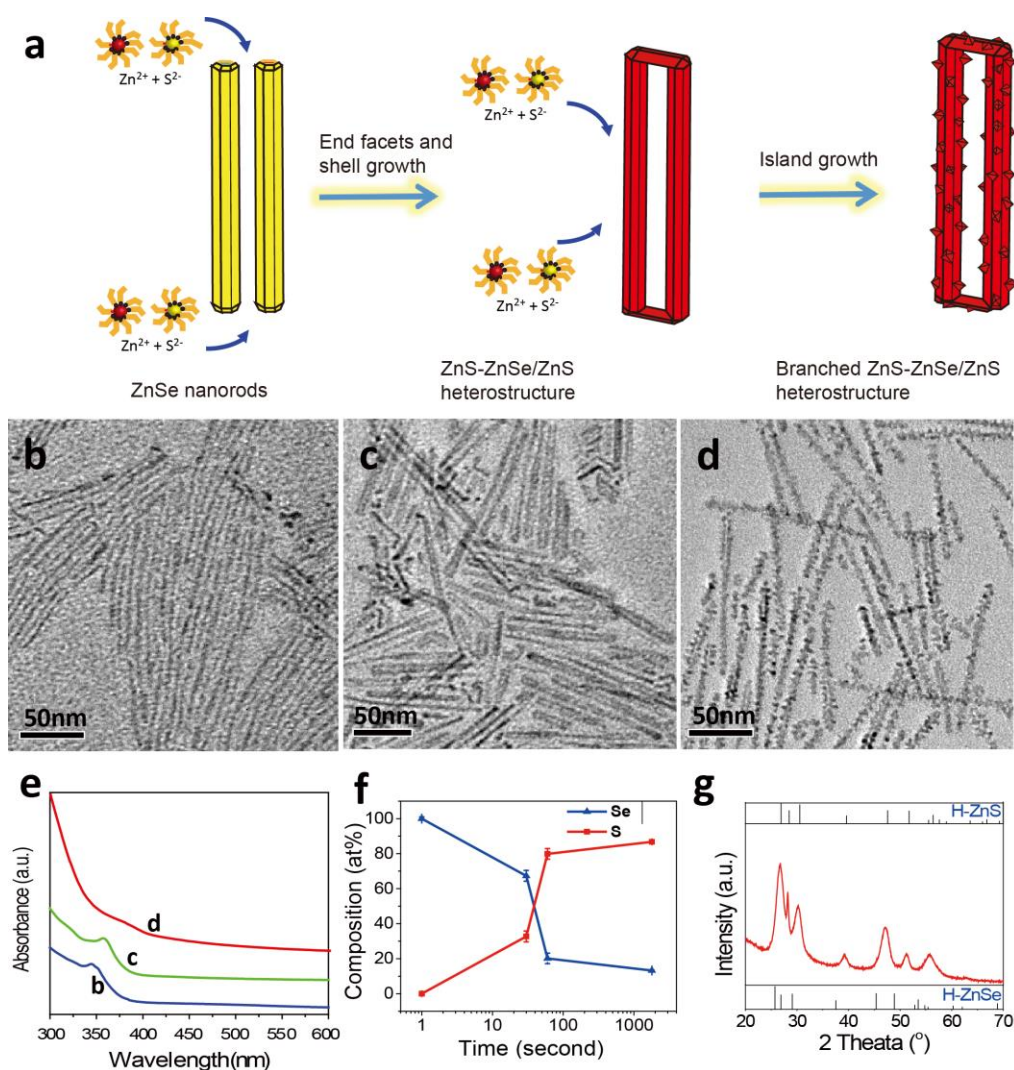


Fig 1. (a) A schematic illustration showing a controlled synthesis of ZnS (short arms)-ZnSe/ZnS core/shell (long arms) heterostructures. (b-d) TEM images of (b) the original thin ZnSe nanorods, (c) the hetero-ZnS-ZnSe/ZnS core/shell nanorod couples obtained after 30 seconds at 280 oC, and (d) the branched hetero- ZnS-ZnSe/ZnS core/shell nanorod couples obtained after 30 minutes at 280 oC. (e) Absorption spectra corresponding to (b-d). (f) Chemical composition of Se (%) and S (%) of branched hetero-ZnS-ZnSe/ZnS core/shell nanorod couples as a function of the reaction time (1 second, 30 seconds, 1 minute and 30 minutes, respectively). (g) XRD patterns of branched hetero- ZnS-ZnSe/ZnS core/shell nanorod couples.

The hierarchical self-assembly processes in the growth of nanorod couples allow the separation of the intermediate products from the reaction system and the manipulation of the particle growth in a controlled manner.^{26,27} We took this into advantage by incorporating both Zn and S precursors together with the purified ZnSe nanorods into the reaction system to synthesize hetero-ZnS (short arm)-ZnSe/ZnS core/shell (long arm) nanorod couples (Figure 1a). Surprisingly, after the reaction has evolved for 30 seconds, Zn (zinc nitride) and S precursors (1-dodecanthiol) integrated two ZnSe nanorods into a single hetero-nanorod couple (Figure 1b) by the growth of ZnS on both end facets of two parallelly aligned ZnSe nanorods (Figure 1c). Further growth of ZnS islands on side facet of the long arms was obtained as the reaction continued (Figure 1d). Analogous to the previously reported single-component ZnSe nanorods couples,²⁷ the driving forces responsible for the initial pairing of ZnSe nanorods with ZnS are dipole-dipole and crystal-crystal interactions. The pairing of ZnSe rods via bridging both end facets by ZnS is formed via a self-limited assembly mechanism, because once the end facets of ZnSe are blocked by the growth ZnS, the hetero-ZnSe-ZnS nanorod couple cannot interact with another ZnSe nanorod.²⁷ Upon the growth of ZnS shell, the absorption onset exhibits a slight red-shift of 7 nm as a result of the leakage of the excitonic wave function into the ZnS layer.^{28,29} A prolonged reaction time of 30 minutes (Figure 1d) produced branched hetero-ZnS-ZnSe/ZnS nanorod couples with ZnS decorating the surface of the nanorod couple heterostructures. The corresponding absorption onset is slightly smeared, but clearly, a further red shift is observed. The islands growth of ZnS at prolonged time may be a result of the lattice strain existing between interfaces of the

ZnSe and ZnS,³⁰ which may also result in the red shift of absorption as previously observed in ZnSe/ZnS core/shell nanoparticles.³¹ Statistical analysis (Figure 2) shows that the lengths of the original nanorods (Figure 1b), intermediate (Figure 1c) and final products (Figure 1d) are almost constant (72.0 nm to 78.7 nm), but their widths change from 2.5 nm to 5.6 nm, and then to 7.5 nm. The increase of width correlates to both the growth of ZnS on both end and side facets of two parallelly aligned ZnSe nanorods. A distinct spacing between two rod components (Figure 1c, 1d) is seen, which can be attributed to the steric hindrance of the oleylamine ligands passivating on the surface of each rod components. Energy dispersive X-ray (EDX) spectroscopy analysis shows that the atomic ratio of Se:S decreases as a function of the reaction time (Figure 1f), which is consistent with the growth of ZnS on the ZnSe nanorod components. The powder X-ray diffraction (XRD) patterns of hetero-ZnS-ZnSe/ZnS core/shell nanorod couples present a shift to higher angles with respect to those of pure ZnSe, which further confirms the growth of the ZnS (Figure 1g).

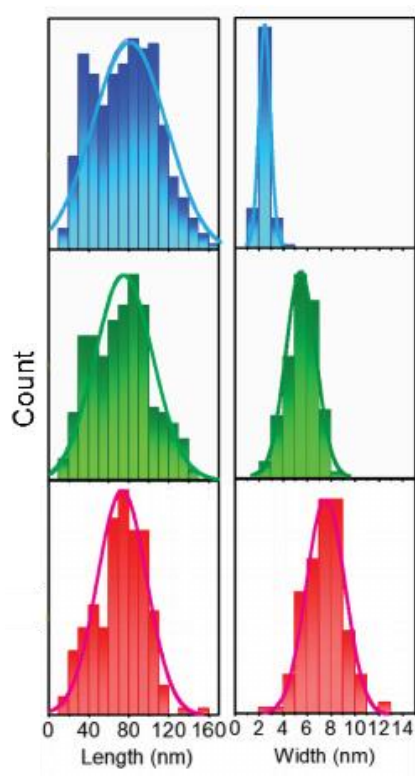


Figure 2. Sizing histograms of original ZnSe nanorods (top panel), hetero- ZnS-ZnSe/ZnS nanorod couples obtained after 30 seconds at 280 °C (middle panel), and branched hetero- ZnS-ZnSe/ZnS nanorod couples obtained after 30 minutes at 280 °C (bottom panel).

Using bis(trimethylsilyl)sulfide as the sulfur source instead of 1-dodecanethiol while keeping other synthetic conditions constant also produced hetero-ZnS-ZnSe/ZnS core/shell nanorod couples (Figure 3) with an even smaller spacing between the two ZnSe rods. The high activity of bistrimethylsilyl)sulfide leads to the fast growth of ZnS and its high etching capability at elevated temperatures may result such a small spacing between each rod components of the hetero- nanorod couples.³² This demonstrated the generality of this synthetic approach for compositing hetero-nanorod couples. The above control experiment also demonstrated that two

elongated nanorods can be integrated into a single nano-object in a predefined way through material engineering and optimization of synthetic protocols.

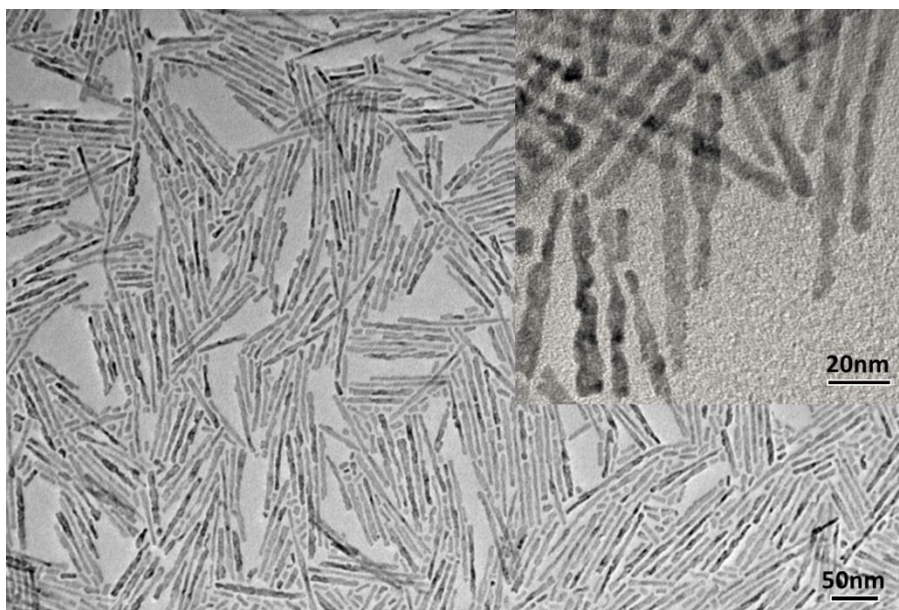


Figure 3. TEM image of hetero- ZnS-ZnSe/ZnS core/shell nanorod couples synthesized using bis(trimethylsilyl)sulfide as the sulfur source. Inset show a zoom-in of nanoparticles.

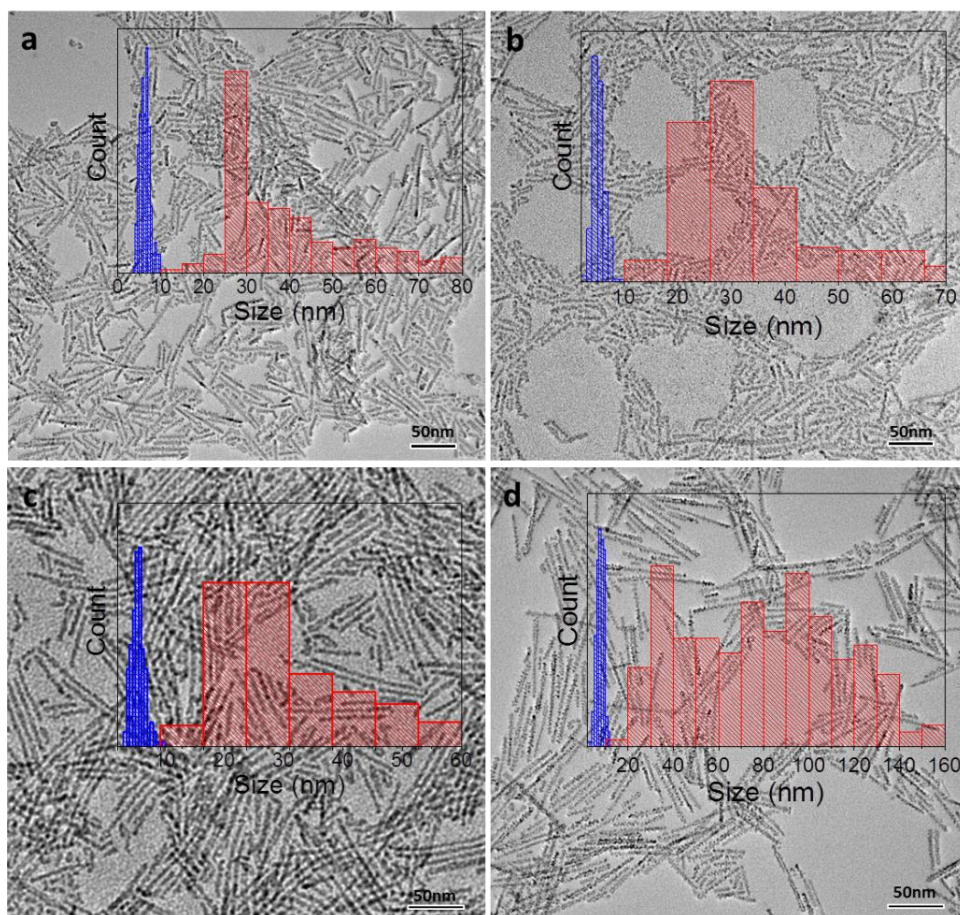


Figure 4. TEM images and sizing histograms of branched hetero- ZnS-ZnSe/ZnS nanorod couples with different dimensions. (a) Length (42.3 ± 17.9 nm) \times width (6.3 ± 1.2 nm). (b) Length (37.7 ± 20.5 nm) \times width (5.3 ± 1.1 nm). (c) Length (45.1 ± 23.4 nm) \times width (5.4 ± 1.1 nm). (d) Length (79.6 ± 35.2 nm) \times width (7.7 ± 1.6 nm).

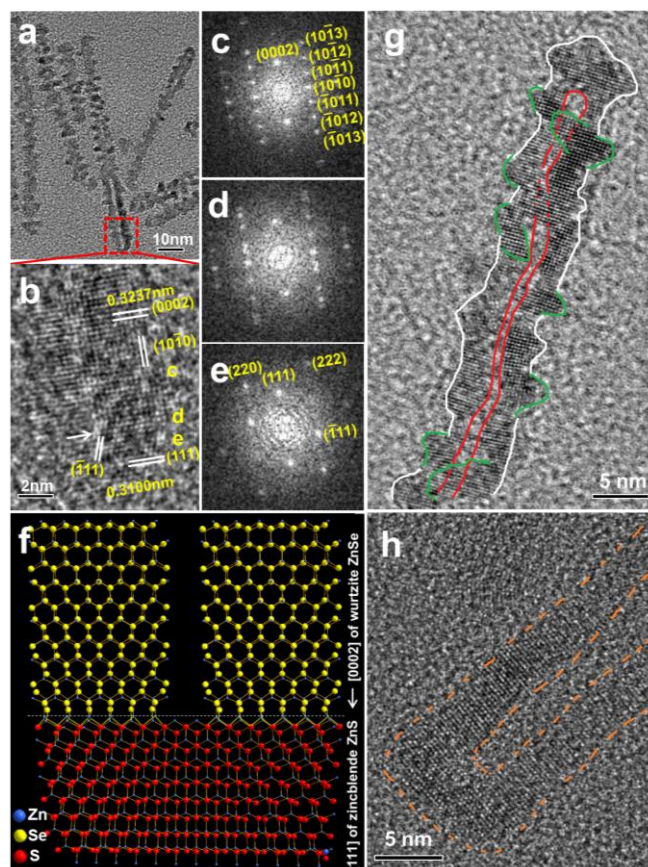


Fig 5. (a) TEM image. (b) HRTEM image of the short arm marked by dashed rectangle in (a). The boundary between wurtzite hexagonal (H-) ZnSe and zincblende cubic (C-) ZnS is labelled by an arrow. (c-e) FFT of selected areas in (b) revealing the crystallographic relations. The diffraction patterns in (c) and (e) match H-ZnSe and C-ZnS, respectively. (f) Schematic atomic crystal structure corresponding to the region depicted in (b). (g) HRTEM image of an individual branched nanorod couple. White lines outline boundary of the branched nanorod couple, green lines outline the ZnS branches, and red lines outline the gap between two rods. (h) HRTEM image of the branched hetero- ZnS-ZnSe/ZnS/CdS core/shell/shell nanorod couples revealing a clear gap (marked by dashed orange lines) between two rods.

We used transmission electron microscope (TEM) imaging in combination with fast Fourier transform (FFT) analysis to reveal how hetero- ZnS-ZnSe/ZnS core/shell nanorod couples form from two parallelly aligned ZnSe nanorods in the presence of Zn and S precursors. Figures 3a and 4 show the branched hetero- ZnS-ZnSe/ZnS core/shell nanorod couples with different dimensions. Close inspection on the connecting areas of the heterostructures (labelled by dashed red rectangle in Figures 5a, 6a and 6f) show that a single heterostructure is formed through ZnS growth on both end facets of two parallelly aligned ZnSe nanorods. The (111) plane of zincblende ZnS grows on the (0002) plane of wurtzite ZnSe nanorods, creating the connecting areas (Figures 5b, 6b and 6g), as confirmed by the presence of two sets of diffraction patterns (Figures 5d, 6d and 6i) of both zincblende ZnS (Figures 5e, 6e and 6j) and wurtzite ZnSe (Figures 5c, 6c and 6h) in close proximity of the boundary. We attribute the growth of (111) zincblende ZnS on the (0002) plane of the ZnSe wurtzite to the moderate lattice mismatch between these two planes, which is about 3.9% (Table S1).³³⁻³⁵ Based on above diffraction analysis, we propose the atomistic crystal structure shown in Figure 5f to explain how zincblende ZnS short arms join the end facets of two parallelly aligned ZnSe nanorods.

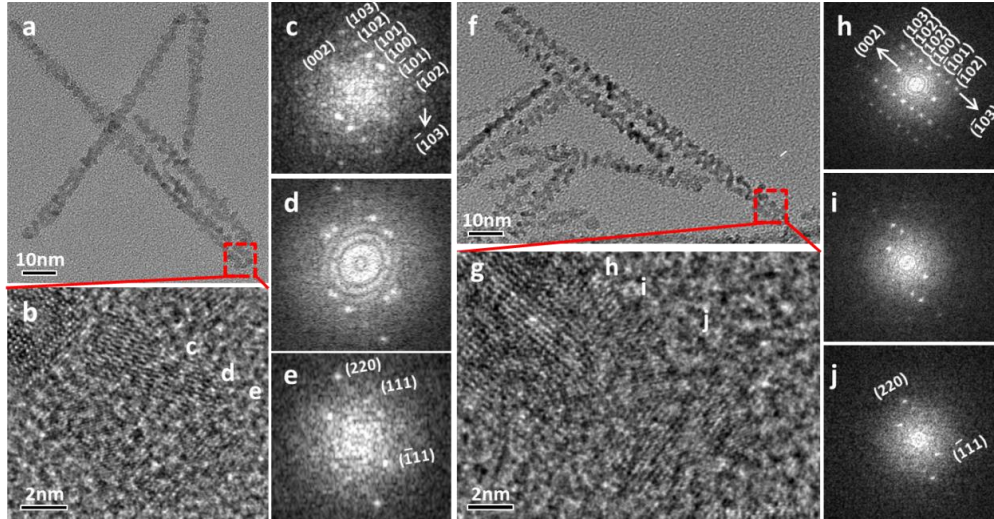


Figure 6. Electron microscopy imaging characterizations of hetero- ZnS-ZnSe/ZnS core/shell nanorod couples. (a) TEM image. (b) HRTEM image of the short arm labelled by dashed rectangle in (a), showing a hetero- nanorod couple is formed by the growth of zincblende ZnS between the end facets of two parallelly aligned wurtzite ZnSe nanorods. (c-e) FFT of selected areas in (b) revealing the crystallographic relations. The diffraction patterns in (c) and (e) match wurtzite ZnSe and zincblende ZnS, respectively. (d) shows the concurrence of above two sets of diffraction patterns. (f) TEM image. (g) HRTEM image of the short arm labelled by dashed rectangle in (f). (h-i) FFT of selected areas in (g) revealing the crystallographic relations. The diffraction patterns in (h) and (j) match wurtzite ZnSe and zincblende ZnS, respectively.

The orientation of the crystal lattices of branched structures is similar to that of the ZnSe rod couples, as is confirmed by HRTEM characterization (Figures 5g, 7) and the FFT analyses (insets of Figure 7). An evident spacing between the rods is observed in individual hetero-ZnS-ZnSe nanorod couples (Figures 8-10). The

boundaries of the nanorods couples, and in particular the gap between them, became more evident after coating of the hetero-ZnS-ZnSe/ZnS core/shell nanorod couples with a shell layer of CdS (Figure 5h) (see Experimental Section in ESI for details). This is mainly a result of the surface reconstruction of the branched ZnS structures on the surface of the hetero-nanorod couples, which occurs at the high growth temperature that is required for the CdS shell growth.

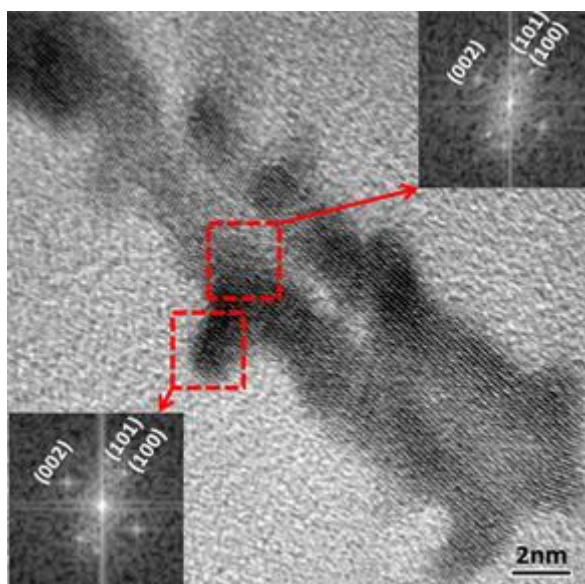


Figure 7. TEM images of “dual” nanorods showing the gap between two rod components. Insets show the FFT analyses of the selected areas.

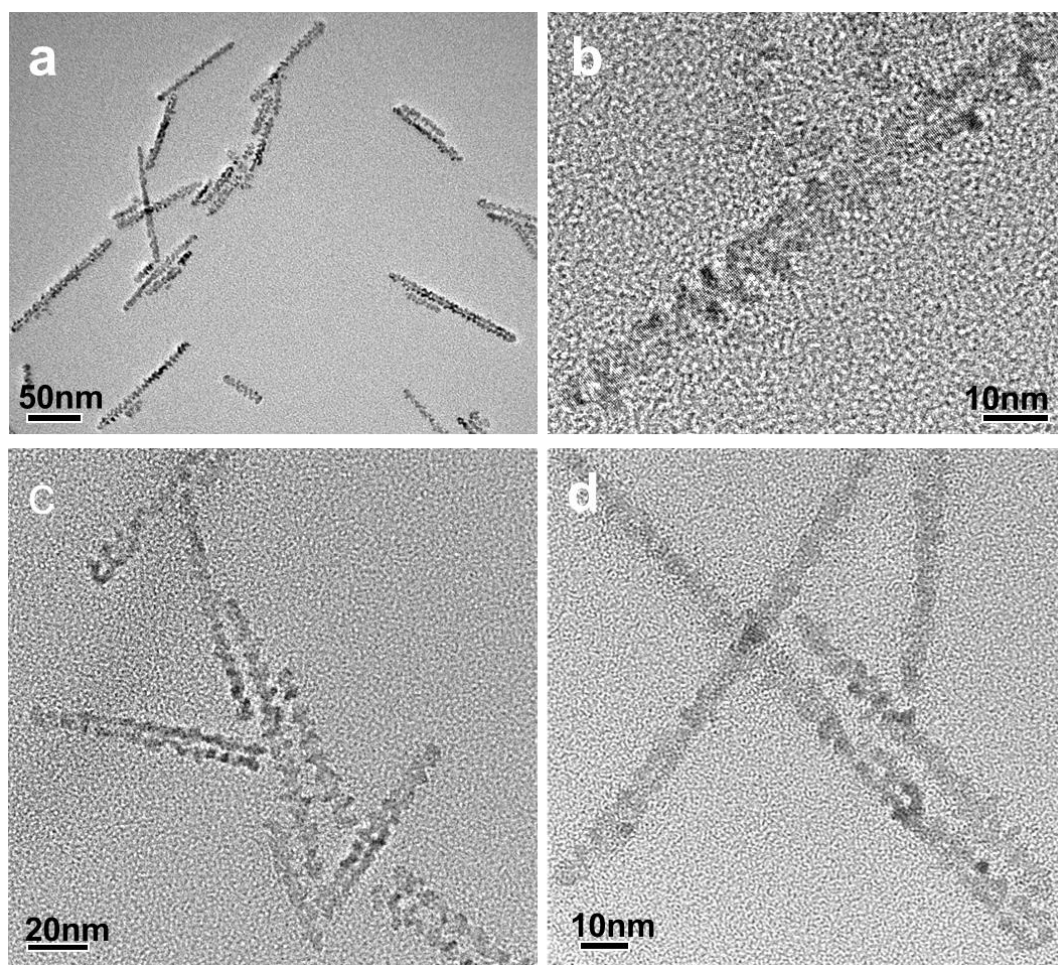


Figure 8. TEM images of hetero- ZnS-ZnSe/ZnS nanorod couples showing the gap between two rod components.

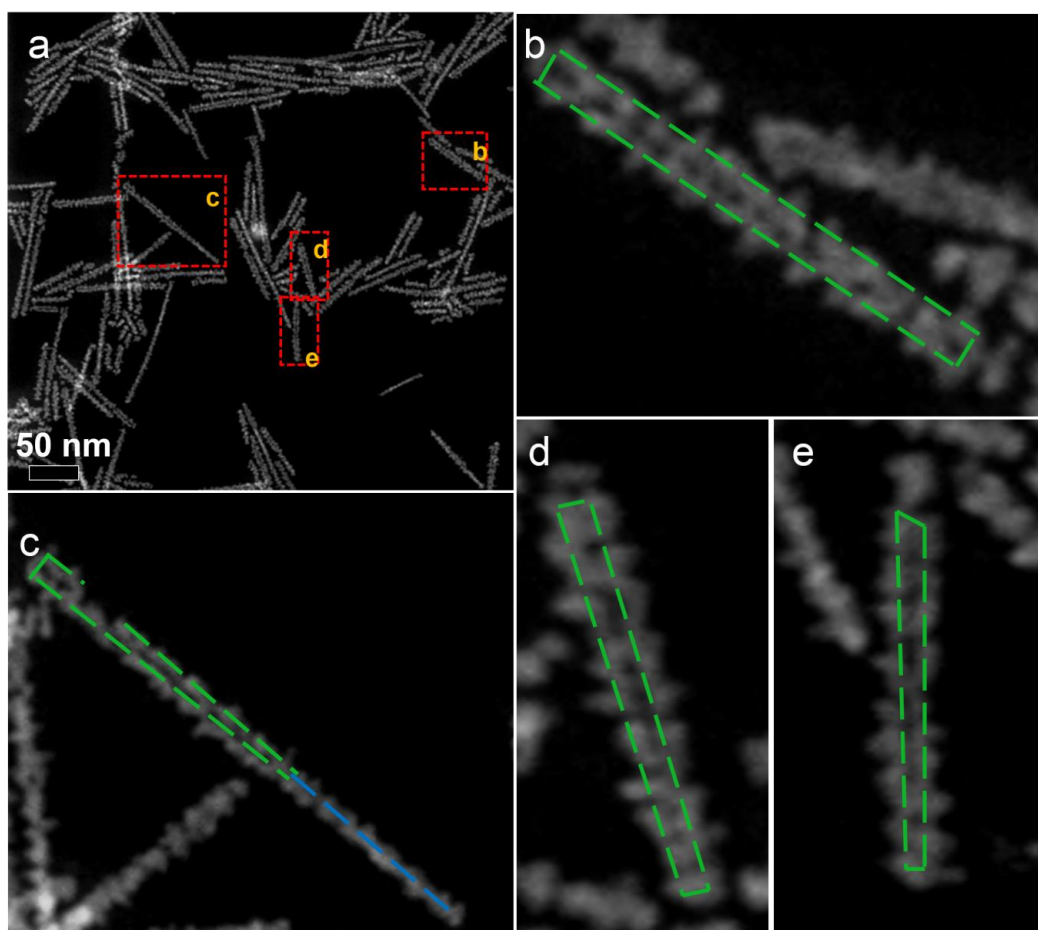


Figure 9. HAADF-STEM images showing the gap between two rod components of hetero- ZnS-ZnSe/ZnS nanorod couples. (a) Branched hetero- nanorod couples. (b-e) Enlarged images of individual nanoparticle as marked by red rectangles in (a). The green lines outline the long rod components, and blue line indicates single rod features of a branched nanorod couple which was formed due to partial coalesce of side facet of the “dual rods” occurred at elevated temperatures, e.g. 280 °C.

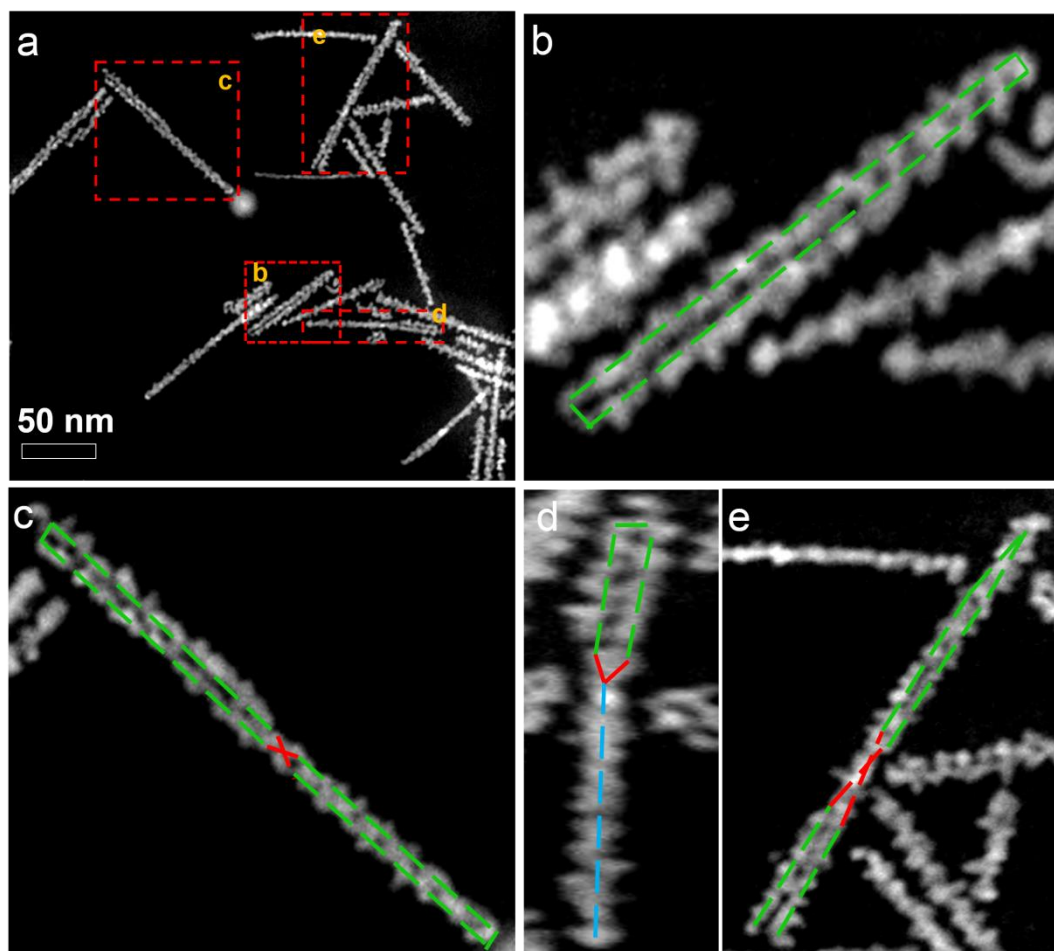


Figure 10. HAADF-STEM images of a) branched hetero- nanorod couples. b,c,d,e) Enlarged images of particles marked by red rectangles in a). The green lines outline the long rod components, and blue line indicates single rod features of a branched nanorod couple, and the red cross indicates the twist features of branched nanorod couples.

In general, the features of branched nanorod couples can be recognized with the guide of the green lines marked in the enlarged HAADF-STEM images. It is evident that the majority of branched nanorod couples remains the “dual rods” features. In Figure S7c and S8d, some parts of branched nanorods couples show single rod feature because of the partial coalesce of side facet of the “dual rods” occurred at

elevated temperatures, e.g. 280 °C. Other branched nanorods couples also show twisting, as marked by red cross, which is also observed in the previously reported ZnSe nanorod couples.²⁷

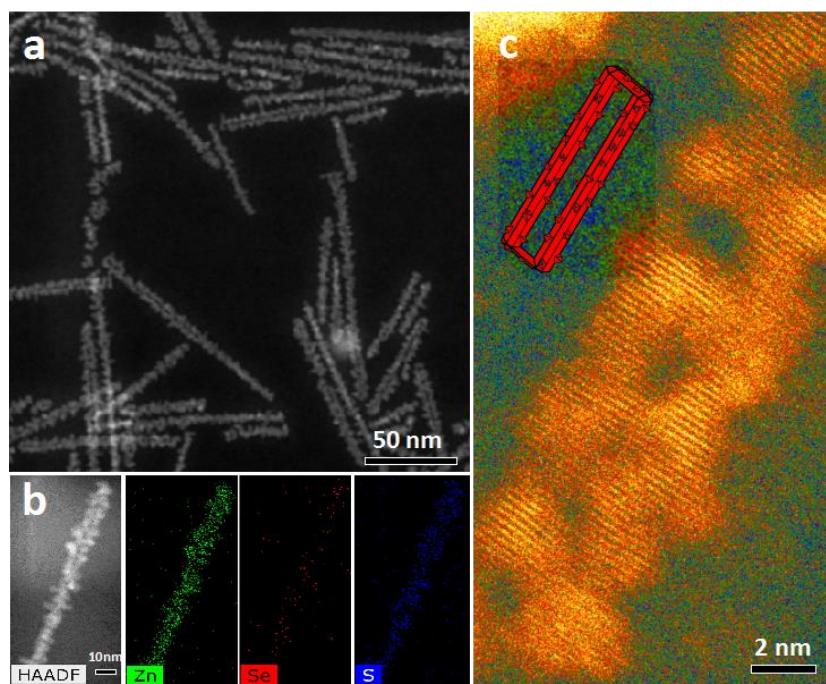


Fig 11. (a) HAADF-STEM image of hetero-ZnS-ZnSe/ZnS core/shell nanorod couples showing a spacing between each two rods. (b) HAADF-STEM image and elemental maps of an individual hetero- ZnS-ZnSe/ZnS core/shell nanorod couple. (c) A high-resolution Z-contrast STEM image of an individual hetero- ZnS-ZnSe/ZnS core/shell nanorod couple.

High angle annular dark field-scanning transmission electron microscopy (HAADF-STEM) confirms the formation of the branched structures on the surface of hetero-ZnS-ZnSe/ZnS core/shell nanorod couples (Figure 11a). Some particles that

resemble single rods can also be identified in the micrograph, but they exhibit a higher contrast, which indicates that these are rod-couples, which are positioned in a perpendicular alignment on top of amorphous carbon film (Figure 11a). HAADF-EDX element mapping confirms the presence of Zn, Se and S elements in the hetero-nanorod couples (Figures 11b, 12) and Zn^{2+} ions are evenly distributed throughout the elongated nanoparticles (Figure 11b). Close inspection on the element maps of Se^{2-} and S^{2-} ions indicates Se^{2-} ions are predominately distributed on the inner side of the obtained nanorod couples whereas S^{2-} ions are initially located on the outer side of the nanoparticles. This confirms the formation of ZnS-ZnSe/ZnS core/shell nanorod couples accompanied with the extensive growth of ZnS branched structures on the ZnSe rod components. Apparently, the mapping of Se element is weak, which is in consistence with the low molar ratio of Se ($\sim 13\%$) in the branched hetero-ZnS-ZnSe/ZnS core/shell nanorod couples (Figure 1f). The Z-contrast STEM image (Figure 11c) shows that the spacing between two rod components is not continuous and may be interrupted by the fuse of the adjacent facets of two rods. This image also confirms that ZnS branched structures have grown on both exterior sides and the interior sides of the rod components of nanorod couples.

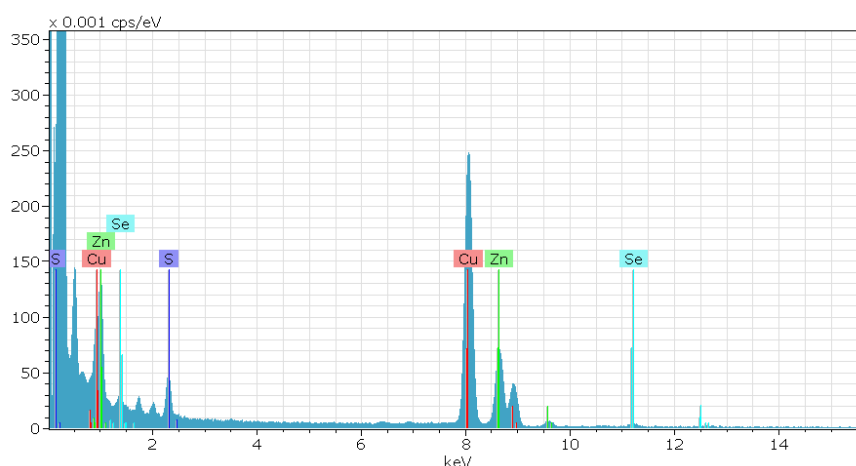


Figure 12. EDX spetrum of branched hetero- ZnS-ZnSe/ZnS core/shell nanorod couples confirming the presence of Zn, Se and S elements.

Table 1. Comparison of lattice mismatches of the nanostructures.

Initial material	(0002) wurtzite ZnSe	(0002) wurtzite ZnSe	(0002) wurtzite ZnSe
Second material	(111) zincblende ZnS	(0002) wurtzite ZnS	(0002) wurtzite CdS
Mismatch (%)	3.9 ³³	4.5 ³⁶	3.4 ^{37,38}

The mismatches were calculated by the equation below:

Lattice mismatch = (lattice parameter of initial material – lattice parameter of a second material)/ lattice parameter of initial material.

(The lattice plane spacings for (0002) of wurtzite ZnSe, (111) of zincblende ZnS, (0002) of wurtzite ZnS and (0002) of wurtzite CdS are 0.32500 nm, 0.3123 nm, 0.31292 nm and 0.33599 nm, respectively.)

One of the intriguing questions regarding the presented system is why does the growth of ZnS on the surface of hetero-ZnS-ZnSe nanorod couples leads to branched structures. Obviously, this is not due to the compatibility between these two

materials since the lattice mismatch between ZnS (wurtzite) and ZnSe (wurtzite) is not very large (4.5%) (Table 1). In a control experiment, ZnSe nanorods were dissolved into the same reaction solvent in the presence of the same sulfur precursor, i.e. 1-dodecanethiol, at a reaction temperature of 280 °C. Under these conditions, the ZnSe nanorods were partially etched, leading to rods with rough surface facets (Figure 13). This process highly resembles the etching of CdS nanorods in the presence of zinc oleate.³⁹ Thus we believe that in the case of the ZnS-ZnSe/ZnS nanorod couples, the surface of the ZnSe rods is etched, and at the same time, ZnS grows epitaxially on the rough surface facets of the nanorod couples, leading to the formation of branched structures.

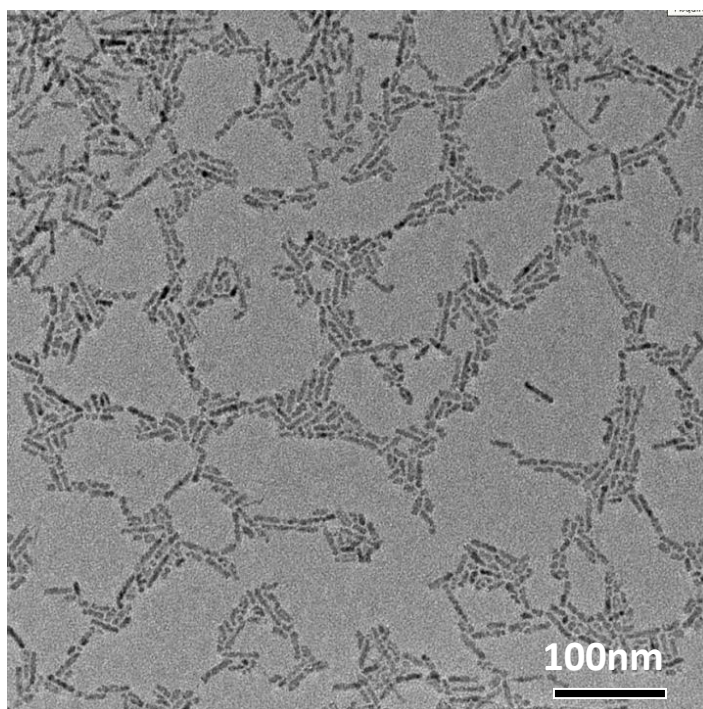


Figure 13. TEM images of etched ZnSe nanorod with rough surface facets obtained in oleylamine solution in the presence of 1-dodecanethiol after the reaction evolved for 30 minutes at 280 °C.

It is worth noting that the structure of the zinc blende ZnS short arms connecting the end facets of two parallel ZnSe nanorods is different from that of the wurtzite ZnS shell grown on the side facets of the ZnSe nanorods. This can be explained by the relatively small difference in the total energy between zinc blende and wurtzite phases of ZnS (3.1 meV/atom)⁴⁰ and the different types of growth of ZnS with respect to the pre-existing ZnSe. In the former case, the growth of the zinc blende structured ZnS on the wurtzite structured ZnSe nanorods only occurred on a small region, i.e. the most reactive end facets of ZnSe nanorods. This is unlikely lead to substantial lattice strain at the interfaces between the short ZnS arms and the end facets of ZnSe nanorods. In addition to the effect of lattice mismatch, kinetic effect of reaction precursors may also affect the phase of ZnS because the crystallization of zinc blende-structured ZnS is preferred at high supersaturation of zinc and sulfur precursors.⁴¹⁻⁴³ However, in the latter case, wurtzite structured ZnS growth on the elongated side facets of wurtzite structured ZnSe is preferred because this can significant reduce the lattice strain and increase the stability of the core/shell structure.

4.3.2 Electronic structure of hetero-ZnS (short arm)-ZnSe/ZnS core/shell (long arm) nanorod couples

A finite well effective mass approximation (EMA) approach⁴⁴ was used to study the electronic structure of the hetero-ZnSe-ZnS/ZnSe core/shell nanorod couples, and in particular to compare them to that of homo- ZnSe nanorod couples. Due to the complex shape of the system, the solution was performed numerically using a finite element based model obtained with COMSOL Multiphysics package.

Within the EMA, we modeled the excited charge carrier confined to the particle as a particle in a box. Under this approximation, the Schrödinger equation for the electron (hole) envelope wave functions, φ_a , is defined as

$$\left(-\frac{\hbar}{2m_a^*} \nabla^2 + V_a \right) \varphi_a = E_a \varphi_a, \quad a = e/h \quad (1)$$

where \hbar is the reduced Planck constant, m_a^* is the reduced mass and V_a is the potential energy exerted on the charge carrier in the medium.

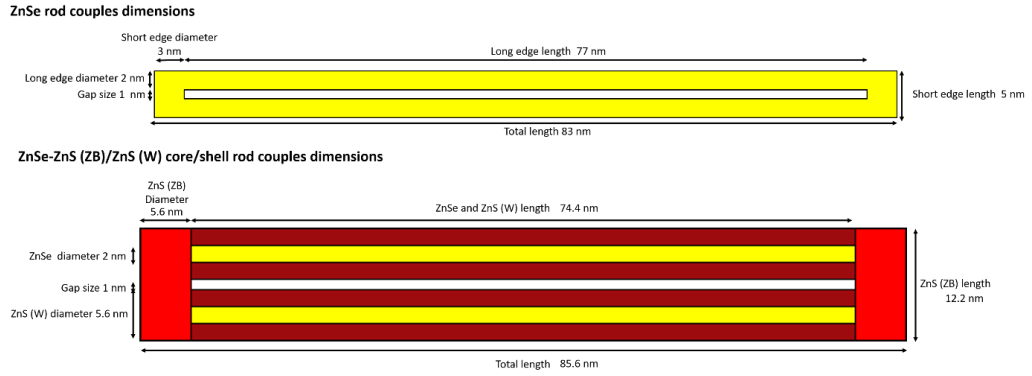
The total exciton energy can be calculated by

$$E = E_{bg} + E_e + E_h \quad (2)$$

where E_{bg} is the bulk's band gap. The potential energy of the charge carriers within the particle is taken as zero. The potential energy outside the particle, which determines the height of the well's wall, was set to $V_{ligands} = [E_{LH}(ligands) - E_{bg}(ZnSe)]/2$, where $E_{LH}(ligands)$ is the energy difference between the LUMO and HOMO energies of the ligand. For oleylamine, $E_{LH}(ligands) = 4.430 \text{ eV}$.⁴⁵

In this calculations, Coulomb, Exchange, and Correlation interactions were neglected as they were not easily obtained for elongated systems, and may further shift the exciton's energy. We took both the bulk band gap energy for ZnSe and ZnS and the effective masses from references⁴⁶⁻⁵¹, and are summarized in Table 2. The hole states correspond to the heavy hole, which dominates the valence band-edge states in this system.

Scheme 1: Dimensions of the different systems used for calculating the electronic structures.



Comparison between the electronic structure of hetero-ZnSe-ZnS/ZnS nanorod couples and homo- ZnSe was obtained for systems of similar ZnSe dimensions. All geometric parameters were set according to the dimensions extracted from TEM images and are shown in Scheme 1. The particles were embedded in an environment of organic material, with wave functions set to zero at the boundaries. The environment dimensions were increased until the difference in eigenvalues was lower than 10^{-4} eV, omitting boundary artifacts on the solution. The energies and the contour of the wave functions cross section along the zx plane were shown in Figure 14.

As discussed in the main article, in ZnSe nanorod couples, the wavefunctions of the lowest electron/hole states reside in the corners and hence occupy the short vertices, while in the hetero- ZnS-ZnSe nanorod couples they reside in the long vertices. In the hetero- ZnS-ZnSe system, in the first 6 states, the hole and electron occupies only ZnSe rod states. Interestingly, despite lying at the edge of the conduction-band offset of ZnSe and ZnS (ZB), the electron also occupies ZnSe rod states, and this is because the first allowed state of the ZnS in the short edges has a much higher energy because of the confinement. However, the electron wavefunction penetrates the ZnS (W) shell quite

significantly. Within the first 6 states, in the ZnSe there are several transitions that are well-defined because of the short/long edges states. In contrary, in the hetero- ZnS-ZnSe system, the states are almost degenerate because they are "rod" states. This difference cannot be distinguished for the ensemble at room temperature but might be visible for single particles.

It should be noted that the model described above produces only a first approximation for the accurate energy values. In order to provide a more detailed picture of the electronic structure, including hole state mixing, electronic fine structure, and dipole moment induced effects, a more complex modeling is required, which is beyond the scope of the calculation described above.

Table 2. Bulk band gap energy and effective masses for ZnSe and ZnS

	ZnSe	ZnS (ZB)	ZnS (W)	Environment
m_e^*	$0.21 m_e$	$0.22 m_e$	$0.22 m_e$	$1 m_e$
m_{hh}^*	$0.67 m_e$	$1.76 m_e$	$1.4 m_e$	$1 m_e$
E_{bg}	2.82 eV	3.78 eV	3.91 eV	4.430 eV
V_e	0	0.51	0.56	0.7965 eV
V_h	0	0.45	0.53	0.7965 eV

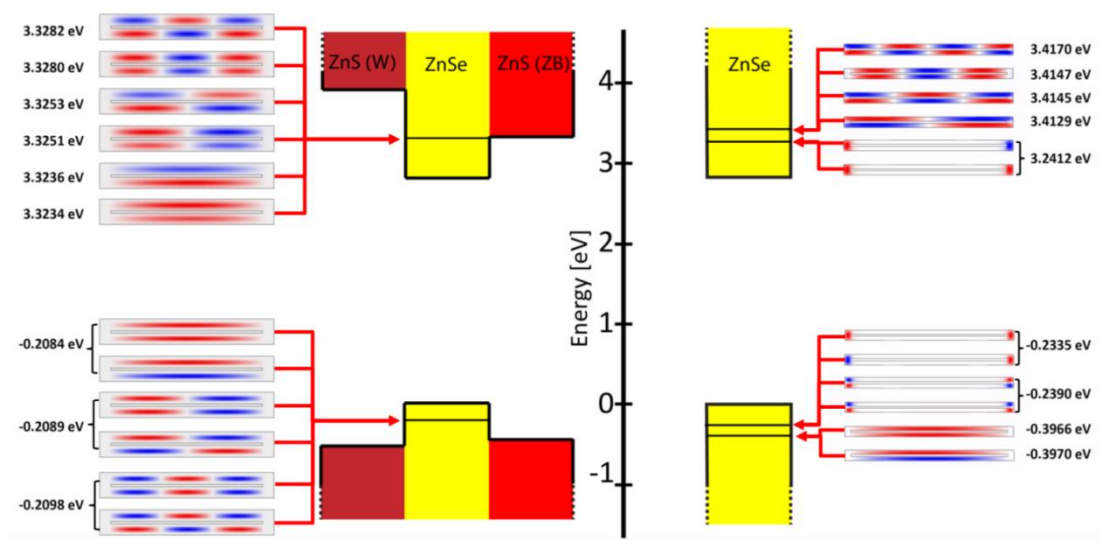


Fig 14. Electronic structures of hetero- ZnS-ZnSe nanorod couples (left panel) compared with homo-ZnSe nanorod couples (right panel). A Zoom-ins on the near band-edge energy levels and envelope wave functions of electron and hole states are depicted in top and bottom panels, respectively. The wave functions are portrayed at the cross-section along the zx plane ($y=0$). White is 0, and red and blue are the + and – phases, respectively. Electron and hole states are presented in different energy scales for clarity.

The transition from homo-ZnSe nanorod couples to hetero- ZnS-ZnSe/ZnS nanorod couples leads to a significant change in the envelope wave functions of the charge carriers and in the energy level structure. A numerical finite-well EMA approach was employed to study the electronic structure of the hetero- ZnS-ZnSe/ZnS nanorod couples (Figure 4, Table 2). In homo-ZnSe nanorod couples, the wave functions of the lowest electron/hole states reside in the corners of the nanorod couples (right panel of Figure 14), while in the hetero- ZnS-ZnSe nanorod couples they reside in

the long vertices (Left panel of Figure 14). From the shape and position of the lowest six electronic and hole states, they can be clearly characterized as ZnSe rod states. However, because the electron states energies reside above the conduction band-offset of ZnSe-ZnS (ZB), the penetration of the electron states into the short edges is slightly more pronounced. Within the first 6 states, in the ZnSe there is a relatively large energy difference between the “corner” states and the long edge states, which is a result of the lower confinement of the charge carriers in the corners of the structure. In contrary, in the hetero-ZnS-ZnSe system, all the states are almost degenerate because they are "rod" states. It is worth noting that the formation of the ZnS shell on the hetero- ZnS-ZnSe nanorod couples further strengthens the confinement of holes into the ZnSe nanorod components of the hetero-nanorod couples, while the electrons leak much more into the ZnS (W) shell, mainly because of the lower effective mass of the electron.

4.3.3 Optical properties of hetero- ZnS-ZnSe/ZnCdS core/shell nanorod couples

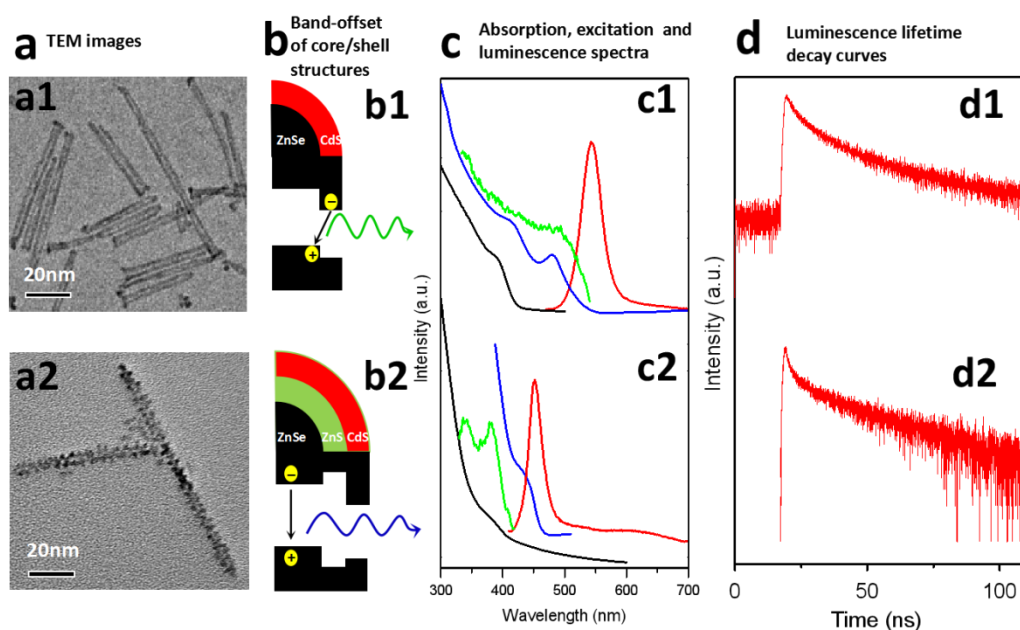


Fig 15. (a) TEM images. (b) Band-offset of core/shell structures. (c) Optical spectra (Black lines are the original core absorption; Green lines are PLE of core/shell structures; Blue lines are absorption of core/shell structures; Red lines are emission of core/shell structures. (d) Fluorescence lifetime decay curves at room temperature. (a1-d1) Homo- ZnSe nanorod couples. (a2-d2) Branched hetero- ZnS (short arm)-ZnSe (long arm)/ZnCdS core/shell/shell nanorod couples.

The above EMA simulations show that the electronic structures of the hetero- ZnS-ZnSe core/shell nanorod couples should present a distinct change in the luminescence characteristics in comparison to those of the homo-ZnSe nanorod couples (Figure 14). In order to eliminate surface traps and to increase the quantum efficiency, a CdS layer was grown on the nanorod couples, generating hetero-ZnS-ZnSe/ZnCdS core/shell nanorod couples. TEM measurements confirmed the obtained homo-ZnSe/CdS (Figure 15a1) and hetero-ZnS-ZnSe/ZnCdS core/shell nanorod couples (Figure 15a2) retain the distinct features of the original particles (Figures 16a and 17a). Statistical analysis on the nanoparticles before and after the CdS shell growth shows that 1-4 monolayers of CdS were grown (Figures 16b and 17b). As depicted in Figure 15b1, ZnSe/CdS nanorod couples constitute core/shell structures with a type II configuration, and therefore, a significant red shift of the band gap with respect to the original ZnSe is expected. The excitation spectra are broader (green curves in Figure 15c1) and resemble the respective absorption spectrum. The corresponding Stokes shift is large (62 nm) with respect to that of CdS rods (~4-10 nm, Figure 18), in consistence with previous results reported in the literature.⁵²⁻⁵⁴

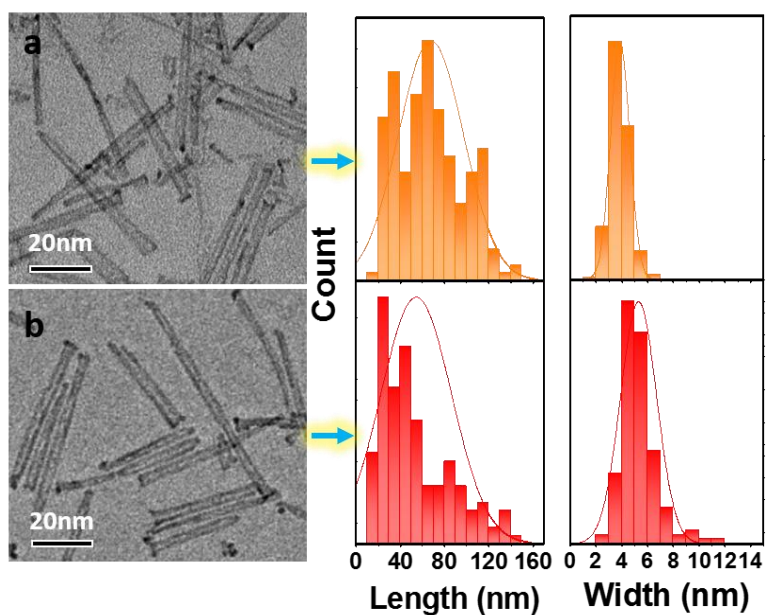


Figure 16. Sizing histograms of a) the original ZnSe nanorod couples before (top panel) (length 65.55 ± 25.40 nm \times width 6.36 ± 1.54 nm) and b) after CdS shell growth (bottom panel) (length 51.90 ± 19.30 nm \times width 7.55 ± 1.42 nm).

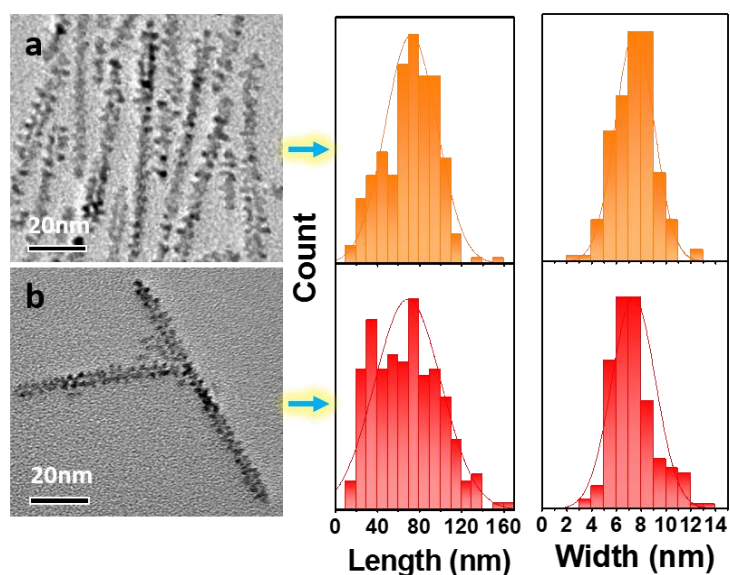


Figure 17. Sizing histograms of a) the original branched hetero- ZnS-ZnSe/ZnS nanorod couples before (top panel) (length 88.58 ± 26.93 nm \times width 7.47 ± 1.55 nm)

and b) after CdS shell growth (bottom panel) (length 83.51 ± 28.50 nm \times width 7.51 ± 2.71 nm).

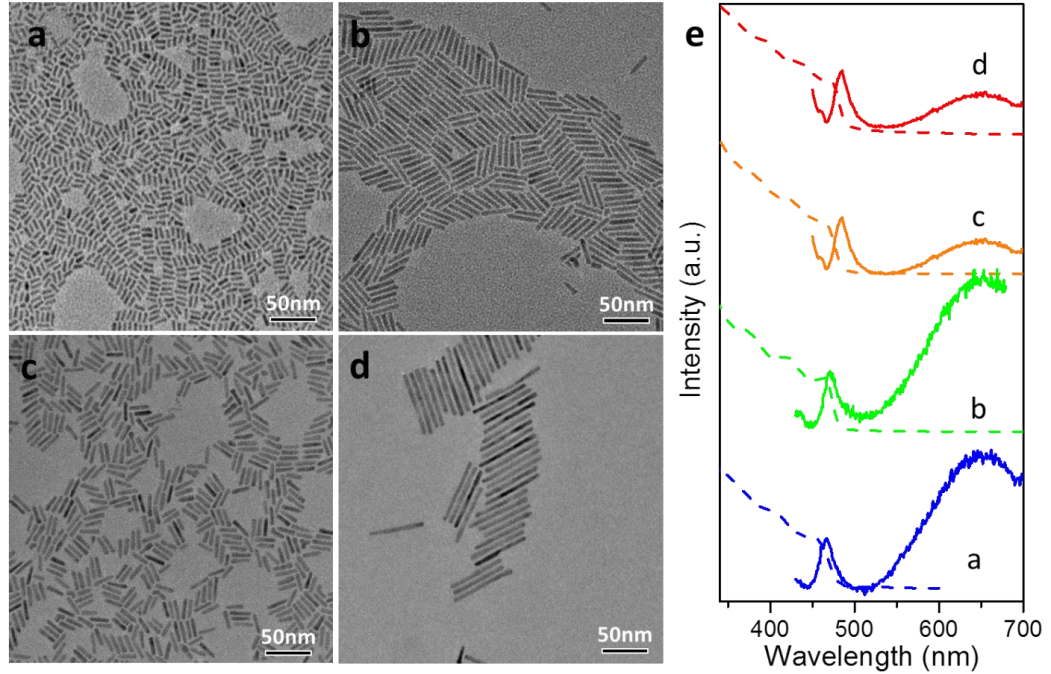


Figure 18. TEM images of CdS nanorods synthesized in TOP/TOPO using hexylphosphonic acid as the surfactant. (a-d) TEM images of CdS nanorods. (a) 3.8 nm (width) \times 11 nm (length). (b) 4.5 nm (width) \times 32 nm (length). (c) 5.5 nm (width) \times 23 nm (length). (d) 4.7 nm (width) \times 72 nm (length). (e) Absorption (dashed line) and luminescence (solid line) of CdS nanorods.

To further elucidate the origin of the blue emission of hetero- ZnS-ZnSe/ZnS/CdS core/shell/shell nanorods couples, a control experiment for the synthesis of CdS nanorods was conducted using similar synthetic conditions as those for the CdS shell growth on the ZnSe nanoparticle. All obtained CdS nanorods show a very weak band edge emission in the range of 460 nm to 476 nm (Fig 18) and a broad band trap state

emission at longer wavelengths with the luminescence quantum efficiency less than 0.1%.

In contrast, the band structure of hetero- ZnS-ZnSe/ZnS core/shell nanorod couples have a quasi-type I configuration because the electron wave functions slightly penetrate the ZnS while the holes are predominantly confined inside the ZnSe nanorod components (Figure 15b2), as predicted by the EMA simulations (Figure 14). The formation of an alloyed layer of ZnCdS on hetero ZnS-ZnSe nanorod couples pushes down the band edge of the conduction band slightly (Figure 15b2). As a result, a small red shift on both absorption and emission spectra in comparison with those of homo- ZnSe/CdS core/shell nanorods couples is expected. As for the hetero- ZnS-ZnSe/ZnCdS core/shell nanorod couples, interestingly, the luminescence excitation spectrum (green curve in Figure 15c2) matches the absorption spectrum of the original hetero- ZnS-ZnSe/ZnS nanorods couples. The emission of the hetero- ZnS-ZnSe/ZnCdS core/shell nanorod couples falls in the blue range with a peak at 451 nm and the Stokes shift is 10 nm. This shift is much smaller than that of homo- ZnSe/CdS core/shell nanorod couples with a type II configuration (Figure 15c1) and is consistent with the aforementioned band offset analysis. It is worth noting that the strain existing at the interfaces between ZnS and CdS may also lead to a red shift as observed in core/shell nanoparticles.³³

We also compared the luminescence spectra of the nanorods couples before and after CdS shell growth (Figure 19). In this case, luminescence of the original nanorods couples was obtained by performing the surface ligand exchange from oleylamine to trioctylphosphine (TOP). After the CdS shell growth, the shifts of the luminescence peak of the homo- ZnS-ZnSe/CdS nanorod couples (Figure 19a) are 120 nm,

whereas the shift for hetero- ZnS-ZnSe/ZnCdS core/shell nanorod couples (Figure 19b) is 44 nm. The luminescence spectra for all core/shell nanorods couples measured at 77 K exhibit a blue shift compared with those measured at room temperature (Figures 20 and 21), which is consistent with the reduction of thermal smearing.

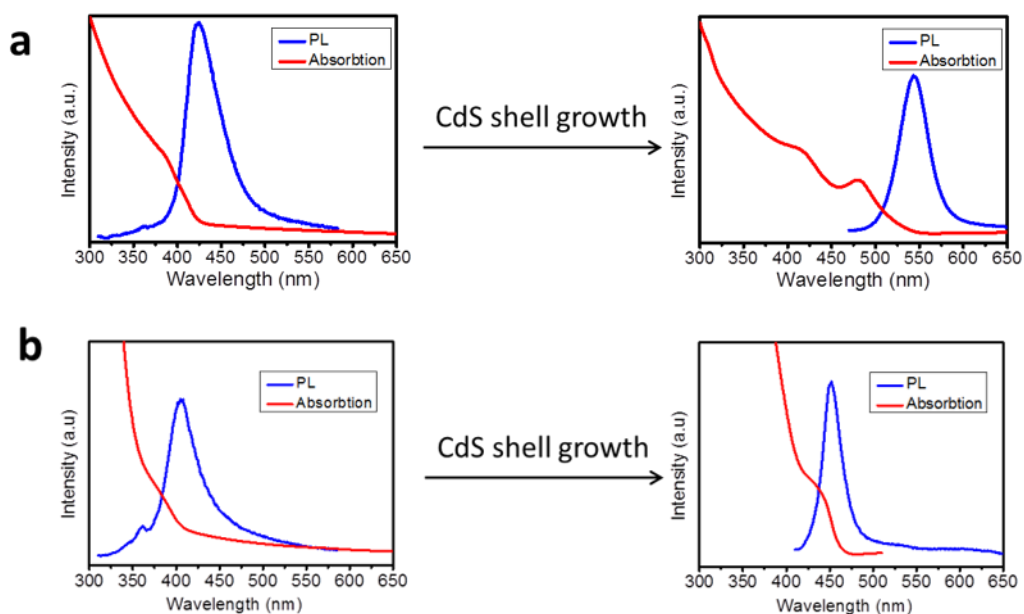


Figure 19. Comparison of absorption and luminescence spectra of nanorod couples before and after CdS shell growth. (a) Homo- ZnSe/CdS core/shell nanorod couples. (b) Hetero- ZnS-ZnSe/ZnCdS core/shell/shell nanorod couples.

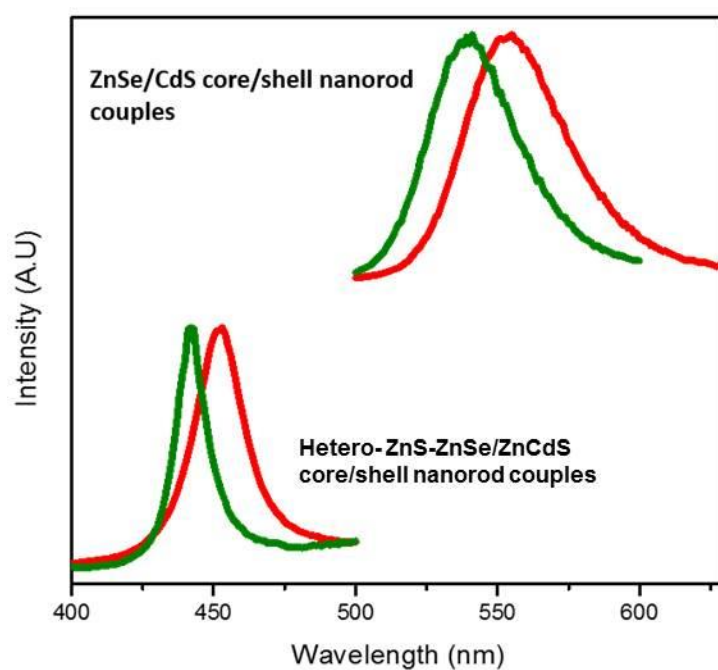


Figure 20. PL spectra of nanorods couples with the CdS shell at room temperature (red curves) and 77K (green curves).

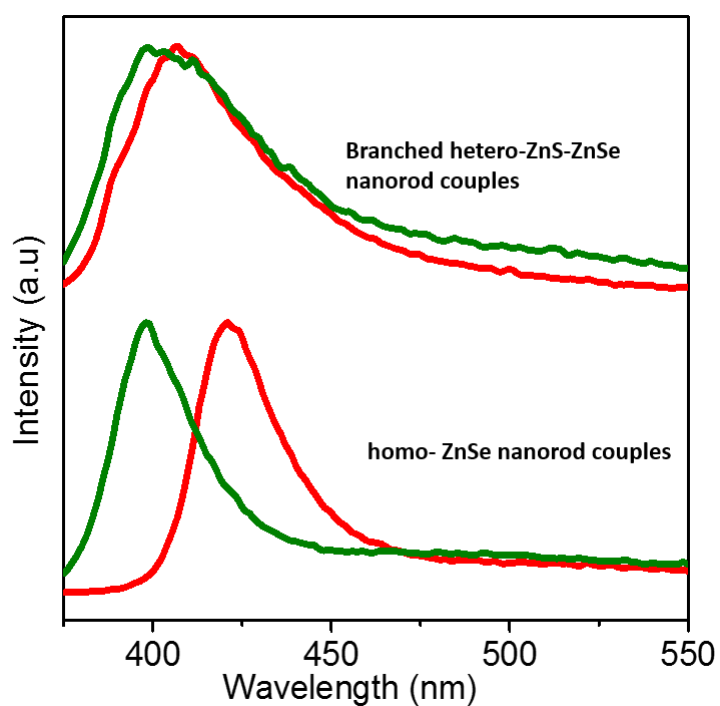


Fig 21. PL spectra of nanorods couples after surface ligand exchange with TOP at room temperature (red curves) and 77K (green curves).

The quantum efficiency of the hetero- ZnS-ZnSe/ZnCdS core/shell nanorod couples is ~2%, which is much lower than those of homo- ZnSe/CdS nanorods couples (15%) (Table 3). This is most likely because forming a perfect CdS shell over the branched ZnS structures in hetero- ZnS-ZnSe/ZnS nanorod couples is hard to achieve, and defects, which act as trap states for the electrons and holes are not diminished. Fluorescence lifetimes of all core/shell nanorod couples at both room temperature and 77 K and were measured and compared in Figures 15d and 22. The time-resolved fluorescent decay curves were fitted by a bi-exponential model $I(t) = A_1[-t/\tau_1] + A_2\exp[-t/\tau_2]$. For hetero ZnS-ZnSe/ZnCdS nanorod couples, $\tau_1 = 6.0$ ns and $\tau_2 = 45.3$ ns whereas $\tau_1 = 10.3$ ns and $\tau_2 = 50.5$ ns for homo- ZnSe/CdS nanorods couples at room temperature (Table 3). The fluorescent lifetimes are much shorter at 77 K (Figure 22) compared those at room temperature as the possibility for non-radiative transition is significantly reduced at low temperature. Although the hetero- ZnS-ZnSe/ZnCdS core/shell nanorod couples show a much lower quantum efficiency than homo- ZnSe/CdS nanorods couples, the luminescence and luminescence excitation spectra of the former provide sufficient information to reveal the distinct change in the luminescence characteristics between hetero- and homo- nanorod couples.

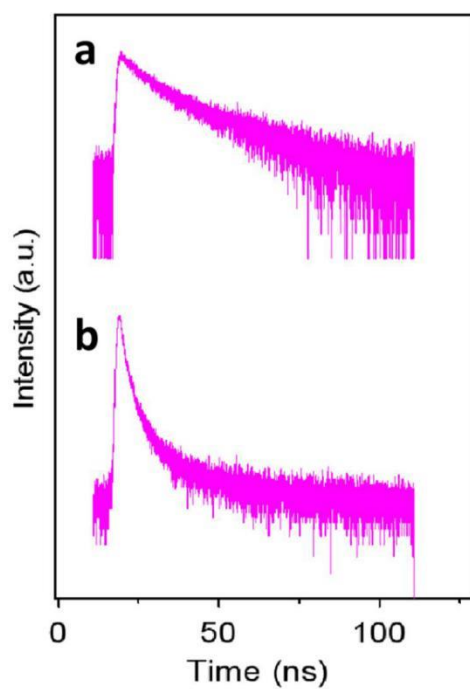


Figure 22. Comparison of 77 K fluorescence lifetime decay curves of hetero-ZnS-ZnSe/ZnCdS and homo- ZnSe/CdS core/shell nanorod couples.

Table 3. Comparison of optical properties of core/shell nanorod couples.

With CdS Shell	Emission	τ_1 (ns)	τ_2 (ns)	τ_1 percentage	Quantum Yields
	(nm)				(%)
Hetero- nanorod couples (RT)	453	6.0	45.3	8%	2.3
Hetero- nanorod couples (77K)	442	2.5	12.1	46%	-
Homo- nanorod	554	10.3	50.5	20%	15.4

couples (RT)

Homo- nanorod	540	7.3	32.4	18%	-
---------------	-----	-----	------	-----	---

couples (77K)

We further expanded this distinct hetero- nanorod couples into other compositions by a cation exchange reaction (Figure 23a).⁵⁵⁻⁵⁷ We specifically targeted lead ions (Pb²⁺) since it is most likely to observe the electronic coupling effect between two closely spaced PbSe rods within a hetero- PbS (short arms)-PbSe (long arms) nanorod couple. This is because the wavefunctions of electrons and holes in PbSe are more delocalized considering its larger exciton Bohr radii (46 nm)⁵⁸ in comparison with the small Bohr exciton radius of ZnSe (4.5 nm).⁵⁹ TEM (Figure 23b, 23c) and HAADF-STEM (Figure 23d, 23e) imaging confirmed that the produced nanoparticles maintained the original features of the branched hetero- nanorod couples. STEM-EDX maps confirmed the alternation of the composition of the hetero- nanorod couples (Figure 24). FFT analysis of the selected area in the HRTEM image (Figure 23c) and XRD patterns corroborate the rock-salt structure of the crystal lattice of the obtained nanoparticles (Figure 23g). The absorption features at longer wavelength (2 in Figure 23f) are consistent with the small band gap of PbS-PbSe. The hetero- PbSe-PbS/PbS nanorod couples do not show any detectable PL as the emission intensity in the near-infrared spectral range may be too weak to be detected. The structural analysis and EDX measurement confirm the successful expansion of hetero- PbS-PbSe nanorod couples via a cation exchange reaction,

which provides an ideal platform to study the electronic coupling effects between closely spaced nanorods. Further experiments in this area are in progress.

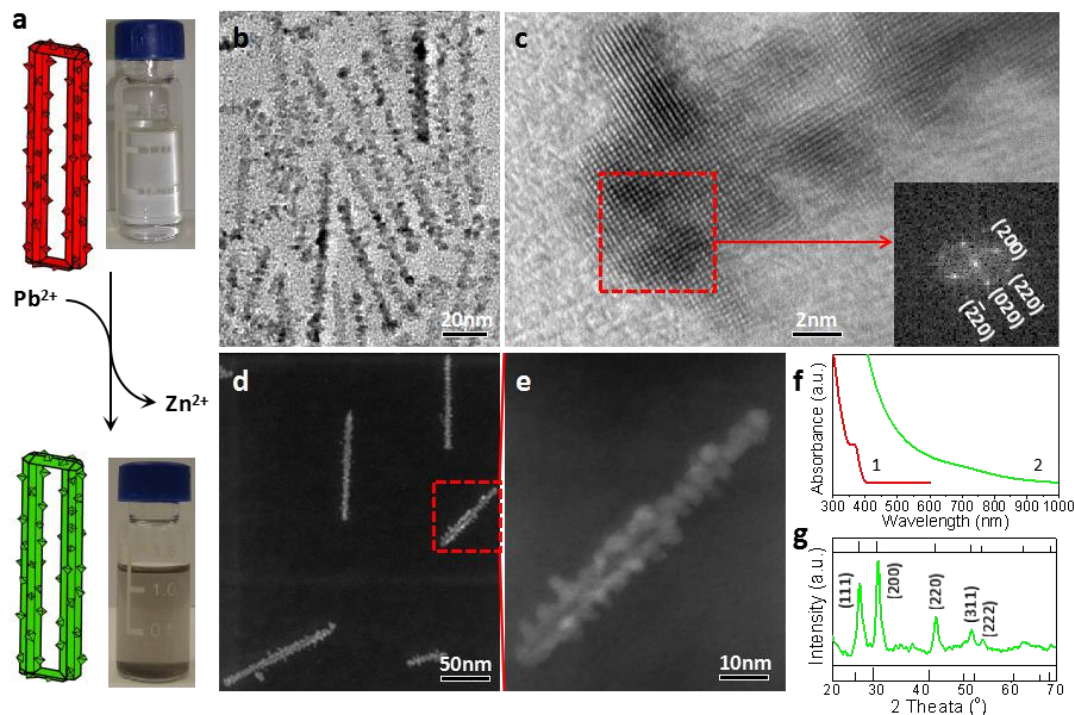


Figure 23. Branched hetero- PbS-PbSe/PbS nanorod couples obtained by a cation exchange reaction. (a) Schematic illustration of branched hetero- PbS-PbSe nanorod couples generated through Zn^{2+} replacement by Pb^{2+} . Band gap tuning is visualized by the color change of nanoparticle solutions before and after the cation exchange. (b) TEM image (c) HRTEM image. Inset in (c) shows the FFT of a selected area labelled by a red rectangle. (d,e) HAADF-STEM images of branched hetero- PbS-PbSe nanorod couples. (f) Comparison of optical absorption spectra of the branched hetero- PbS-PbSe nanorod couples before and after the cation exchange. (g) XRD patterns of branched hetero- PbS-PbSe nanorod couples. The standard XRD patterns for PbSe (bottom) and PbS (top) are given for reference.

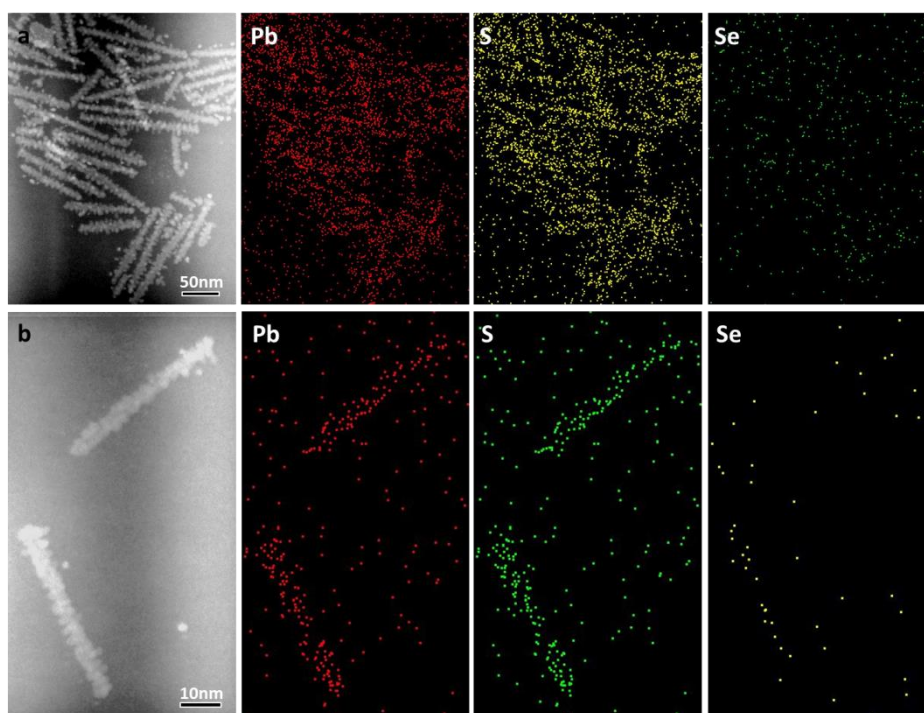


Figure 24. HAADF-STEM images and element maps of branched hetero- PbS-PbSe/PbS core/shell nanorod couples obtained after the cation exchange reaction. (a) Hetero- PbS-PbSe/PbS core/shell nanorod couples with a large population. (b) Two individual hetero- PbS-PbSe/PbS core/shell nanorod couples.

4.4 Conclusions

In conclusion, we have demonstrated a facile wet-chemical approach for the synthesis of hetero- ZnS-ZnSe nanorod couples with ZnS precisely grown on the end facets of two parallelly aligned ZnSe nanorods. Due to the small contact area between ZnSe and ZnS at the apexes of ZnSe nanorods, the growth of zinc blende ZnS on ZnSe nanorods may still be epitaxial. The hetero- ZnS-ZnSe/ZnCdS core/shell nanorod couples show a blue emission due to the distinct quantum

confinement regime within these unique heterostructures in comparison with the green emission from homo- core/shell nanorod couples. Further expanding the hetero- nanorod couples produced hetero- PbS-PbSe/PbS nanorod couples. The synthetic strategy developed here may provide new insight into the rational design and synthesis of new heterostructures with increasing complexity, and the heterostructures obtained here may facilitate the incorporation of such materials into optoelectronic and catalytic applications.

4.5 References

- [1] R. Costi, A. E. Saunders, U. Banin, *Angew. Chem. Int. Ed.* **2010**, *49*, 4878.
- [2] G. Jia, Y. Pang, J. Ning, U. Banin, B. Ji, *Adv. Mater.* **2019**, *31*, 1900781.
- [3] K. Wu, J. Chen, J. R. McBride, T. Lian, *Science* **2015**, *349*, 632.
- [4] Li, Z. Wei, T. Wu, Q. Peng, Y. Li, *J. Am. Chem. Soc.* **2011**, *133*, 5660.
- [5] R. D. Robinson, B. Sadtler, D. O. Demchenko, C. K. Erdonmez, L.-W. Wang, A. P. Alivisatos, *Science* **2007**, *317*, 355.
- [6] U. Banin, Y. Ben-Shahar and K. Vinokurov, *Chem. Mater.* **2014**, *26*, 97.
- [7] A. Vaneski, A. S. Susha, J. Rodríguez-Fernández, M. Berr, F. Jäckel, J. Feldmann, A. L. Rogach, *Adv. Funct. Mater.* **2011**, *21*, 1547.
- [8] Y. Shemesh, J. E. Macdonald, G. Menagen, U. Banin, *Angew. Chem. Int. Ed.* **2011**, *123*, 1217.
- [9] T. Simon, Bouchonville, N.; M. J. Berr, A. Vaneski, A. Adrovic, D. Volbers, R. Wyrwich, M. Döblinger, A. S. Susha, A. L. Rogach, F. Jäckel, J. K.

- Stolarczyk, J. Feldmann, *Nat. Mater.* **2014**, *13*, 1013.
- [10] S. M. Kim, S. J. Lee, S. H. Kim, S. Kwon, K. J. Yee, H. Song, G. A. Somorjai, J. Y. Park, *Nano Lett.* **2013**, *13*, 1352.
- [11] N. Oh, B. H. Kim, S.-Y. Cho, S. Nam, S. P. Rogers, Y. Jiang, J. C. Flanagan, Y. Zhai, J.-H. Kim, J. Lee, Y. Yu, Y. K. Cho, G. Hur, J. Zhang, P. Trefonas, J. A. Rogers, M. Shim, *Science* **2017**, *355*, 616.
- [12] R. Lavieville, Y. Zhang, A. Casu, A. Genovese, L. Manna, E. Di Fabrizio, R. Krahne, *ACS Nano* **2012**, *6*, 2940.
- [13] S.-H. Choi, H. B. Na, Y. I. Park, K. An, S. G. Kwon, Y. Jang, M.-H. Park, J. Moon, J. S. Son, I. C. Song, W. K. Moon, T. Hyeon, *J. Am. Chem. Soc.* **2008**, *130*, 15573.
- [14] C. Xu, J. Xie, D. Ho, C. Wang, N. Kohler, E. G. Walsh, J. R. Morgan, Y. E. Chin, S. Sun, *Angew. Chem. Int. Ed.* **2008**, *47*, 173.
- [15] C. Xu, B. Wang, S. Sun, *J. Am. Chem. Soc.* **2009**, *131*, 4216.
- [16] J.-S. Choi, Y.-W. Jun, S.-I. Yeon, H. C. Kim, J.-S. Shin, J. Cheon, *J. Am. Chem. Soc.* **2006**, *128*, 15982.
- [17] D. V. Talapin, J. S. Lee, M. V. Kovalenko and E. V. Shevchenko, *Chem. Rev.* **2010**, *110*, 389.
- [18] R. E. Schaak, M. E. Williams, *ACS Nano* **2012**, *6*, 8492.
- [19] L. Carbone, C. Nobile, M. De Giorgi, F. Della Sala, G. Morello, P. Pompa, M. Hytch, E. Snoeck, A. Fiore, I. R. Franchini, M. Nadasan, A. F. Silvestre, L. Chiodo, S. Kudera, R. Cingolani, R. Krahne, L. Manna, *Nano Lett.* **2007**, *7*,

2942.

- [20] T. Wang, J. Zhuang, J. Lynch, O. Chen, Z. Wang, X. Wang, D. LaMontagne, H. Wu, Z. Wang, Y. C. Cao, *Science* **2012**, 338, 358.
- [21] Y. Ben-Shahar, F. Scotognella, I. Kriegel, L. Moretti, G. Cerullo, E. Rabani, U. Banin, *Nat. Commun.* **2016**, 7, 10413.
- [22] N. J. Borys, M. J. Walter, J. Huang, D. V. Talapin, J. M. Lupton, *Science* **2010**, 330, 1371.
- [23] J. Dimitrijevic, L. Krapf, C. Wolter, C. Schmidtke, J.-P. Merkl, T. Jochum, A. Kornowski, A. Schüth, A. Gebert, G. Hüttmann, T. Vossmeier and H. Weller, *Nanoscale* **2014**, 6, 10413.
- [24] H. Li, R. Brescia, R. Krahne, G. Bertoni, M. J. P. Alcocer, C. D'Andrea, F. Scotognella, F. Tassone, M. Zanella, M. De Giorgi, L. Manna, *ACS Nano* **2012**, 6, 1637.
- [25] L. Carbone, C. Nobile, M. De Giorgi, F. Della Sala, G. Morello, P. Pompa, M. Hytch, E. Snoeck, A. Fiore, I. R. Franchini, M. Nadasan, A. F. Silvestre, L. Chiodo, S. Kudera, R. Cingolani, R. Krahne, L. Manna, *Nano Lett.* **2007**, 7, 2942.
- [26] G. Jia, U. Banin, *J. Am. Chem. Soc.* **2014**, 136, 11121.
- [27] G. Jia, A. Sitt, G. B. Hitin, I. Hadar, Y. Bekenstein, Y. Amit, I. Popov, U. Banin, *Nat. Mater.* **2014**, 13, 301.
- [28] B. O. Dabbousi, J. Rodriguez Viejo, F. V. Mikulec, J. R. Heine, H. Mattoussi, R. Ober, K. F. Jensen, M. G. Bawendi, *J. Phys. Chem. B* **1997**, 110, 9463.

- [29] X. Peng, M. C. Schlamp, A. V. Kadavanich, A. P. Alivisatos, *J. Am. Chem. Soc.* **1997**, *119*, 7019.
- [30] B. Ji, Y. E. Panfil, N. Waiskopf, S. Remennik, I. Popov, U. Banin, *Nat. Commun.* **2019**, *10*, 2.
- [31] M. Lomascolo, A. Cretì, G. Leo, L. Vasanelli, L. Manna, *Appl. Phys. Lett.* **2003**, *82*, 418.
- [32] D. Chen, H. Zhang, Y. Li, Y. Pang, Z. Yin, H. Sun, L.-C. Zhang, S. Wang, M. Saunders, E. Barker, G. Jia, *Adv. Mater.* **2018**, *30*, 1803351.
- [33] A. M. Smith, A. M. Mohs, S. Nie, *Nat. Nanotechnol.* **2009**, *4*, 56.
- [34] C.-M. Ning, L. Dou, P. Yang, *Nat. Rev. Mater.* **2017**, *2*, 17070.
- [35] T. Mokari, U. Banin, *Chem. Mater.* **2003**, *15*, 3955.
- [36] H. Zhong, T. Mirkovic and G. D. Scholes, Comprehensive Nanoscience and Technology Vol. 5: Nanocrystal Synthesis, (Eds: D. Andrews, G. Scholes, G. Wiederrecht), Elsevier **2010**, 153.
- [37] C.-M. Ning, L. Dou, P. Yang, *Nat. Rev. Mater.* **2017**, *2*, 17070.
- [38] C. Tan, J. Chen, X.J. Wu, H. Zhang, *Nat. Rev. Mater.* **2018**, *3*, 17089.
- [39] N. Oh, M. Shim, *J. Am. Chem. Soc.* **2016**, *138*, 10444.
- [40] C.-Y. Yeh, Z. W. Lu, S. Froyen, A. Zunger, *Phys. Rev. B* **1992**, *46*, 10085.
- [41] T. Omata, H. Uesugi, M. Kita, *J. Cryst. Growth* **1994**, *394*, 81.
- [42] P. D. Cozzoli, L. Manna, M. L. Curri, S. Kudera, C. Giannini, M. Striccoli, A. Agostiano, *Chem. Mater.* **2005**, *17*, 1296.

- [43] W. Chen, A. Karton, T. Hussian, S. Javaid, F. Wang, Y. Pang, G. Jia, *CrystEngComm* **2019**, *21*, 2955.
- [44] G. Pellegrini, G. Mattei, P. Mazzoldi, *J. Appl. Phys.* **2005**, *97*, 073706.
- [45] T. Omata, K. Nose, S. Otsuka-Yao-Matsuo, *J. Appl. Phys.* **2009**, *105*, 073106.
- [46] H. Landolt, R. Börnste, Landolt-Börnstein: Numerical Data and Functional Relationships in Science and Technology, O. Madelung, U. Rössler, M. Schulz, Ed. group III, vol. 41B (Springer, Berlin, **1982**)
- [47] Landolt-Börnstein: Numerical Data and Functional Relationships in Science and Technology, New Series (Ed: K. H. Hellwege), Springer, Berlin **1983**.
- [48] M. Cardona, *J. Phys. Chem. Solid.* **1963**, *24*, 1543.
- [49] S.H. Wei, A. Zunger, *Appl. Phys. Lett.* **1998**, *72*, 2011.
- [50] H. E. Ruda, *J. Appl. Phys.* **1986**, *59*, 3516.
- [51] M. Murayama, T. Nakayama, *Phys. Rev. B* **1994**, *49*, 4710.
- [52] K. Boldt, C. Ramanan, A. Chanaewa, M. Werheid, A. Eychmüller, *J. Phys. Chem. Lett.* **2015**, *6*, 2590.
- [53] K. Boldt, K. N. Schwarz, N. Kirkwood, T. A. Smith, P. Mulvaney, *J. Phys. Chem. C* **2014**, *118*, 13276.
- [54] D. Dorfs, A. Salant, I. Popov, U. Banin, *Small* **2008**, *4*, 1319.
- [55] D. H. Son, S. M. Hughes, Y. Yin, A. P. Alivisatos, *Science* **2004**, *306*, 1009.
- [56] W. Li, R. Zamani, M. Ibáñez, D. Cadavid, A. Shavel, J. R. Morante, J. Arbiol, A. Cabot, *J. Am. Chem. Soc.* **2013**, *135*, 4664.

- [57] L. De Trizio, L. Manna, *Chem. Rev.* **2016**, *116*, 10852.
- [58] H. Du, C. Chen, R. Krishnan, T. D. Krauss, J. M. Harbold, F. W. Wise, M. G. Thomas, J. Silcox, *Nano Lett.* **2002**, *2*, 1321.
- [59] V. V. Rossin, T. Böttger, F. Henneberger, *Phys. Rev. B* **1996**, *54*, 7682.

Chapter 5. Type-II ZnSe (Rod)/CdS (Rod) Core/Shell Quantum Rods with Green Fluorescence

(Chapter 5 was submitted to a peer-reviewing journal.)

5.1 Abstract

Quasi-one dimensional type-II core/shell structures are of highly importance due to their efficient charge separation and transport. Here, we present the synthesis of type-II ZnSe (rod)/CdS (rod) core/shell nanorods through a colloidal seeded-growth method. ZnSe /CdS core/shell nanorods show green fluorescence centered at 540 nm with a luminescence quantum yield of 26%, with relevance to applications in green-emitting polarized quantum light emitting diodes.

5.2 Introduction

Colloidal type-II core/shell semiconductor nanocrystals have staggered band alignments because either holes or electrons of the charge carriers are partially confined in the core. Therefore the luminescence spectra of semiconductor nanocrystals with such a configuration show a larger red shift and a longer luminescent lifetimes in comparison with those of type-I core/shell semiconductor nanocrystals wherein both electrons and holes of charge carriers are confined in the core materials. The strong local electric field associated with multiexciton behavior and optical-gain enhancement of type-II core/shell semiconductor nanocrystals

reduce the lasing threshold and enhance the electron extraction efficiency.^{1,2} Current colloidal synthesis strategies enable precisely control the size, shape and aspect ratio of quasi-one dimensional semiconductor quantum rods.³ Comparing with spherical semiconductor quantum dots, quasi-one dimensional quantum rods have a large absorption cross section, longer bi-exciton lifetime and linearly polarized absorption and emission,^{4,5} making them more advantageous in many applications such as lasers,⁶ optoelectronics⁷ and bioimaging⁸.

The seeded-growth method is a powerful approach for the preparation of quasi-one dimensional core/shell structures. It involves the hot injection of shell precursors of appropriate reactivity and nanocrystal seeds into the reaction solutions in the presence of organic surfactants.⁹ Minimizing the lattice mismatch between core and shell materials are crucial to tailor the CdS nanorod shell growth. The crystal structure of core can also make differences on the final morphology of the core/shell structures. For examples, CdS shell growth on wurtzite CdSe core led to core/shell nanorod while CdS nanotetrapods were obtained when zinc blende CdSe cores were used.^{3,10}

Quasi-one dimensional type-II core/shell structures were less reported.^{11,12} Zamkov et al reported the ZnSe (dots)/CdS (dots) core shell quantum dots with a luminescence quantum yield of up to 20%.¹³ Afterwards, Banin et al presented the ZnSe (dot)/CdS (rod) core/shell quantum rods with cubic ZnSe as the core materials.¹⁴ However, the ZnSe (rod)/CdS (rod) core/shell quantum rods have not been investigated so far and further studies on their electronic structures and luminescence dynamics are highly demanded. Meanwhile, various novel properties have been revealed in case studies on zinc chalcogenide based quantum rods

heterostructures such as red-shifted emission ZnSe tipped ZnTe nanorods,¹⁵ enhanced photocatalytic alloyed ZnS_xSe_{1-x} nanorods,¹⁶ low photoluminescence polarization anisotropy of ZnSe nanorod couples,¹⁷ and blue fluorescent hetero-ZnS (short arms)-ZnSe (long arms)/ZnS shell nanorod couples.¹⁸ In-depth understanding the distributions of the wavefunctions of electron and hole are important in exploring electronic coupling effects associating with the structure which can finally benefit to their applications.¹⁸

5.3 Experimental Section

Chemicals: Zn(NO₃)₂·6H₂O (99%), selenium powder (99.999%), sulfur powder (99%), oleylamine (approximate C₁₈ content 80–90%), CdO (99%), trioctylphosphine (TOP, 97%), trioctylphosphine oxide (TOPO, 90%), Poly(vinyl butyral-co-vinyl alcohol-co-vinyl acetate) (average M_w 50000-80000), toluene (99.8%, anhydrous), and methanol (99.8% anhydrous) were purchased from Sigma-Aldrich. Octadecylphosphonic acid (ODPA) and hexylphosphonic acid (HPA) were purchased from PCI Synthesis. All chemicals were used as received without further purification.

Synthesis of ZnSe (rod)/CdS (rod) core/shell nanorods: Thin ZnSe nanorods synthesis was synthesized and controlled according to a previously reported approach.^{16,19} For the CdS shell growth, a modified seeded-growth method were used.⁹ Typically, CdO (15 mg), trioctylphosphine oxide (2.0 g), octadecylphosphonic acid (75 mg) and hexylphosphonic acid (10 mg) were mixed and heated to 150 °C for 0.5 h under vacuum and then rise to 320 °C at N₂ to form a colourless solution.

Then, a stock solution dissolved of 3 ml TOP solution dissolved with 1×10^{-9} mol thin ZnSe nanorods and 30 mg sulfur was swiftly injected into the reaction at 365 °C. After corresponding time, the reaction was quenched by ice bathing. The crude reaction solution was diluted with toluene, methanol was added to precipitate the nanocrystals and remove excess surfactants.

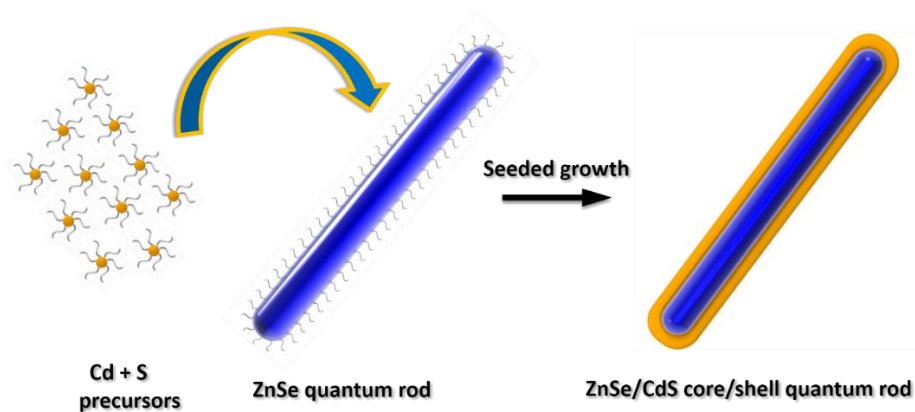
Synthesis of ZnSe (rod)/CdS (rod) core/shell nanorods film: Poly(vinyl butyral-co-vinyl alcohol-co-vinyl acetate) was firstly dissolved by toluene to obtain a uniform solution. Then, the ZnSe (rod)/CdS (rod) core/shell nanorods (5 wt % of Poly(vinyl butyral-co-vinyl alcohol-co-vinyl acetate)) were dissolved in toluene as well. After that, the two solutions were mixed to form homogeneous solution. The homogeneous solution was heat at 60 °C for two days and toluene was fully evaporated to form the QD-polymer film.

Sample Characterization.

UV-vis absorption spectroscopy was performed on a Perkin Elmer Lambda 35 UV/VIS. Photoluminescence spectra were recorded using a Cary Eclipse luminescence spectrophotometer. *XRD Measurement:* XRD patterns were obtained using Cu K α ($\lambda=1.5406$ Å) photons from an X'per PRO (PANalytical) X-ray diffractometer operated at 40 kV and 40 mA. TEM was performed using a JEOL 2100 transmission electron microscope with a tungsten filament running at an accelerating voltage of 120 keV. High angle annular dark field-scanning transmission electron microscopy (HAADF-STEM) was performed on an FEI Titan G2 80-200 high-resolution transmission electron microscope.

5.4 Results and discussion

Here, we present the synthesis of green fluorescent ZnSe (rod)/CdS (rod) core/shell quantum rods through a seed-growth method (Scheme 1). The initial ZnSe quantum rods were synthesized by injection of Se-oleylamine (OLA) stock solution into Zn-oleylamine solution according to a method developed by our group.¹⁹ It worth noting that the size distribution of ZnSe quantum rods can be optimized through the ripping process or thiol-etching at elevated temperatures.¹⁶ The obtained ZnSe quantum rods were washed by toluene and precipitated by methanol. The shell growth approach is a typical seed mediated growth mechanism by hot injection. After the injection of the ZnSe quantum rods with sulfur-trioctylphosphine (S-TOP) stock into solution, the emerged CdS trends to grow on the surface of ZnSe quantum rods with the aid of surfactants as octadecylphosphonic acid and hexylphosphonic acid, rather than self-nucleation.⁹ The shell thickness of CdS can be controlled through the reaction time after injecting S precursor into the reaction solution containing ZnSe nanorods and Cd precursor. In the typical synthesis, CdS shell grew very fast in the first 30 seconds after the injection and then the growth rate slowed down due to the decrease of the reacting monomer concentration. After ~3min, almost all the monomers were consumed, which indicates the system reaches a thermodynamic limit. This seeded growth approach for CdS shell growth over ZnSe nanorods can prevent the self-nucleation and benefit the uniform shell formation.^{18,23}



Scheme 1. Illustration of CdS shell growth on the ZnSe quantum rod

The original ZnSe quantum rods were shown in Fig 2a with an average diameter of 4.01 ± 0.90 nm. After shell growth, the core/shell ZnSe/CdS rod is about 4.43 ± 0.77 nm in diameter which corresponds to a 1.2 monolayer (0.42 nm) of CdS shell (Fig 2 b, 2c). High angle annular dark field-scanning transmission electron microscopy (HAADF-STEM) also confirms the uniform size distribution of ZnSe/CdS core/shell quantum rods (Fig 3). Selected area fast Fourier transforms (FFT) of the high-resolution transmission electron microscopy (HRTEM) images can be indexed into wurtzite structures (Fig 2d). Due to the wurtzite ZnSe rods are embedded in the wurtzite CdS shell, the exposed faces are belonging to CdS. The (0 0 2) reflection confirms the growth direction along the c-axis of the wurtzite CdS structure.¹⁶

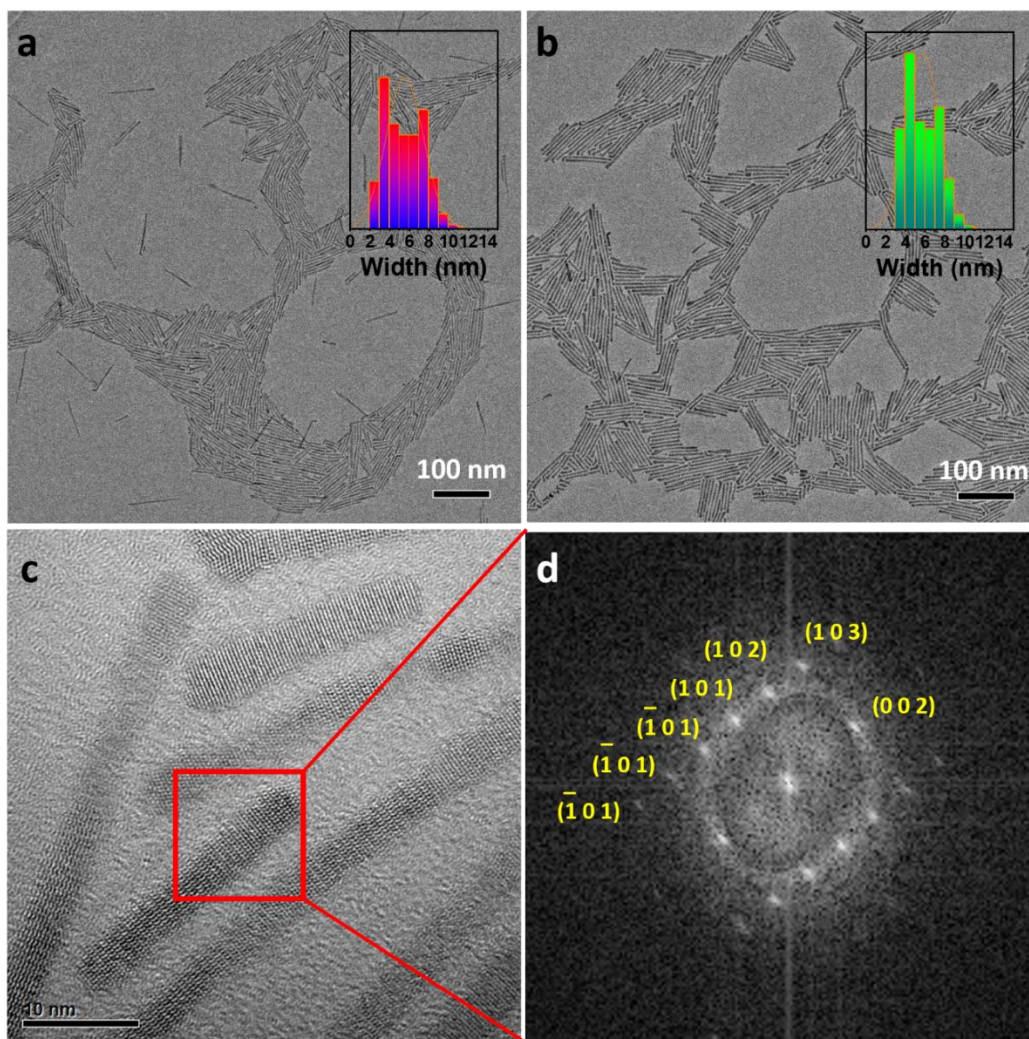


Figure 2. TEM images of ZnSe quantum rods (a) and ZnSe (rod)/CdS (rod) core/shell nanorods (b). The inserts are the statistics of diameter. c) HRTEM images of ZnSe (rod)/CdS (rod) core/shell nanorods. d) The FFT of selected area of ZnSe (rod)/CdS (rod) core/shell nanorods.

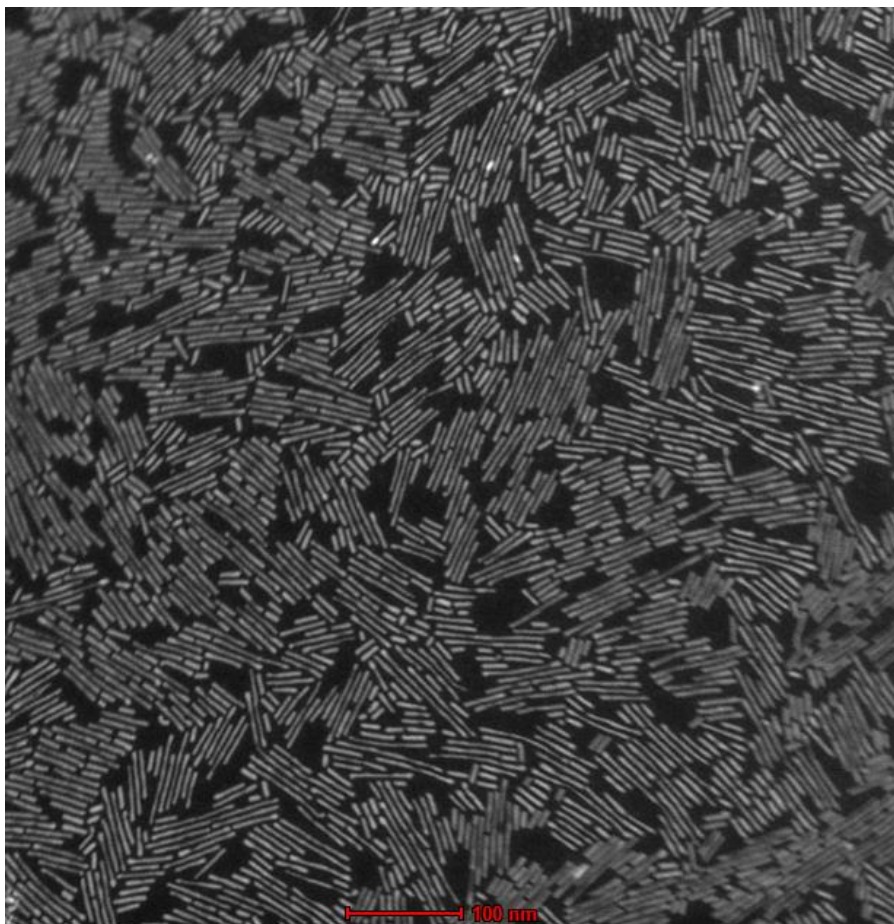


Figure 3. STEM images of ZnSe (rod)/CdS (rod) core/shell nanorods

Being consistent with the FFTs, the powder X-ray diffraction (XRD) pattern presents a strong diffraction peaks corresponding to the (0 0 2) lattice plane of the wurtzite structure in Fig 4. Comparing with the standard JCPDS cards, the XRD pattern of the product displays a typical feature of wurtzite structures, with diffraction peaks being located between those of wurtzite ZnSe and CdS. The shifts of the diffraction peaks confirm the formation of CdS shell on the ZnSe core materials.¹⁴ The results agree with the pervious report of ZnSe (dot)/CdS (rod) core/shell nanorods which have a wurtzite structure CdS shell.¹⁴

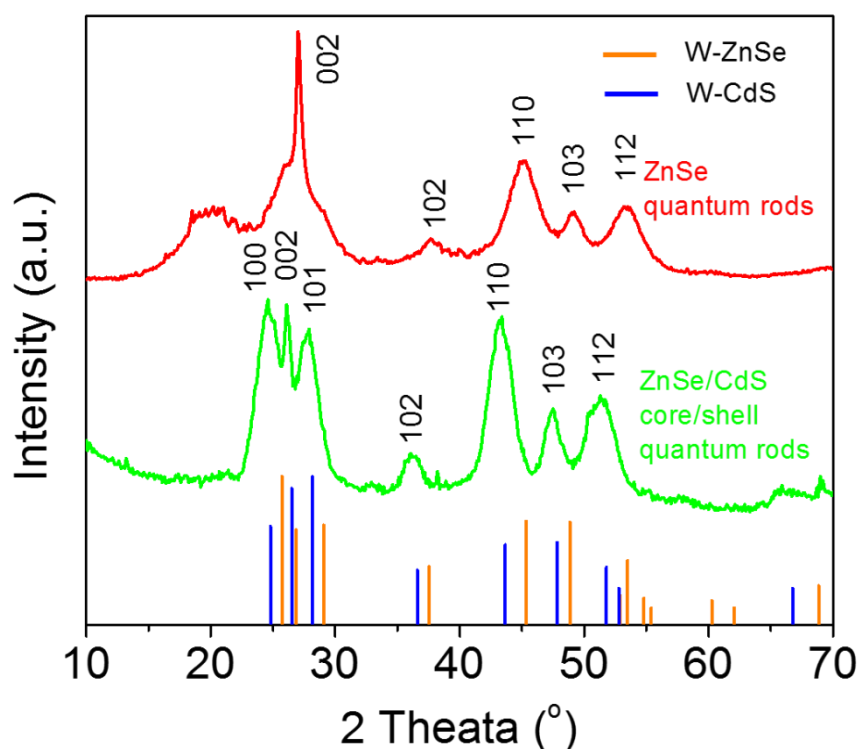


Figure 4. XRD pattern of ZnSe (rod)/CdS (rod) core/shell nanorods (The ZnSe quantum dots XRD pattern was adapted from Ref 16)

In a type-II core/shell structure (Fig 4a), the hole localized in the core of the ZnSe rods with a direct band gap of 2.72 eV and the electron is distributed in the shell of the CdS with a direct band gap of 2.49 eV. The staggered band alignments lead to a reduced band gap of 1.93 eV and a significant red shift of around 100 nm in luminescent emission. As the reaction evolves for from 10 s, 30 s to 2 minutes, the emission shifts from 500 nm to 536 nm and 550 nm respectively (Fig 5b). As shown in Fig 5c, photoluminescence excitation (PLE) spectra show a characteristic feature of ZnSe nanorods, a large stokes shift of around 0.5 eV is observed. Because both the conduction band bottom and valance band top of CdS (shell) are lower than those of ZnSe (core), ZnSe nanorods overcoated with a thin shell of even 0.42 nm constitute

core/shell structures with a type-II configuration.²⁸ Under such a configuration, although the holes are confined in the ZnSe core materials, the electron could easily delocalized to the shell materials of CdS, leading to a large Stokes shift of absorption and emission, and long luminescence lifetime^{13,24} As the reaction evolves for from 10 s, 30 s to 2 minutes, the emission shifts from 500 nm to 536 nm and 550 nm, respectively (Fig 5b). The emission wavelength of ZnSe (rod)/CdS core/shell structures were readily tuned into the green spectral range through changing the thickness of the CdS shell. The shift in ZnSe/CdS core/shell structures is indeed much larger than the type-I CdSe/CdS core/shell structures which have only a small shift of a few nanometers.¹⁴ Compared with ZnSe/CdS core/shell dots, ZnSe (rod)/CdS (rod) core/shell nanorods have a narrower full width at half maximum (FWHM), which is 37 nm.¹³ The luminescence lifetime $t_{1/e}$ of ZnSe/CdS core/shell nanorods is about 52 ns which is much slower than that of the type-I CdSe/CdS core/shell structure (13 ns) due to delocalization of the charge carriers.¹⁴ Meanwhile, the $t_{1/e}$ of ZnSe/CdS core/shell nanorods is faster than ZnSe(dots)/CdS(rod) core/shell quantum rods (105 ns).¹⁴ The rationale here is that because the CdS shell is very thin, the delocalization of electron into the shell is not very far from the core materials of ZnSe nanorods while in the ZnSe dots seeded CdS core/shell nanorods, the electron can delocalize into the rod component, leading to increased luminescence lifetime in ZnSe (dot)/CdS (rod) core/shell nanorods.⁹ Therefore, a long luminescence lifetime can be achieved through a thick shell, as well as observed in the ZnSe (dot)/CdS (rod) core/shell nanorods.¹⁴ Consistently, ZnSe (rod)/CdS (rod) core/shell nanorods with a 1.2 monolayer thick shell show a radiative luminescence lifetime of 32 ns at the room temperature and 29 ns at 77 K (see in Fig 6). In Fig 6a,

the emission measured at 77 K shows a 18 nm blue shift .¹⁸ The 3 ns decrease of decay at 77K is agree with phenomenon of thermal smearing reduction.¹⁸ Furthermore, due to the type-II structure, only holes have been confined in the core, leading to a lower quantum yield of around 26% comparing to a QY of 75% of the type-I CdSe/CdS quantum rods.⁹

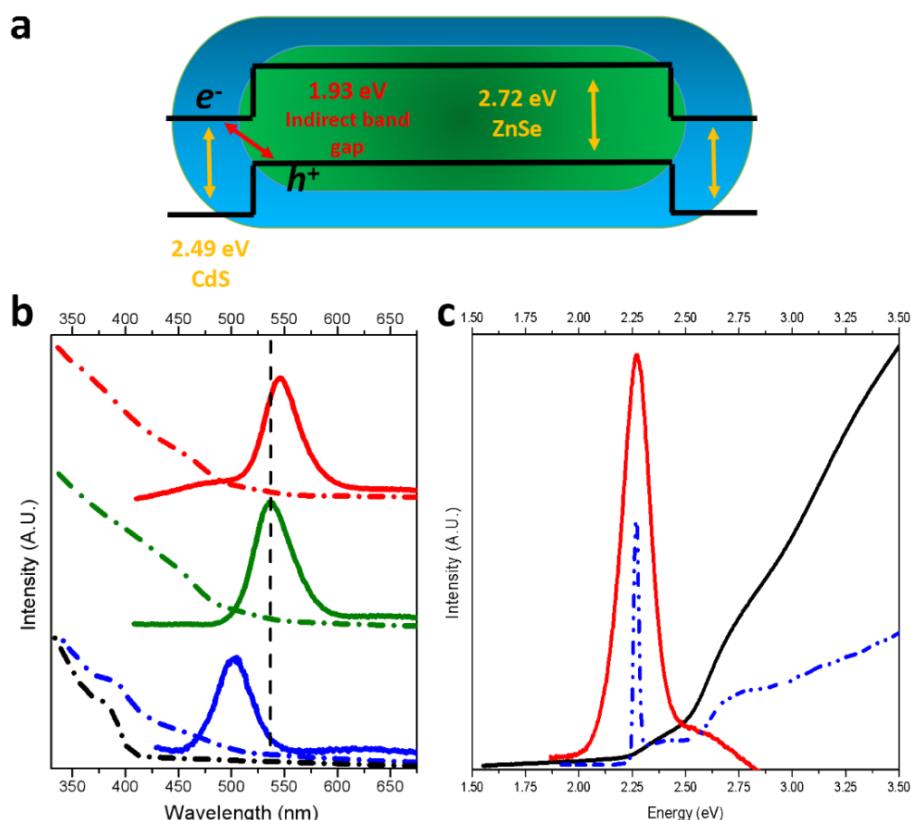


Figure 5. a) Band gap alignment of ZnSe (rod)/CdS (rod) core/shell nanorods. b) absorption (dashed lines) and PL (solid lines) spectra of ZnSe nanorods (black lines), ZnSe (rod)/CdS (rod) core/shell nanorods after injection 10 s (blue lines), 30 s (green lines) and 2 mins (red lines). c) absorption (black lines), PL (red lines) and PLE spectra (blue dashed lines) of ZnSe (rod)/CdS (rod) core/shell nanorods.

Table 1. Comparison of optical properties of ZnSe (rod)/CdS (rod) core/shell nanorods in room temperature and 77K.

Sample	Emission (nm)	τ_1 (ns)	τ_2 (ns)	τ_1 percentage	Quantum Yields (%)
ZnSe (rod)/CdS (rod) core/shell nanorods (Room Temperature)	553	32.95	141.81	38%	25.94
ZnSe (rod)/CdS (rod) core/shell nanorods (77K)	535	29.75	114.89	50%	25.36

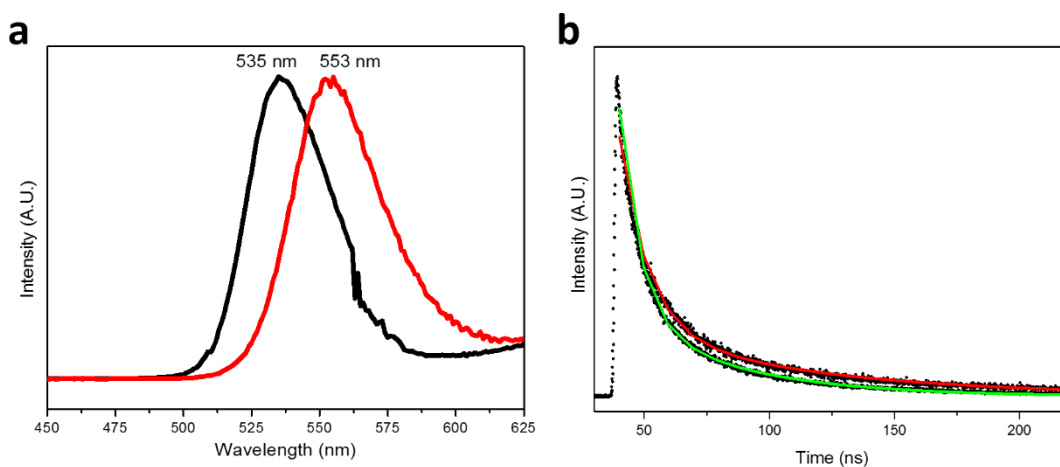


Figure 6. a) PL spectra of ZnSe (rod)/CdS (rod) core/shell nanorods in room temperature (red line) and 77K (black line). b) Decay fitting of ZnSe (rod)/CdS (rod) core/shell nanorods in room temperature (green line) and 77K (red line).

We used a finite well effective mass approximation (EMA) approach to study the electronic structure of the hetero-ZnSe/CdS nanorods, and to compare it to the electronic structure of ZnSe nanorods. In EMA, the confined excited charge carrier is treated as a particle in a box. Under this approximation, the Schrödinger equation for the electron (hole) envelope wave functions, φ_a , is defined as

$$\left(-\frac{\hbar}{2m_a^*} \nabla^2 + V_a \right) \varphi_a = E_a \varphi_a, \quad a = e/h \quad (1)$$

where \hbar is the reduced Planck constant, m_a^* is the reduced mass and V_a is the potential energy exerted on the charge carrier in the medium. The total exciton energy is approximated by

$$E = E_{bg} + E_e + E_h \quad (2)$$

where E_{bg} is the bulk's band gap. The potential energy of the charge carriers in a single component particle set to 0, while in a heterostructure it is determined according to the band offset of the materials, as is described in table 1. The potential energy outside the particle, which determines the height of the well's wall, was set to $V_{ligands} = [E_{LH}(ligands) - E_{bg}(ZnSe)]/2$, where $E_{LH}(ligands)$ is the energy difference between the LUMO and HOMO energies of the ligand. For oleylamine, $E_{LH}(ligands) = 4.430 eV$.²⁰

In our calculations we neglected the Coulomb, Exchange, and Correlation interactions, which is not easily obtained for elongated systems, and may further shift the exciton's energy. For the calculations described in this paper, both the bulk band gap energy for ZnSe and ZnS and the effective masses were taken from reference 21

and 22, and are summarized in Table 2. The hole states correspond to the heavy hole, which dominates the valence band-edge states in this system.

Table 2. Bulk band gap energy and effective masses for ZnSe and CdS

	ZnSe	CdS	Environment
m_e^*	$0.14 m_e$	$0.18 m_e$	$1 m_e$
m_{hh}^*	$0.53 m_e$	$0.6 m_e$	$1 m_e$
E_{bg}	2.72eV	2.45eV	4.430eV
V_e	0.8	0	2.20eV
V_h	0	0.52	2.23eV

The dimensions of the ZnSe and hetero- ZnSe/CdS nanorods used in the calculations were based on the averaged dimensions obtained from TEM measurements of the experimental systems. In all the modeled systems the ZnSe rod length was set to 58 nm, the ZnSe rod radius was set as 2.005 nm, and the CdS shel thickness was set to 0.42nm (Figure 7).

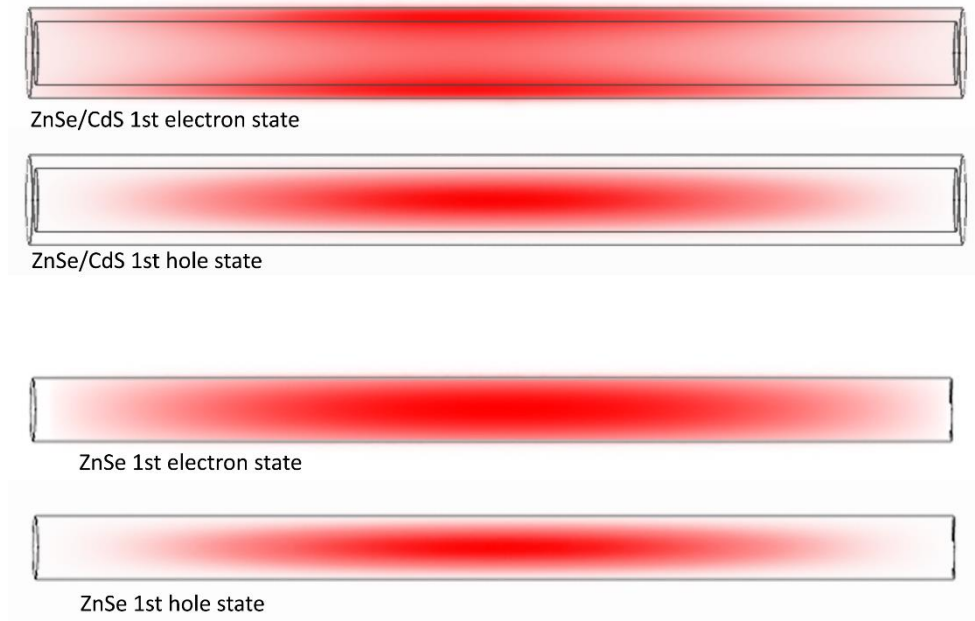


Figure 7: The contour of the first electron and hole wave functions cross section along the zx plane in ZnSe rods (bottom) and in ZnSe/CdS core/shell rods (top) obtained using the EMA model. While the hole wave function resides in the core, the electron wave function resides in the shell, but exhibits strong penetration into the core.

It should be accentuated that the model provides only a first approximation for the accurate energy values of the system, and a more detailed picture of the electronic structure (hole state mixing, electronic fine structure, and dipole moment induced effects) would require a more sophisticated modelling scheme.

Based on the band-offsets of ZnSe and CdS,^{21,22} ZnSe/CdS core/shell rods are expected to exhibit a type-II behavior, in which upon excitation the hole resides in the ZnSe core region, while the electron resides in the CdS shell. The EMA calculation indeed indicates that wave function of the hole is confined to the ZnSe

core, and its spatial distribution highly resembles that of the hole in ZnSe rods. The electronic wave function was found to reside in the shell and occupy a CdS state. However, the relatively small thickness of the shell leads to a strong confinement and hence to an increase in the energy of the electronic level almost to the band offset (Figure 8). Consequently, as depicted in Figure 7, the electronic wave function exhibits a significant penetration to the ZnSe core. Thus, despite the type II structure the overlap between the electron and hole wave functions is significant, hence the emission from these heterostructured nanorods is expected to be relatively high.

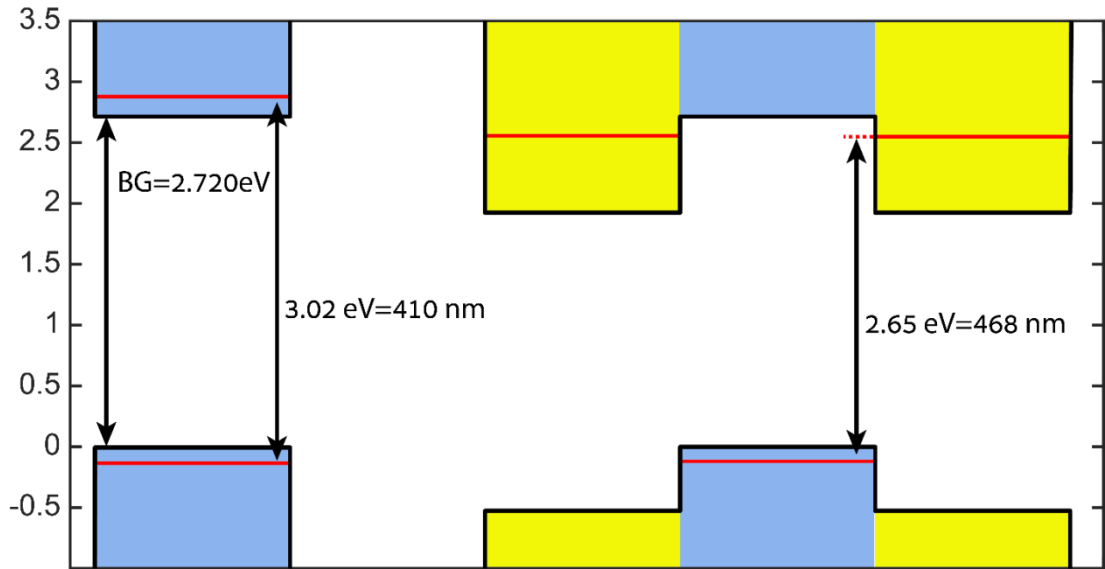


Figure 8: The band diagram of ZnSe (left) and of ZnSe/CdS nanorods (right). EMA calculations indicate that the system is a type II heterostructure. The hole energy level is a ZnSe hole state and it is almost similar in energy to the hole state of ZnSe rods. The electron energy level resides in the CdS shell, but due to the high confinement is relatively high, reaching almost the conduction band edge. The type-II band gap obtained from the calculation is of 2.65 eV, in high agreement to the experimental adsorption band edge of the system.

Furthermore, we dispersed the ZnSe (rod)/CdS (rod) core/shell nanorods into poly(vinyl butyral-co-vinyl alcohol-co-vinyl acetate) to fabricate the QD-polymer film. In the experiment, we chose the 560 nm emissive ZnSe (rod)/CdS (rod) core/shell nanorods as an example, and both core/shell rods and poly(vinyl butyral-co-vinyl alcohol-co-vinyl acetate) can be well dissolved in toluene and mixed to form a homogeneous solution. After casting solution, the toluene was evaporated and the film was formed. The QD-polymer film presents a green emission in 560 nm with a FWHM of 37.8 nm (Fig 9c). Here, the 10 nm red-shift of QD-polymer comparing to the solution sample was due to the aggregations of quantum rods and the modification of core/shell quantum rods by polymer.^{25,26,27} The composite film presents a good chemical stability under air by maintaining their emission properties for over 3 months (Fig 9a, b). Such nanocomposites have the potential in polarized light emitting diodes, flexible electronic displays, and other optoelectronic devices.

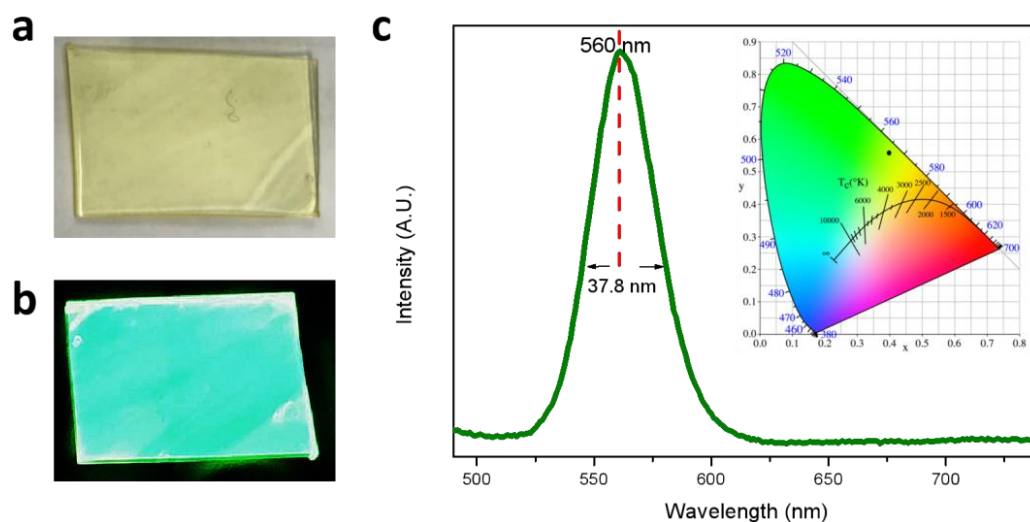


Figure 9. a) ZnSe (rod)/CdS (rod) core/shell nanorods film. a) ZnSe (rod)/CdS (rod) core/shell nanorods film under 365 nm excitation. c) PL spectra of ZnSe (rod)/CdS (rod) core/shell nanorods film (Insert is CIE image of the film).

5.5 Conclusion

In conclusion, a seeded-growth method was performed to synthesis of type-II ZnSe (rod)/CdS (rod) core/shell nanorods structure. The large charge-separation leads to a distinct red shift of their luminescence spectra to the green range. The particles were further applied into polymer film which may act as a promising candidate for polarized quantum light emitting diodes.

5.6 References

- [1] V. I. Klimov, S. A. Ivanov, J. Nanda, M. Achermann, I. Bezel, J. A. McGuire, A. Piryatinski, *Nature* **2007**, 447, 441.
- [2] D. Oron, M. Kazes, U. Banin, *Phys. Rev. B.* **2007**, 75, 1.
- [3] D. Chen, A. Wang, M. Buntine, G. Jia, *ChemElectroChem* **2019**, 6, 4709.
- [4] H. Htoon, J. A. Hollingsworth, R. Dickerson, V. I. Klimov, *Phys. Rev. Lett.* **2003**, 91, 1.
- [5] G. Jia, S. Xu, A. Wang, *J. Mater. Chem. C* **2015**, 3, 8284.
- [6] M. Kazes, D. Y. Lewis, Y. Ebenstein, T. Mokari, U. Banin, *Adv. Mater.* **2002**, 14, 317.
- [7] M. Shim, *J. Phys. D. Appl. Phys.* **2017**, 50, DOI 10.1088/1361-6463/aa65a5.
- [8] D. Gao, P. Zhang, Z. Sheng, D. Hu, P. Gong, C. Chen, Q. Wan, G. Gao, L. Cai, *Adv. Funct. Mater.* **2014**, 24, 3897.

- [9] L. Carbone, C. Nobile, M. De Giorgi, F. Della Sala, G. Morello, P. Pompa, M. Hytch, E. Snoeck, A. Fiore, I. R. Franchini, M. Nadasan, A. F. Silvestre, L. Chiodo, S. Kudera, R. Cingolani, R. Krahne, L. Manna, *Nano Lett.* **2007**, 7, 2942.
- [10] D. V. Talapin, J. H. Nelson, E. V. Shevchenko, S. Aloni, B. Sadtler, A. P. Alivisatos, *Nano Lett.* **2007**, 7, 2951.
- [11] S. Kumar, M. Jones, S. S. Lo, G. D. Scholes, *Small* **2007**, 3, 1633.
- [12] H. Zhong, G. D. Scholes, *J. Am. Chem. Soc.* **2009**, 131, 9170.
- [13] A. Nemchinov, M. Kirsanova, N. N. Hewa-kasakarage, M. Zamkov, *J. Phys. Chem. C* **2008**, 112, 9301.
- [14] D. Dorfs, A. Salant, I. Popov, U. Banin, *Small* **2008**, 4, 1319.
- [15] B. Ji, Y. E. Panfil, U. Banin, *ACS Nano* **2017**, 11, 7312.
- [16] D. Chen, H. Zhang, Y. Li, Y. Pang, Z. Yin, H. Sun, L. C. Zhang, S. Wang, M. Saunders, E. Barker, G. Jia, *Adv. Mater.* **2018**, 31, 1803351.
- [17] G. Jia, A. Sitt, G. B. Hitin, I. Hadar, Y. Bekenstein, Y. Amit, I. Popov, U. Banin, *Nat. Mater.* **2014**, 13, 301.
- [18] D. Chen, A. Wang, H. Li, L. A. Galan, C. Su, Z. Yin, M. Massi, A. Suvorova, M. Saunders, J. Li, A. Sitt, G. Jia, *Nanoscale* **2019**, 11, 10190.
- [19] G. Jia, U. Banin, *J. Am. Chem. Soc.* **2014**, 136, 11121.
- [20] G. Pellegrini, G. Mattei, P. Mazzoldi, *J. Appl. Phys.* **2005**, 97, 073706.
- [21] Landolt-Boernstein: Numerical Data and Functional Relationships in Science

and Technology. Group III, Condensed Matter, Sub Volume C; Martienssen, W., Ed.; Springer Verlag: Berlin, **1998**.

- [22] Dinger, A. Petillon, S. Gruñ n, M. Hetterich, M. Klingshirn, C. Semicond. *Sci. Technol.* **1999**, *14*, 595.
- [23] B. Ji, Y. E. Panfil, N. Waiskopf, S. Remennik, I. Popov, U. Banin, *Nat. Commun.* **2019**, *10*, 1.
- [24] S. A. Ivanov, A. Piryatinski, J. Nanda, S. Tretiak, K. R. Zavadil, W. O. Wallace, D. Werder, V. I. Klimov, *J. Am. Chem. Soc.* **2007**, *129*, 11708.
- [25] J. Lee, V. C. Sundar, J. R. Heine, M. G. Bawendi, K. F. Jensen, *Adv. Mater.* **2000**, *12*, 1102.
- [26] Y. Q. Wang, Y. Y. Zhang, F. Zhang, W. Y. Li, *J. Mater. Chem.* **2011**, *21*, 6556.
- [27] R. Zhang, H. Yu, B. Li, *Nanoscale* **2012**, *4*, 5856.
- [28] C. Van de Walle, J. Neugebauer, *Nature* **2003**, *423*, 626.

Chapter 6. Summary and Perspectives

In summary, we have developed various strategies for the facile synthesis of three types of quasi-one-dimensional colloidal semiconductor nanocrystals such as alloyed $\text{ZnS}_x\text{Se}_{1-x}$ quantum rods, hetero-ZnS (short arms)–ZnSe (long arms)/ZnS shell nanorod couples and ZnSe(rod)/CdS(rod) core shell quantum rods. The band gap alignments have been investigated and each structure has shown novel properties with relevance to diverse applications.

There are some perspectives for future works:

1. Although some progress has been made in the syntheses of ZnSe/ZnS and ZnTe/ZnS core/shell structures, it is still challenging to achieve good luminescence quantum efficiencies in these materials due to the interfacial defects and strains. Future work needs to focus on this aspect to improve their luminescence quantum efficiency and stability, which could be achieved by engineering the interfaces between the core and shell materials through forming alloyed shell or graded shell with significantly reduced lattice mismatch.
2. The research of 2D zinc-containing semiconductor nanocrystals such as nanoplatelets still in its infancy. Further studies on the growth mechanisms and layer-by-layer thickness control of these NCs are highly desired.
3. ZnTe, Zn_3P_2 and Zn_3As_2 with relatively small band gaps will be important in visible and NIR lighting and detection. Better engineering the precursors for the synthesis in combination with the deep understanding of the growth mechanisms are desired and need to be improved.

4. Heavy-metal-free ZnSe and ZnS nanocrystals already showed their potential in photocatalysis. Further research into metal-semiconductor hybrid structures to leverage their photocatalytic performances is highly demanded.

Contribution Claim

1. Recent Advances in Zinc-Containing Colloidal Semiconductor Nanocrystals for Optoelectronic and Energy Conversion Applications, *ChemElectroChem* 2019, 6, 4709-4724.

To Whom It May Concern

I, Dechao Chen, contributed a major contribution to this work in manuscript writing in the paper entitled “Recent Advances in Zinc-Containing Colloidal Semiconductor Nanocrystals for Optoelectronic and Energy Conversion Applications” in *ChemElectroChem* 2019, 6, 4709-4724.

(Signature of Candidate)

I, as a Co-Author, endorse that this level of contribution by the candidate indicated above is appropriate.

Dechao Chen

(Full Name of Co-Author 1)

(Signature of Co-Author 1)

Aixiang Wang

(Full Name of Co-Author 2)

(Signature of Co-Author 2)

Mark Buntine

(Full Name of Co-Author 3)

(Signature of Co-Author 3)

Guohua Jia

(Full Name of Co-Author 4)

(Signature of Co-Author 4)

2. Spontaneous Formation of Noble- and Heavy-Metal-Free Alloyed Semiconductor Quantum Rods for Efficient Photocatalysis, *Advanced Materials*. 2018, 30, 1803351.

To Whom It May Concern

I, Dechao Chen, contributed a major contribution to this work in nanoparticle synthesis, characterizations, figure preparation, experimental data analysis and organization, and manuscript writing in the paper entitled “Spontaneous Formation of Noble- and Heavy-Metal-Free Alloyed Semiconductor Quantum Rods for Efficient Photocatalysis” in *Advanced Materials*. 2018, 30, 1803351.

(Signature of Candidate)

I, as a Co-Author, endorse that this level of contribution by the candidate indicated above is appropriate.

Dechao Chen

(Full Name of Co-Author 1)

(Signature of Co-Author 1)

Huayang Zhang

(Full Name of Co-Author 2)

(Signature of Co-Author 2)

Yunguo Li

(Full Name of Co-Author 3)

(Signature of Co-Author 3)

Yingping Pang

(Full Name of Co-Author 4)

(Signature of Co-Author 4)

Zongyou Yin

(Full Name of Co-Author 5)

(Signature of Co-Author 5)

Hongqi Sun

(Full Name of Co-Author 6)

(Signature of Co-Author 6)

Lai-Chang Zhang

(Full Name of Co-Author 7)

(Signature of Co-Author 7)

Shaobin Wang

(Full Name of Co-Author 8)

(Signature of Co-Author 8)

Martin Saunders

(Full Name of Co-Author 9)

(Signature of Co-Author 9)

Emily Barker

(Full Name of Co-Author 10)

(Signature of Co-Author 10)

Guohua Jia

(Full Name of Co-Author 11)

(Signature of Co-Author 11)

3. Colloidal quasi-one-dimensional dual semiconductor core/shell nanorod couple heterostructures with blue fluorescence” in *Nanoscale*, 2019, 11, 10190-10197.

To Whom It May Concern

I, Dechao Chen, contributed a major contribution to this work in nanoparticle synthesis, characterizations, figure preparation, experimental data analysis and organization, and manuscript writing in the paper entitled “Colloidal quasi-one-dimensional dual semiconductor core/shell nanorod couple heterostructures with blue fluorescence” in *Nanoscale*, 2019, 11, 10190-10197.

(Signature of Candidate)

I, as a Co-Author, endorse that this level of contribution by the candidate indicated above is appropriate.

Dechao Chen

(Full Name of Co-Author 1)

(Signature of Co-Author 1)

Aixiang Wang

(Full Name of Co-Author 2)

(Signature of Co-Author 2)

Hongbo Li

(Full Name of Co-Author 3)

(Signature of Co-Author 3)

Laura Abad Galán

(Full Name of Co-Author 4)

(Signature of Co-Author 4)

Cong Su

(Full Name of Co-Author 5)

(Signature of Co-Author 5)

Zongyou Yin

(Full Name of Co-Author 6)

(Signature of Co-Author 6)

Massimiliano Massi

(Full Name of Co-Author 7)

(Signature of Co-Author 7)

Alexandra Suvorova

(Full Name of Co-Author 8)

(Signature of Co-Author 8)

Martin Saunders

(Full Name of Co-Author 9)

(Signature of Co-Author 9)

Ju Li

(Full Name of Co-Author 10)

(Signature of Co-Author 10)

Amit Sitt

(Full Name of Co-Author 11)

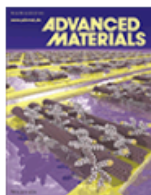
(Signature of Co-Author 11)

Guohua Jia

(Full Name of Co-Author 12)

(Signature of Co-Author 12)

Copyright Claim



Thank you for your order!

Dear Mr. Dechao Chen,

Thank you for placing your order through Copyright Clearance Center's RightsLink® service.

Order Summary

Licensee: Dechao Chen
Order Date: Jan 15, 2020
Order Number: 4750020910905
Publication: Advanced Materials
Title: Spontaneous Formation of Noble- and Heavy-Metal-Free Alloyed Semiconductor Quantum Rods for Efficient Photocatalysis
Type of Use: Dissertation/Thesis
Order Total: 0.00 AUD

View or print complete [details](#) of your order and the publisher's terms and conditions.

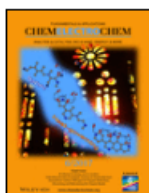
Sincerely,

Copyright Clearance Center

Tel: +1-855-239-3415 / +1-978-646-2777
customer@copyright.com
<https://myaccount.copyright.com>



RightsLink®



Thank you for your order!

Dear Mr. Dechao Chen,

Thank you for placing your order through Copyright Clearance Center's RightsLink® service.

Order Summary

Licensee: Dechao Chen
Order Date: Jan 15, 2020
Order Number: 4750020965214
Publication: ChemElectroChem
Title: Recent Advances in Zinc-Containing Colloidal Semiconductor Nanocrystals for Optoelectronic and Energy Conversion Applications
Type of Use: Dissertation/Thesis
Order Total: 0.00 AUD

View or print complete [details](#) of your order and the publisher's terms and conditions.

Sincerely,

Copyright Clearance Center

Tel: +1-855-239-3415 / +1-978-646-2777
customercare@copyright.com
<https://myaccount.copyright.com>



RightsLink®